А.М. Никишин
Сдвиги

СТРОЕНИЕ ПРОСТОЙ СДВИГОВОЙ ЗОНЫ

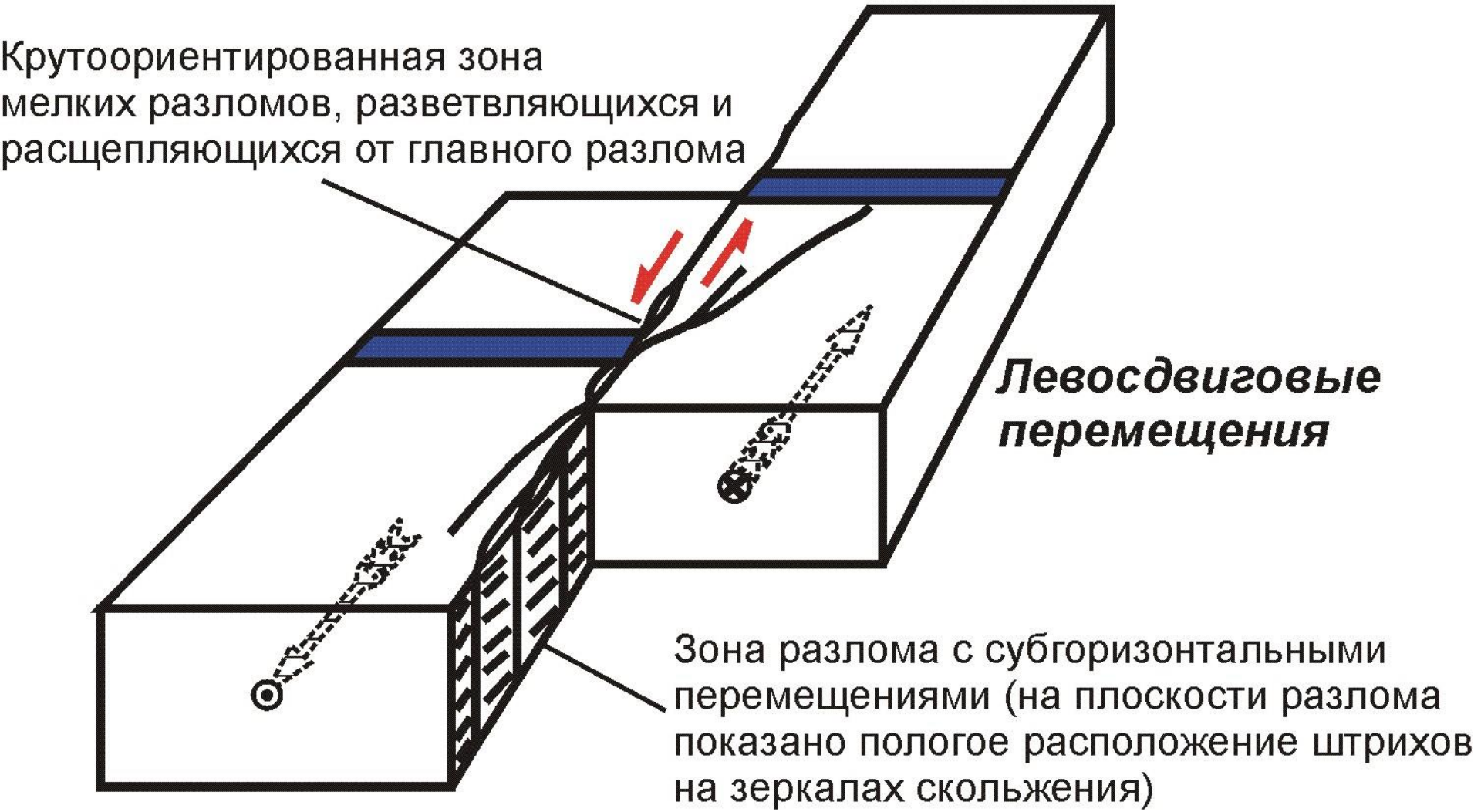

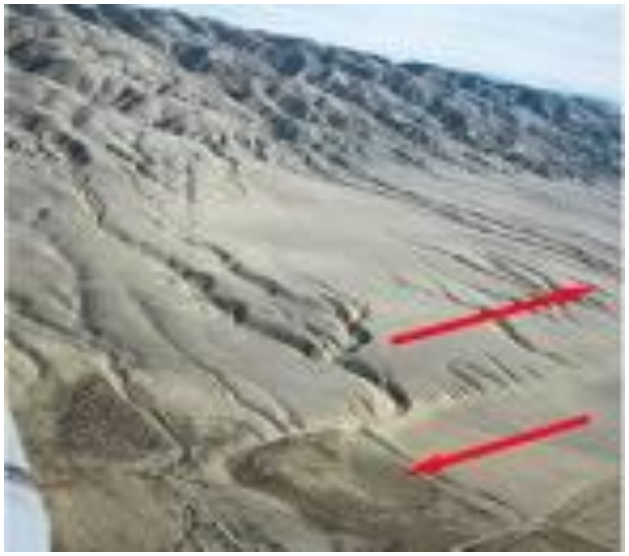

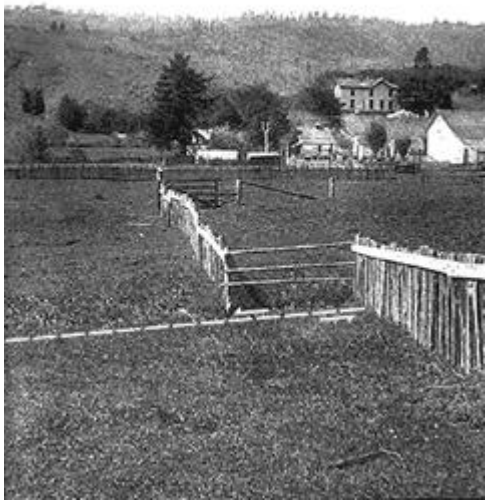

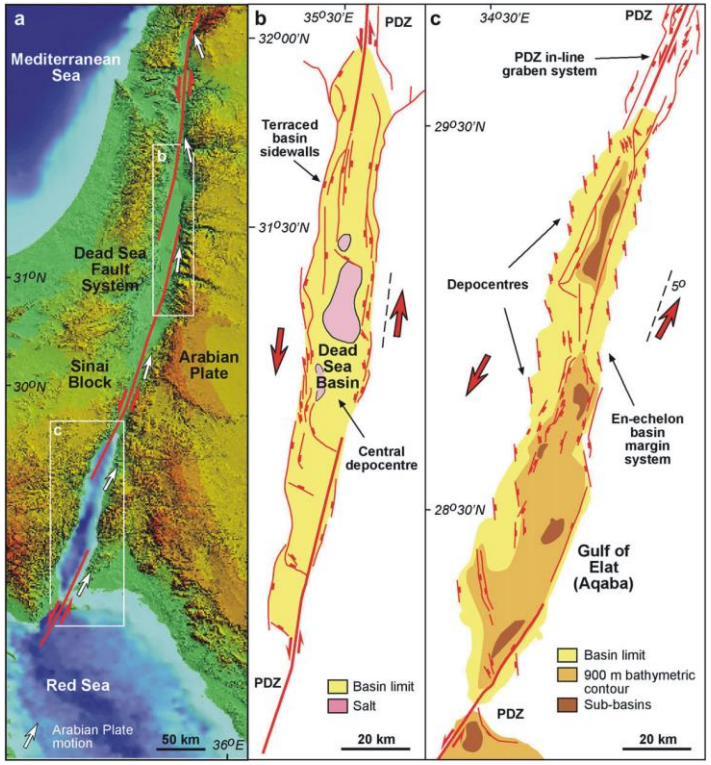
a
Mediterranean Sea
Dead Sea Fault System
Sinai Block
Arabian Plate
Red Sea
Arabian Plate motion
50 km
31°N
30°N
36°E
b
35°30'E
PDZ
32°00'N
Terraced basin sidewalls
31°30'N
Dead Sea Basin
Central depocentre
PDZ
Basin limit
Salt
20 km
c
34°30'E
PDZ
PDZ in-line graben system
29°30'N
Depocentres
5°
En-echelon basin margin system
28°30'N
Gulf of Elat (Aqaba)
Basin limit
900 m bathymetric contour
Sub-basins
PDZ
20 km

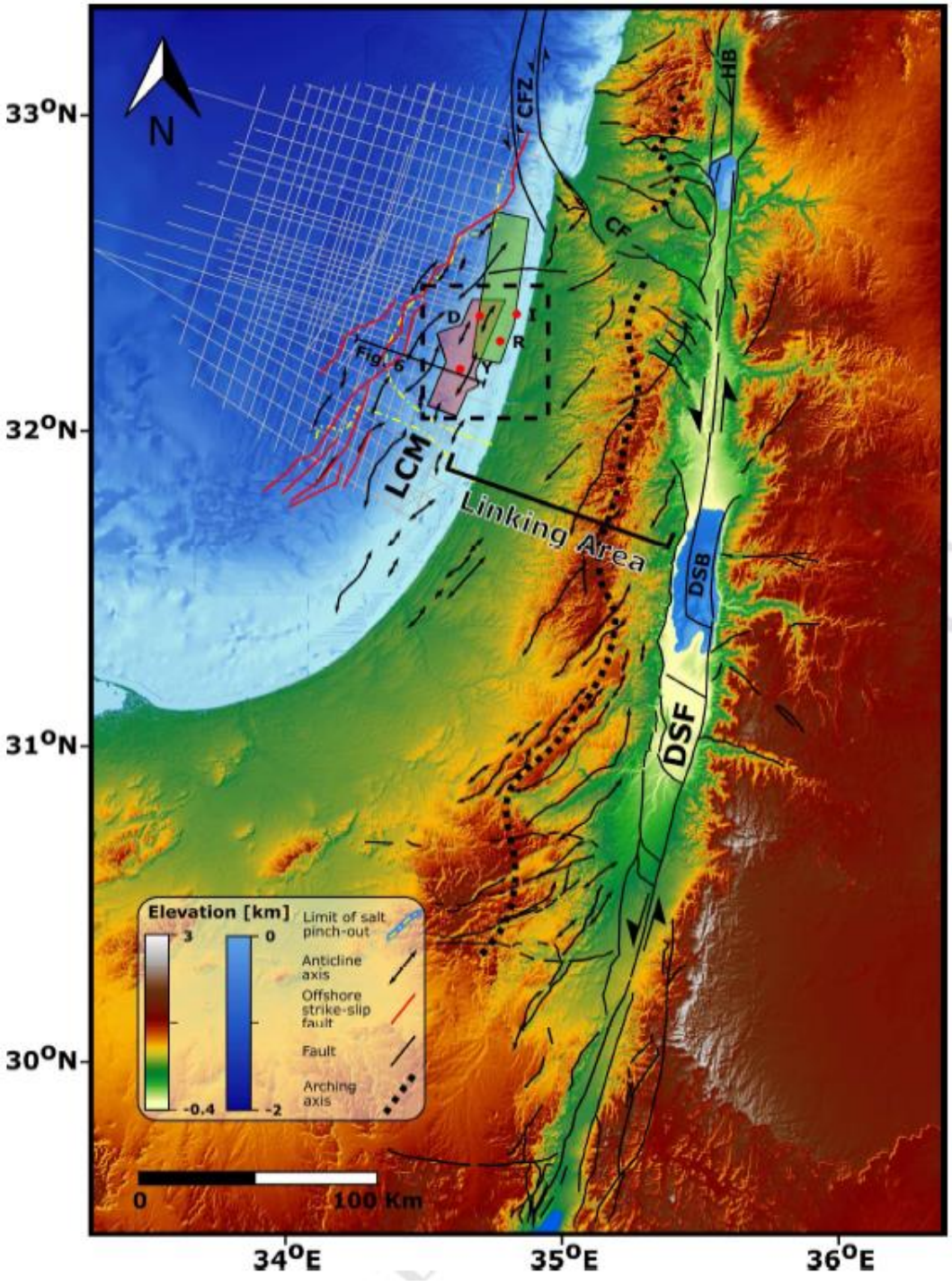
N
33°N
32°N
31°N
30°N
34°E
35°E
36°E
CFZ
HB
CF
LCM
Linking Area
DSB
DSF
Fig. 6
D
I
R
Y
Elevation [km]
3
-0.4
0
-2
Limit of salt pinch-out
Anticline axis
Offshore strike-slip fault
Fault
Arching axis
0
100 Km

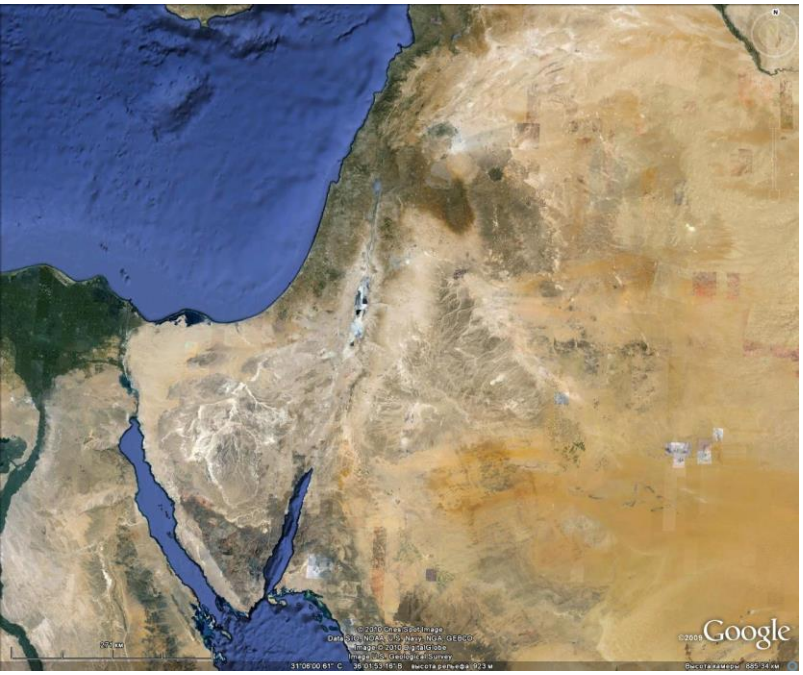
©2009 Google


©2016 CNES/Spot Image
Data SIO, NOAA, U.S. Navy, NGA, GEBCO
Image © 2016 DigitalGlobe
Image © 2016 TerraMetrics
272 км
©2009 Google

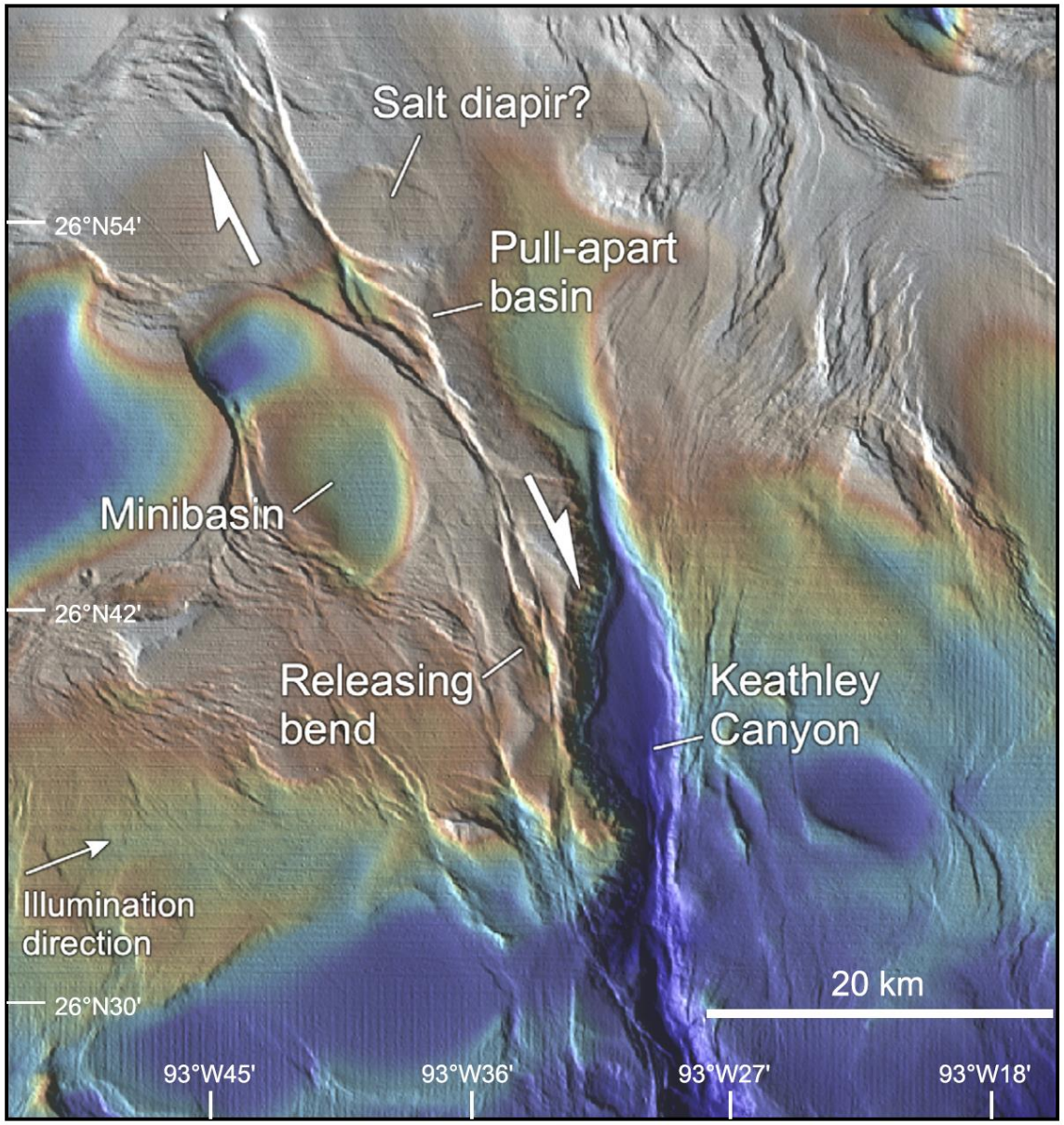

Fig. 77. Bathymetric map of a portion of the northern Gulf of Mexico near Keathley Canyon, illustrating pull-apart-basin formation as a strike-slip fault system weaves its way between minibasins. See text for further details.
Image derived from GeoMapApp using data from D. L. Divins, and D. Metzger, NGDC Coastal Relief Model, http://www.ngdc.noaa.gov/mgg/coastal/coastal.html.

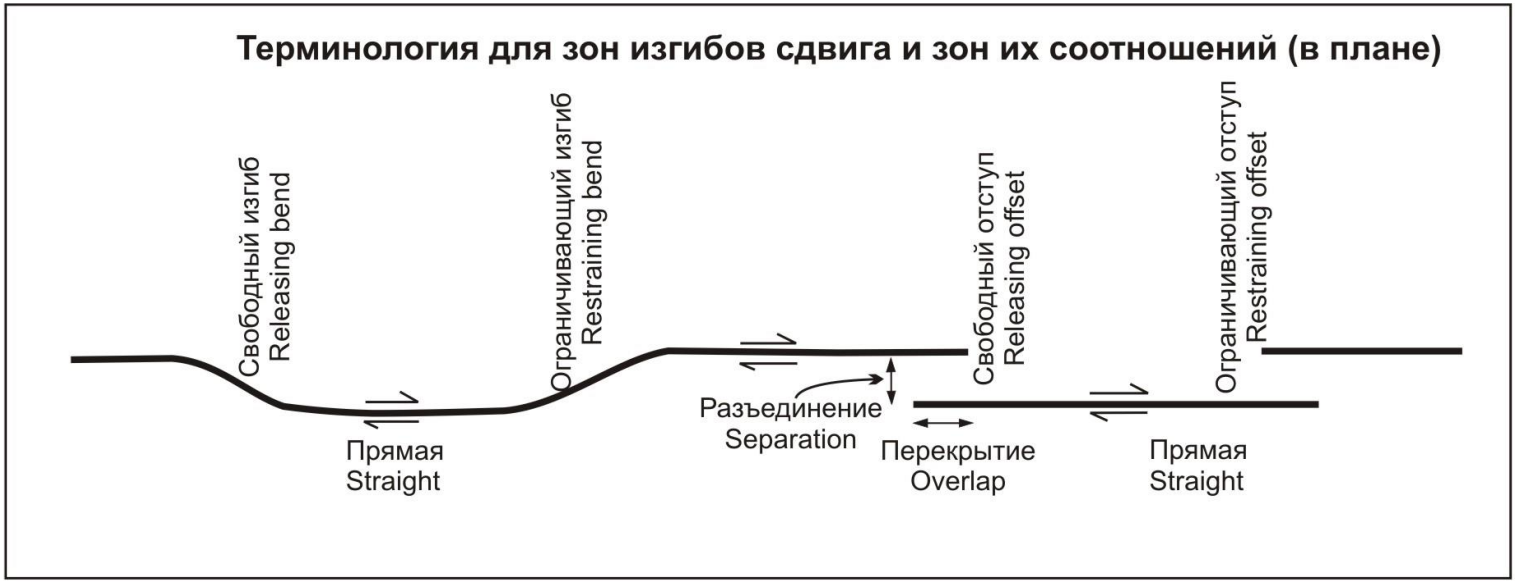
Терминология для зон изгибов сдвига и зон их соотношений (в плане)
Свободный изгиб
Releasing bend
Ограничивающий изгиб
Restraining bend
Свободный отступ
Releasing offset
Ограничивающий отступ
Restraining offset
Разъединение
Separation
Прямая
Straight
Перекрытие
Overlap
Прямая
Straight

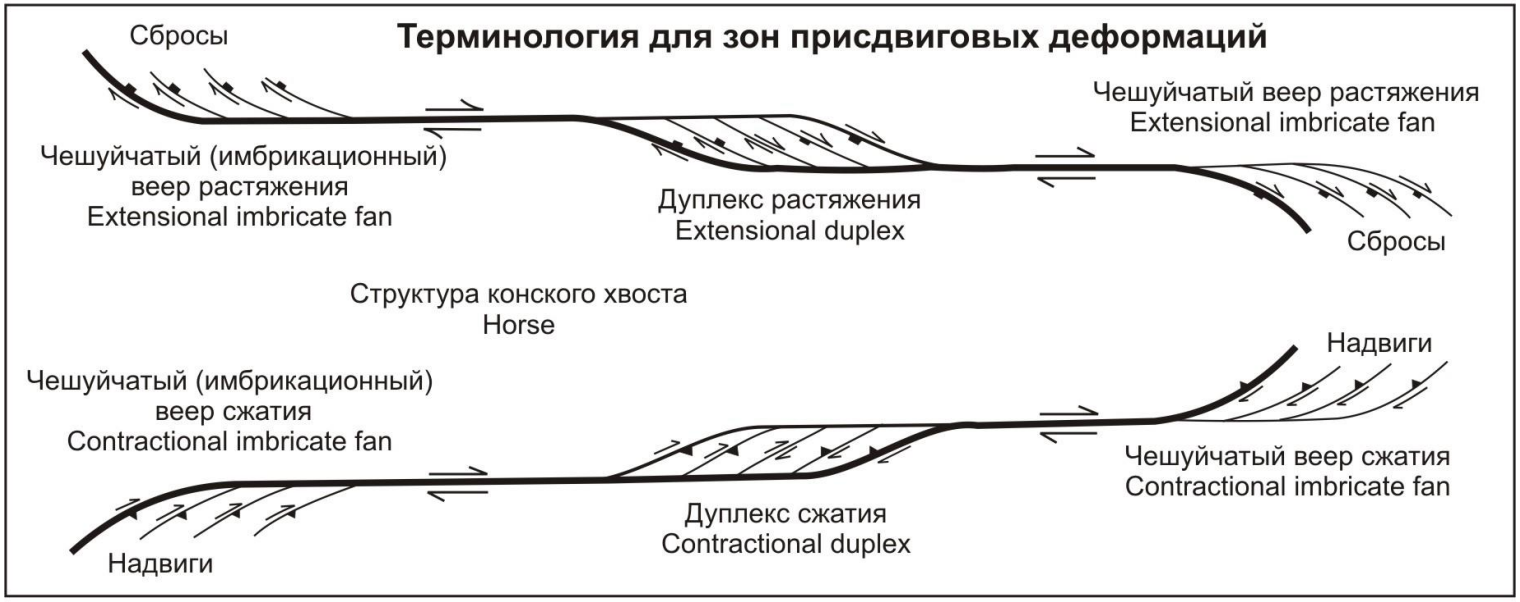
Терминология для зон присдвиговых деформаций
Сбросы
Чешуйчатый (имбрикационный)
веер растяжения
Extensional imbricate fan
Дуплекс растяжения
Extensional duplex
Чешуйчатый веер растяжения
Extensional imbricate fan
Сбросы
Структура конского хвоста
Horse
Надвиги
Чешуйчатый (имбрикационный)
веер сжатия
Contractional imbricate fan
Чешуйчатый веер сжатия
Contractional imbricate fan
Дуплекс сжатия
Contractional duplex
Надвиги

Рис. Сд-3.

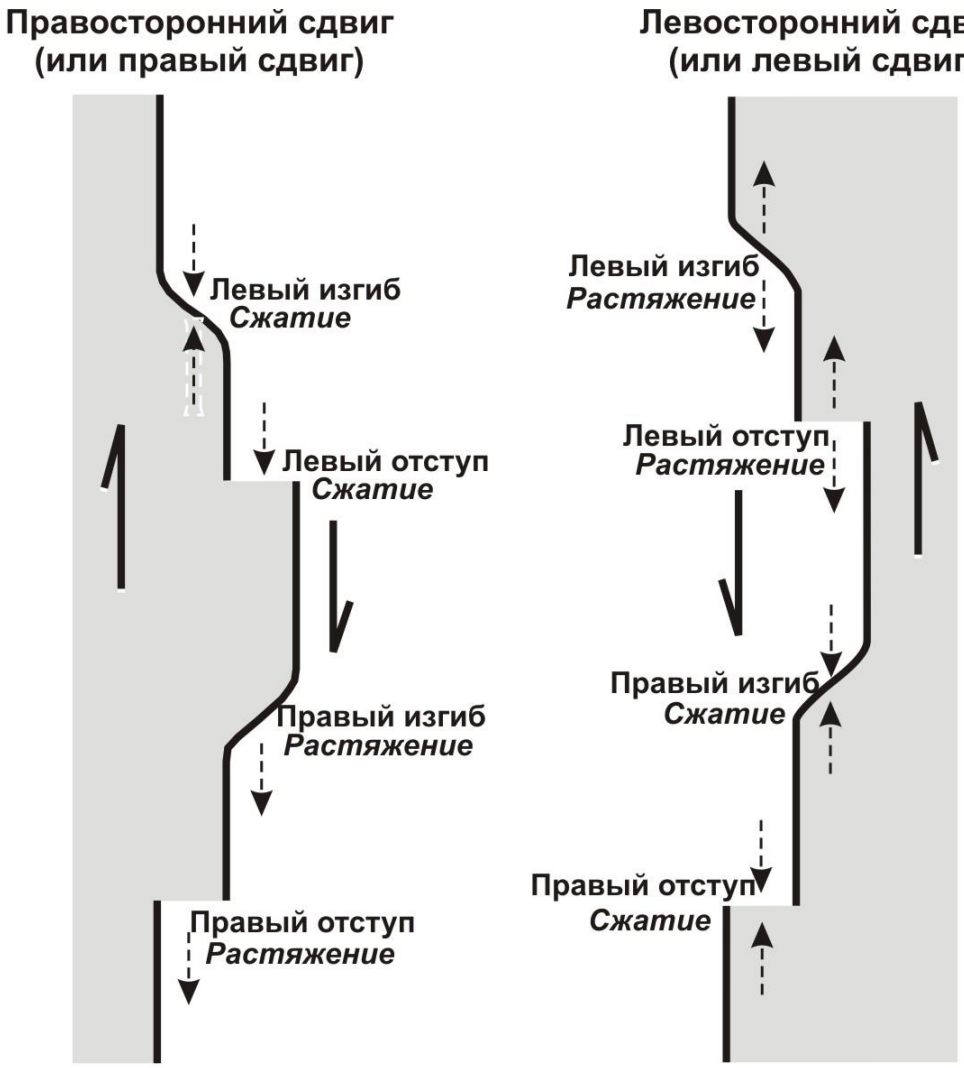
Правосторонний сдвиг
(или правый сдвиг)
Левый изгиб
Сжатие
Левый отступ
Сжатие
Правый изгиб
Растяжение
Правый отступ
Растяжение
Левосторонний сдвиг
(или левый сдвиг)
Левый изгиб
Растяжение
Левый отступ
Растяжение
Правый изгиб
Сжатие
Правый отступ
Сжатие

Рис. Сд-4.

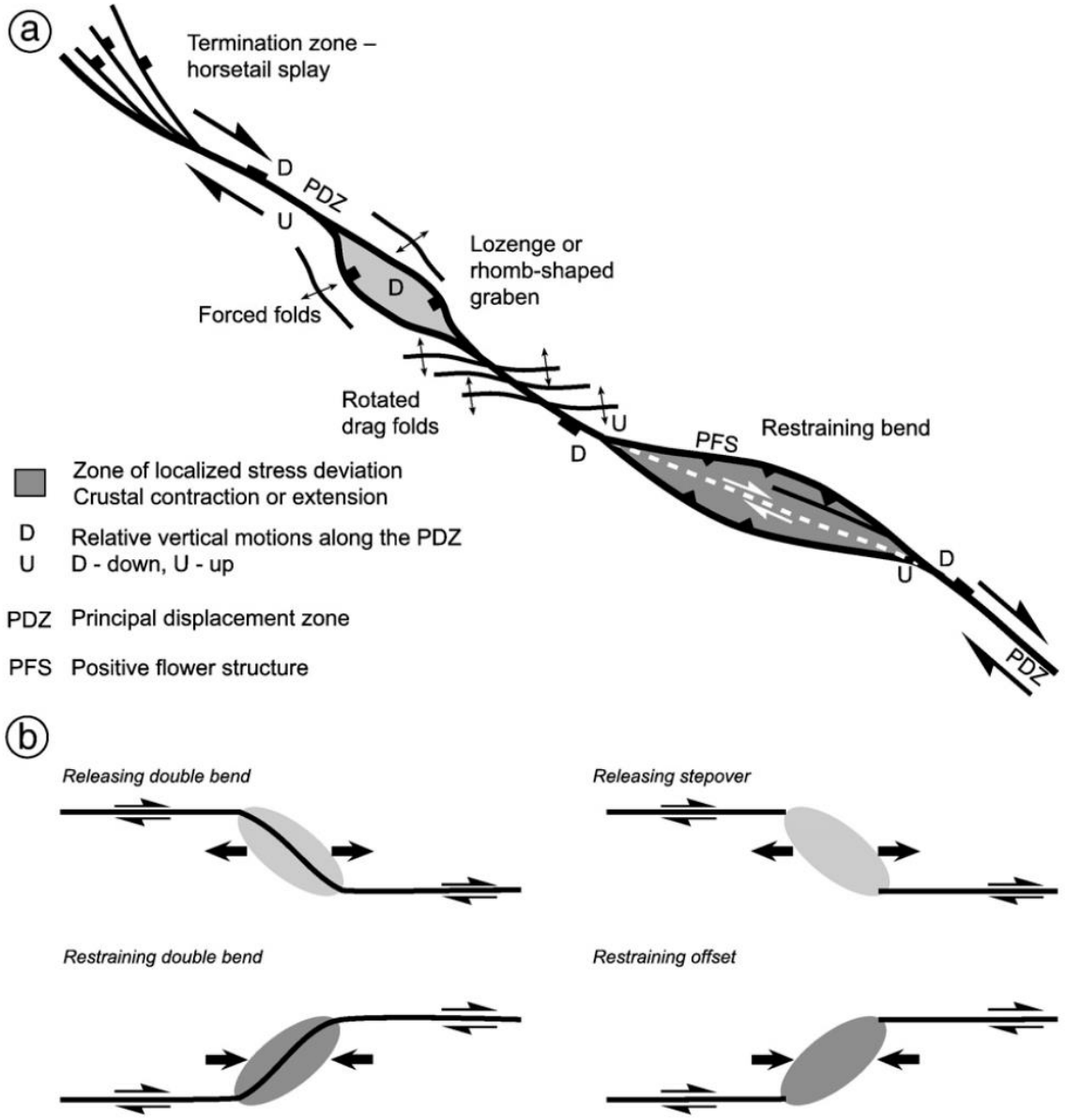

Fig. 30. (a) Schematic diagram illustrating variations in structural style along a strike-slip fault zone. (b) Releasing bend and stepover geometries. a is modified from Christie-Blick and Biddle (1985).

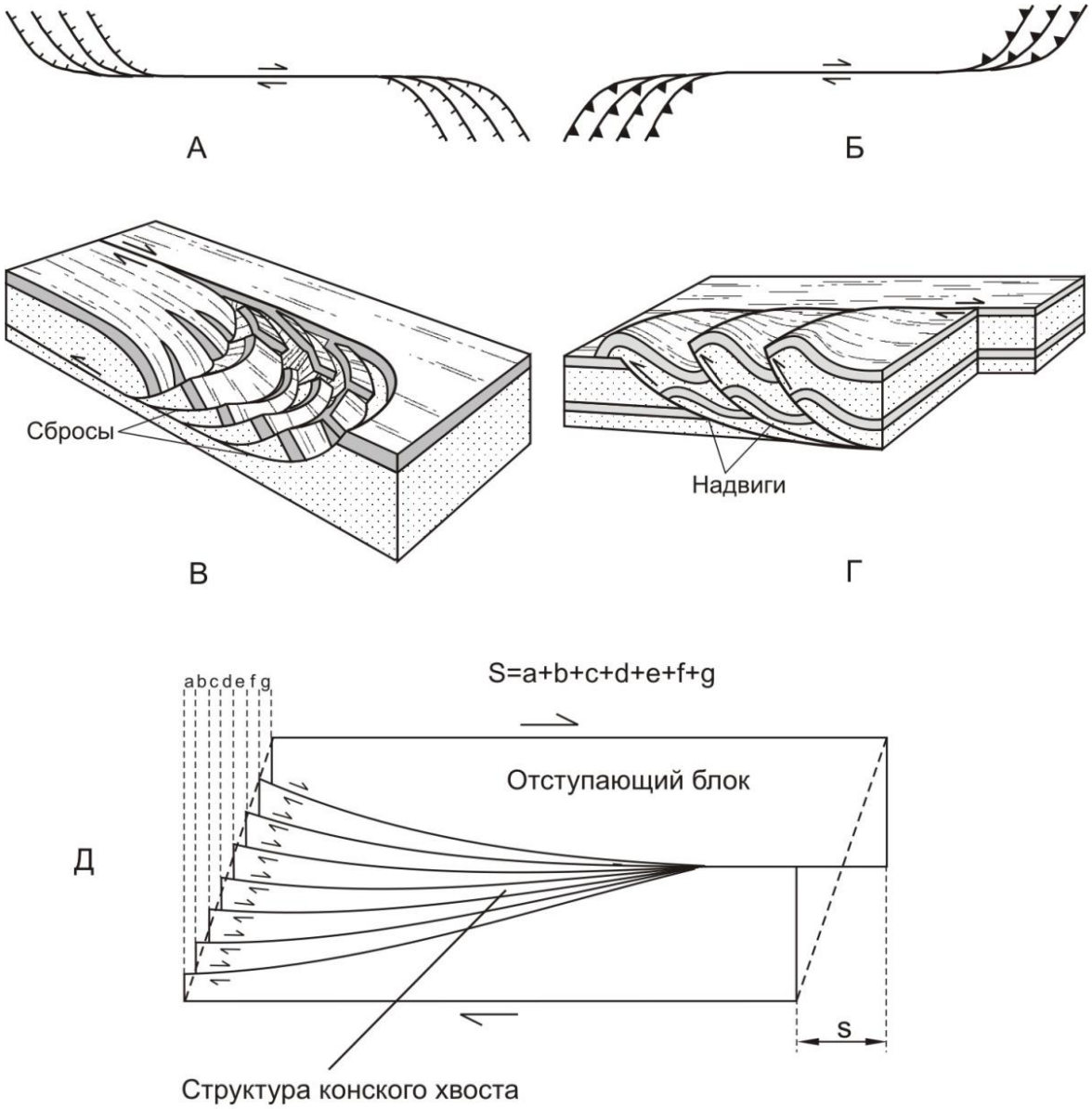
А
Б
Сбросы
В
Надвиги
Г
Д
a b c d e f g
S=a+b+c+d+e+f+g
Отступающий блок
S
Структура конского хвоста

Ртс. Сд-5.

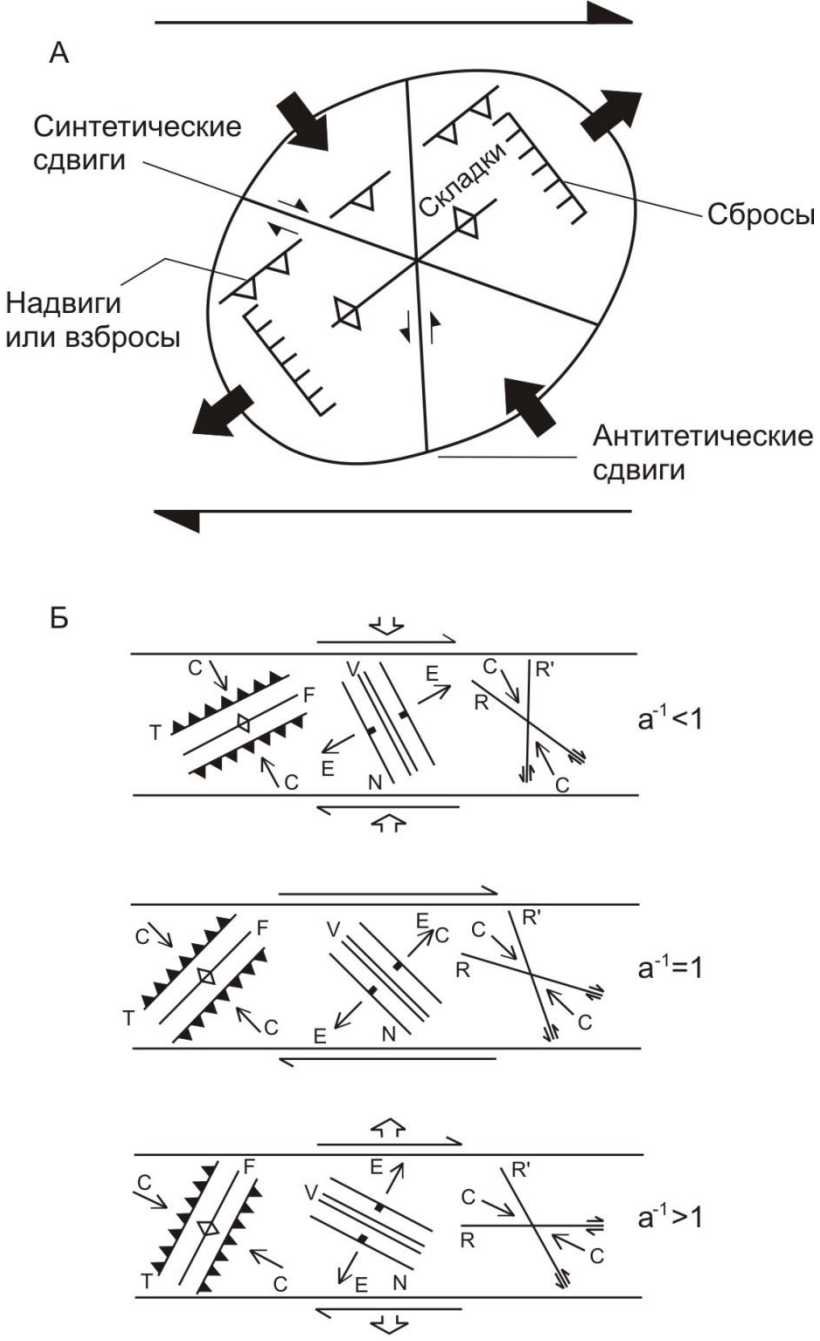
А
Синтетические сдвиги
Складки
Сбросы
Надвиги или взбросы
Антитетические сдвиги
Б
C
F
T
C
V
E
E
N
C
R'
R
C
a-1<1
C
F
T
C
V
E
C
E
N
C
R'
R
C
a-1=1
C
F
T
C
V
E
E
N
C
R'
R
C
a-1>1

Рис. 3.9.

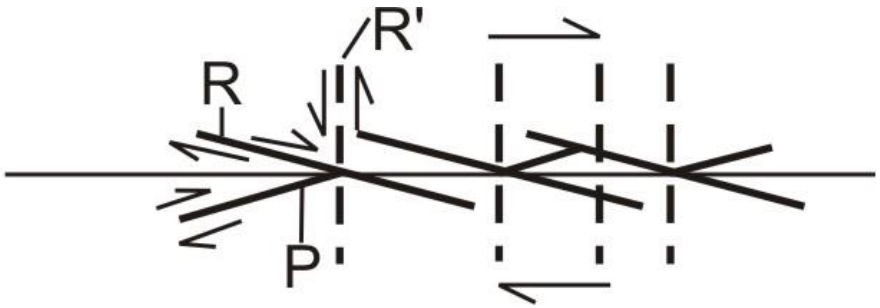

А. Ориентировка дополнительных трещин R, R' и P

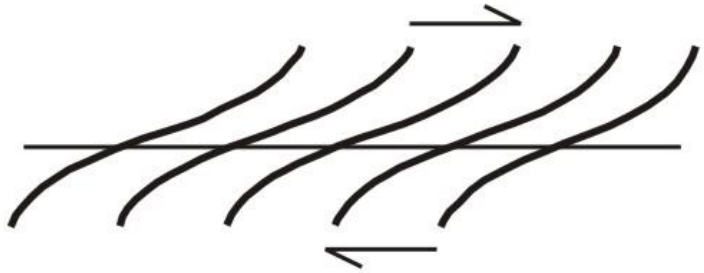

Б. Ориентировка осей сопутствующих складок

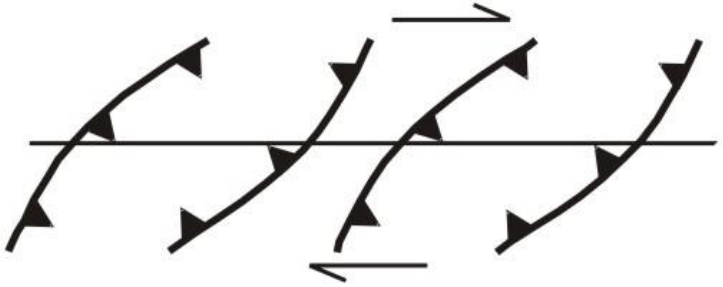

В. Ориентировка плоскостей сопутствующих надвигов

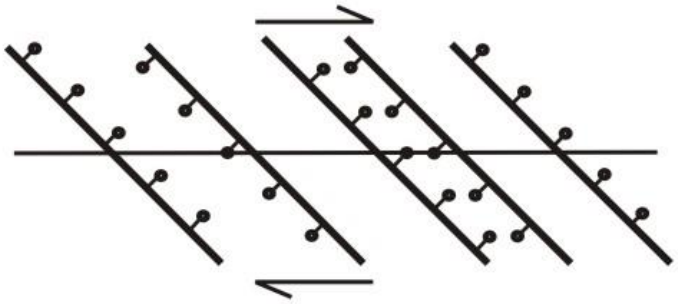

Г. Ориентировка плоскостей сопутствующих сбросов

Рис. Сд-8.

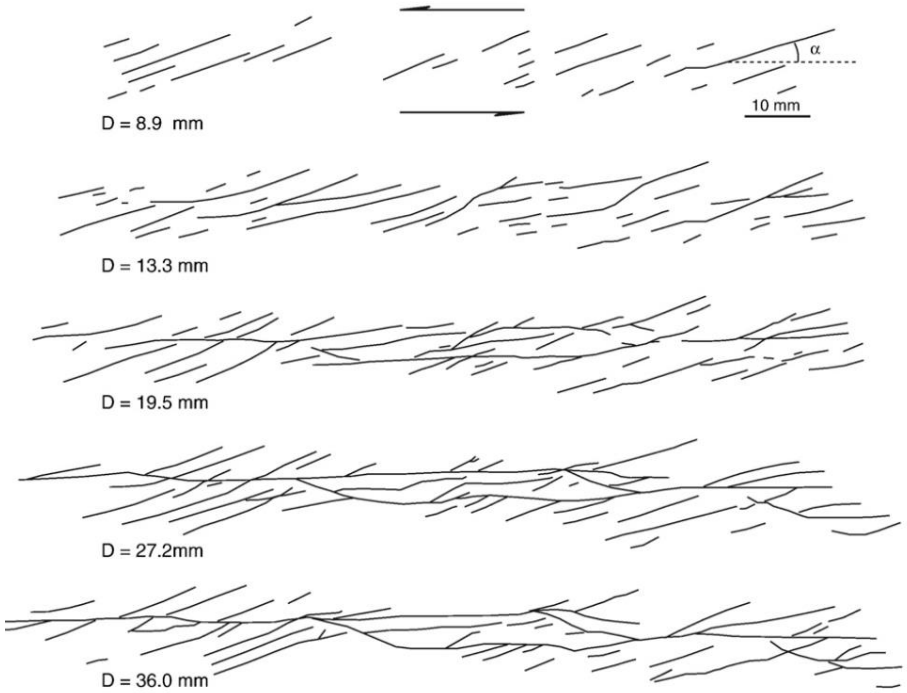

Fig. 2. Fault evolution in a clay cake Riedel experiment. D = horizontal displacement of one base plate.
Redrawn from Tchalenko (1970), with permission of the Geological Society of America.

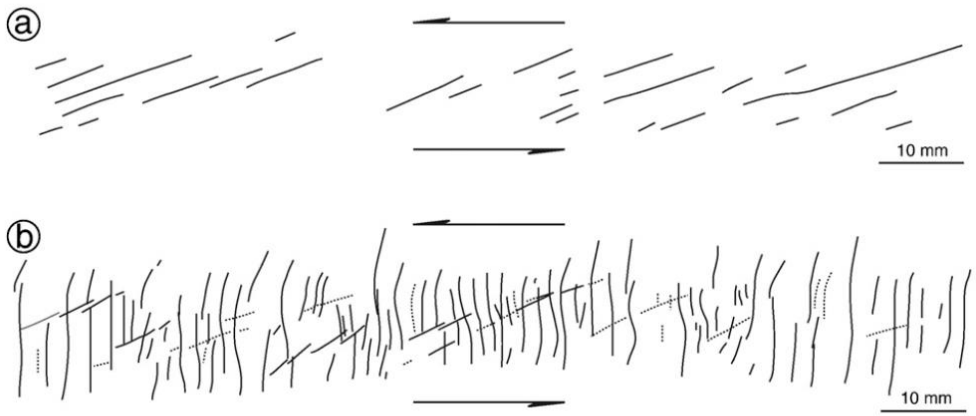

Fig. 3. Comparison of structures in a Riedel experiment using clay with different water contents. (a) Kaolin, 56% water content; (b) kaolin, unspecified water content, but lower than in a, between 45 and 54%. Note that the R′ shears obtain a slightly sigmoidal shape as central segments rotate counter-clockwise with increasing displacement along the basement fault.
Redrawn from Tchalenko (1970), with permission of the Geological Society of America.

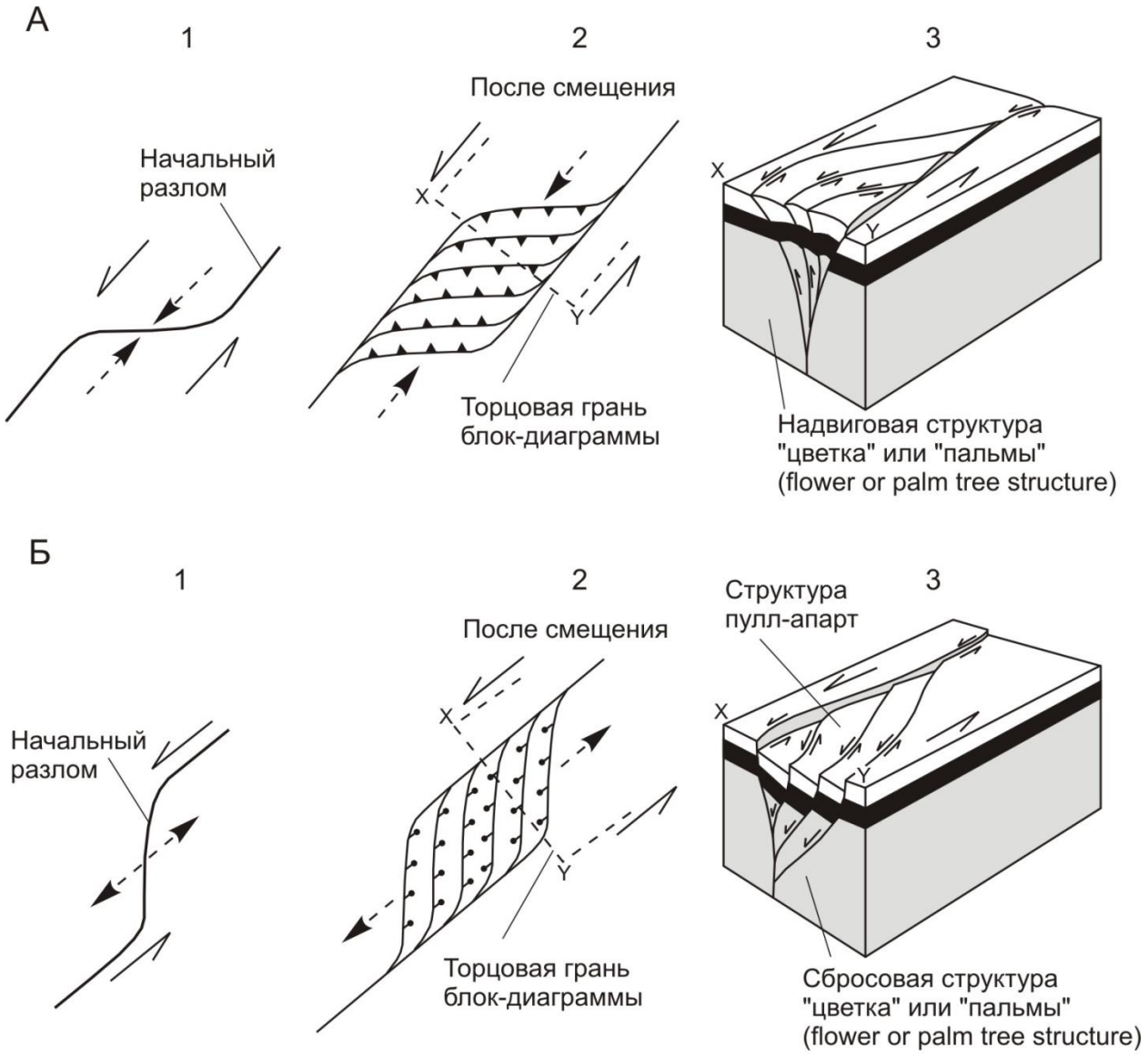
А
1
2
3
После смещения
Начальный разлом
X
Y
Торцовая грань блок-диаграммы
Надвиговая структура "цветка" или "пальмы" (flower or palm tree structure)
Б
1
2
3
Структура пулл-апарт
После смещения
Начальный разлом
X
Y
Торцовая грань блок-диаграммы
Сбросовая структура "цветка" или "пальмы" (flower or palm tree structure)

Рис. 3.14.

ПРИСДВИГОВЫЕ ЦВЕТКОВЫЕ СТРУКТУРЫ

Отрицательная цветковая структура (сдвиго-растяжение, транстенсия)

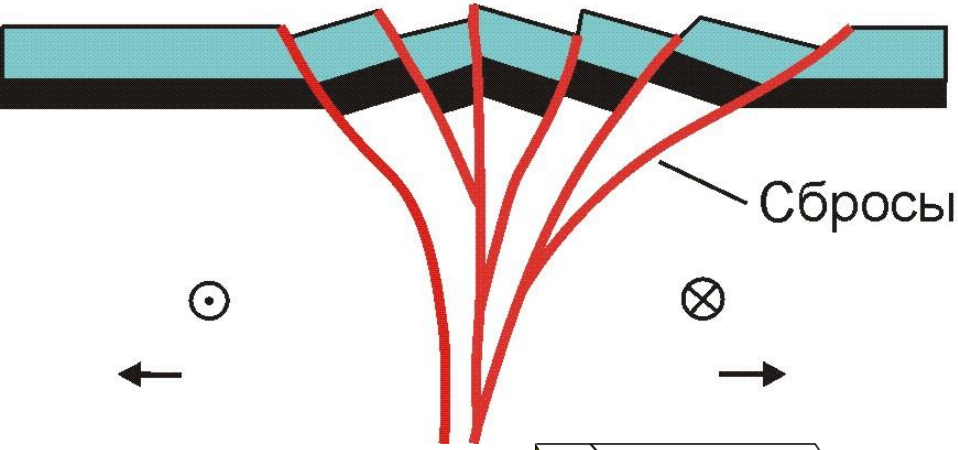

Положительная цветковая структура (сдвиго-сжатие, транспрессия)

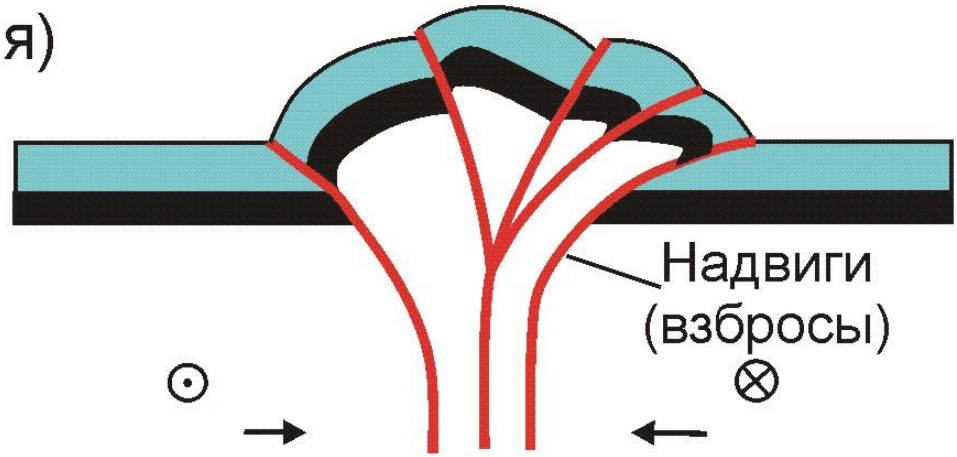

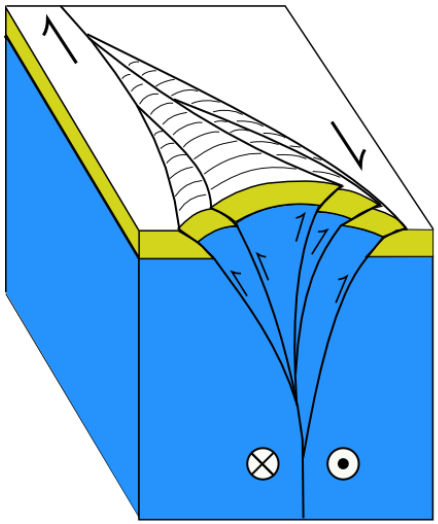

Positive Flower

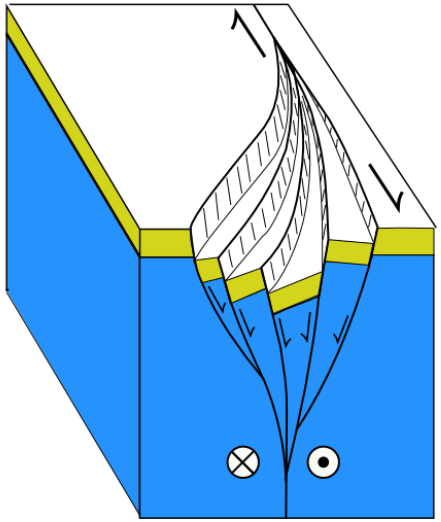

Negative Flower

4D analogue modelling of transtensional pull-apart basins

Jonathan E. Wu [a,*], Ken McClay [a], Paul Whitehouse [a,1], Tim Dooley [b]

[a] Fault Dynamics Research Group, Department of Earth Sciences, Royal Holloway University of London, Egham, Surrey, TW20 0EX, UK
[b] Bureau of Economic Geology, Jackson School of Geosciences, The University of Texas at Austin, University Station, Box X, Austin, TX 78713-8924, USA

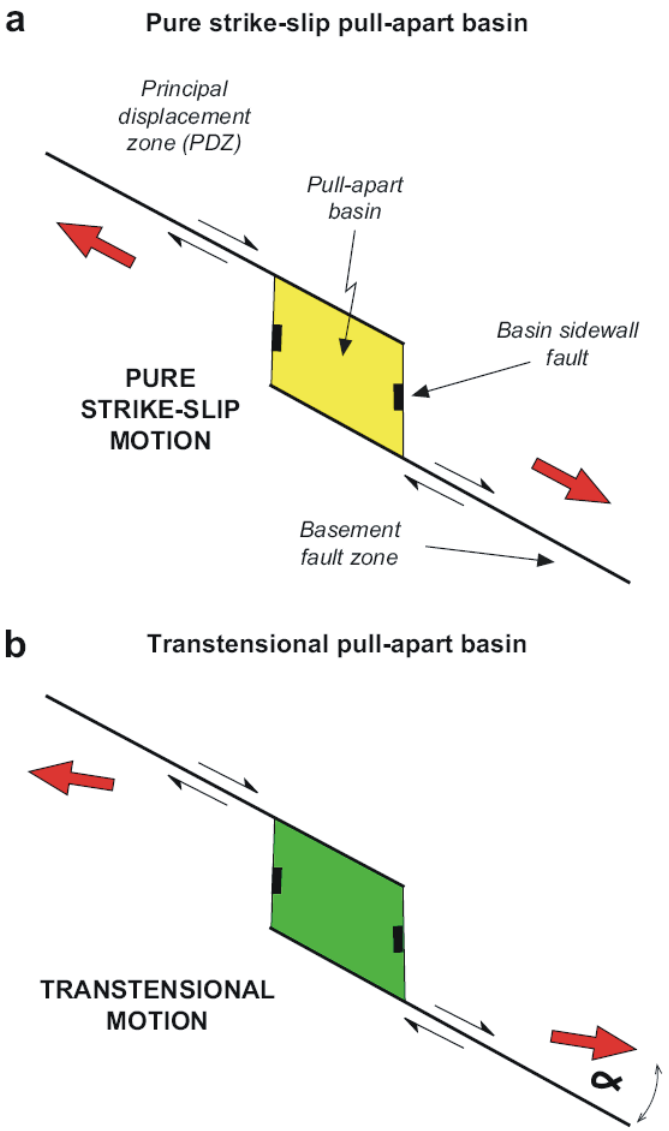

В чем отличия

J.E. Wu et al. / Marine and Petroleum Geology 26 (2009) 1608–1623

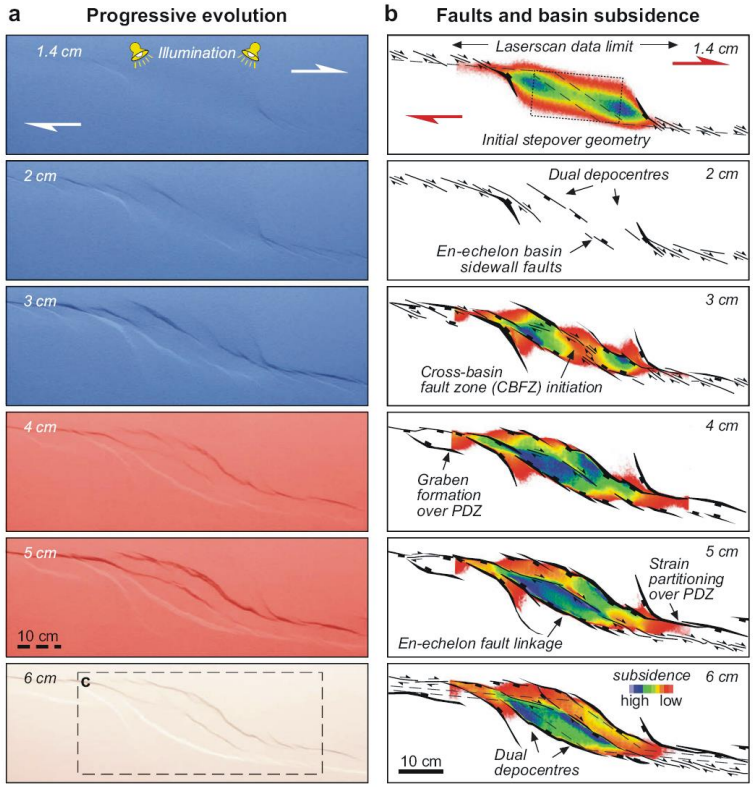

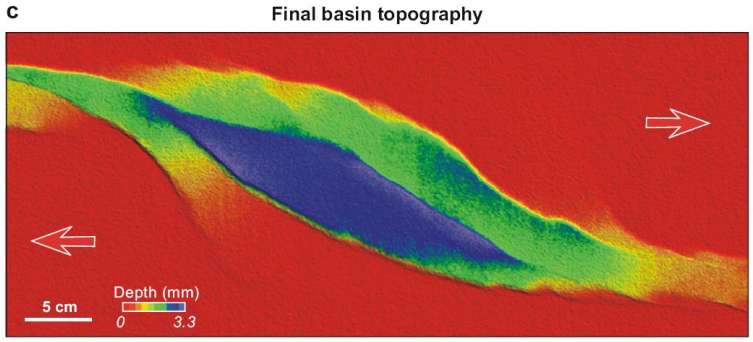

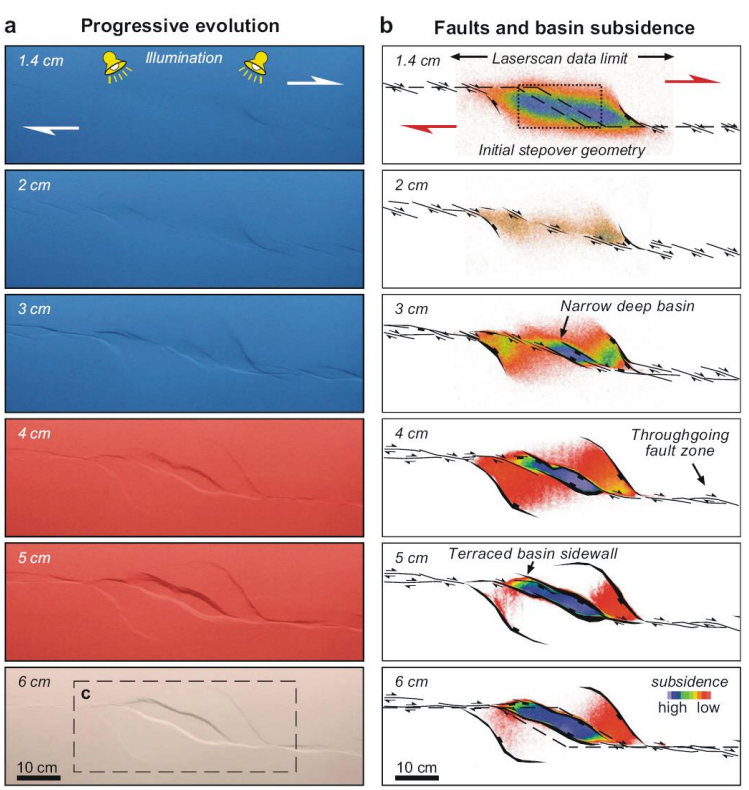

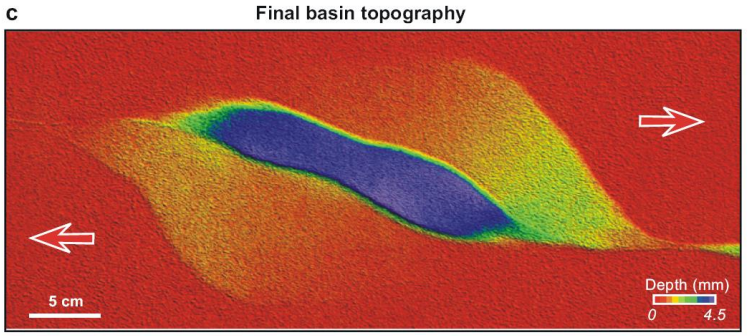

Сдвиг с растяжением

J.E. Wu et al. / Marine and Petroleum Geology 26 (2009) 1608–1623

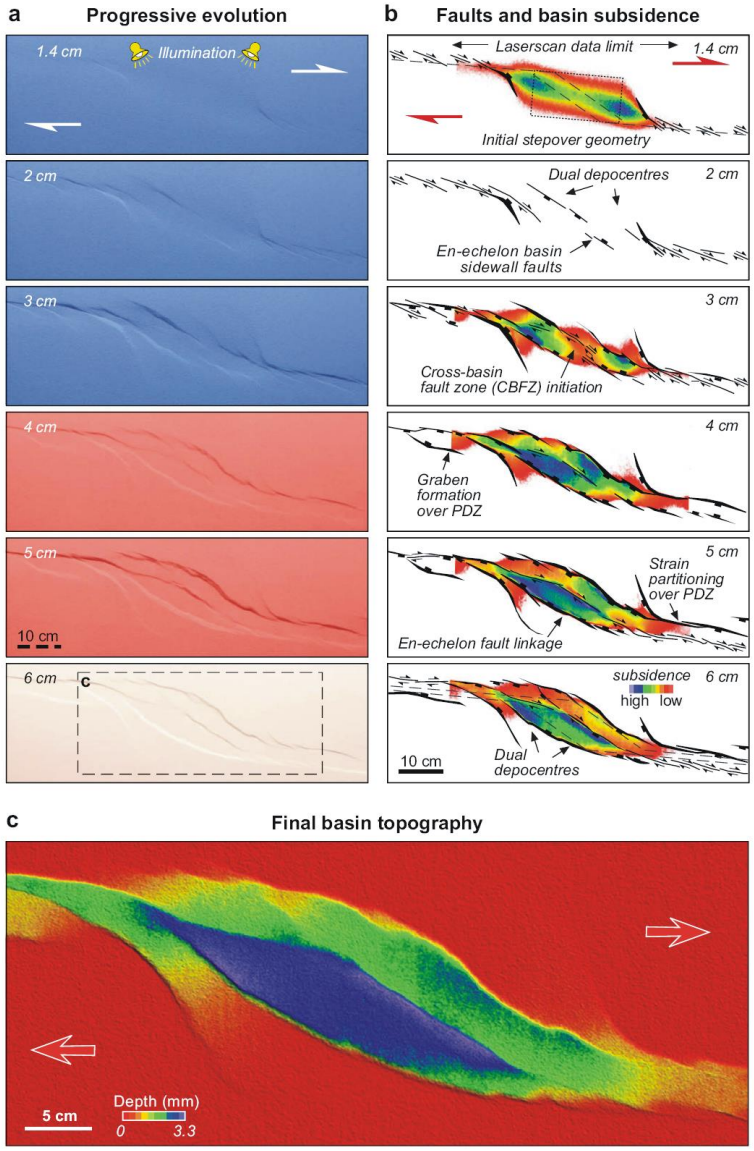

Чистый сдвиг

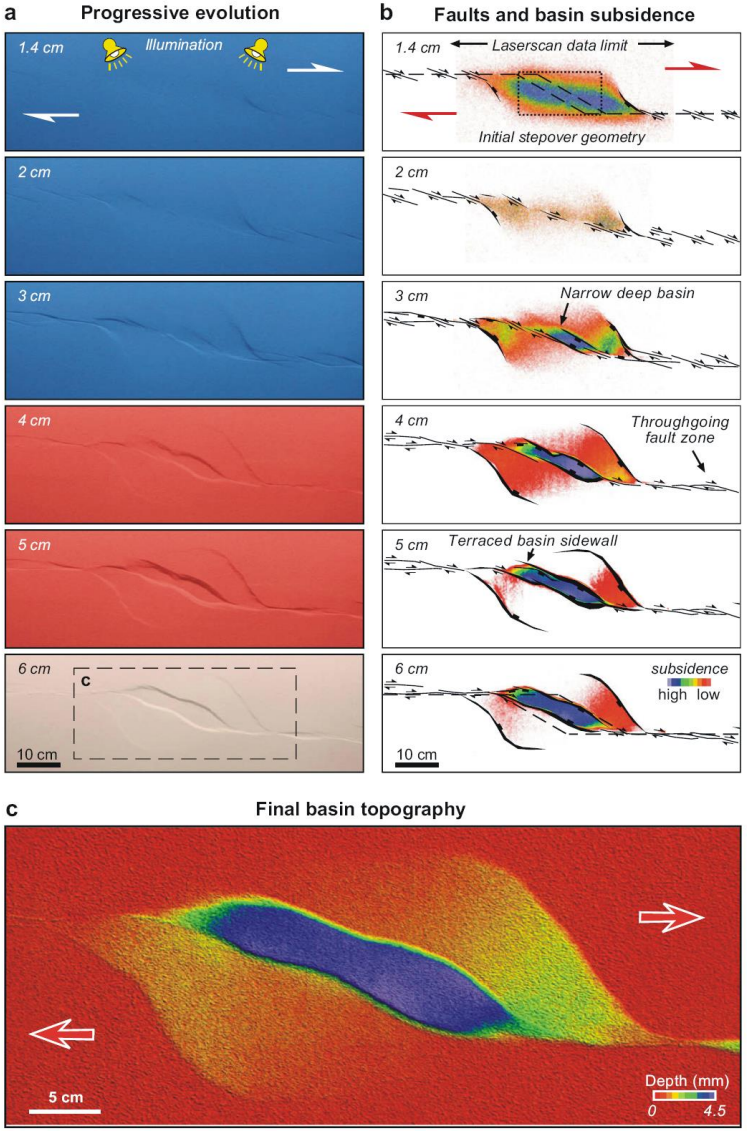

4D analogue modelling of transtensional pull-apart basins

Jonathan E. Wu [a,*], Ken McClay [a], Paul Whitehouse [a,1], Tim Dooley [b]

[a] Fault Dynamics Research Group, Department of Earth Sciences, Royal Holloway University of London, Egham, Surrey, TW20 0EX, UK
[b] Bureau of Economic Geology, Jackson School of Geosciences, The University of Texas at Austin, University Station, Box X, Austin, TX 78713-8924, USA

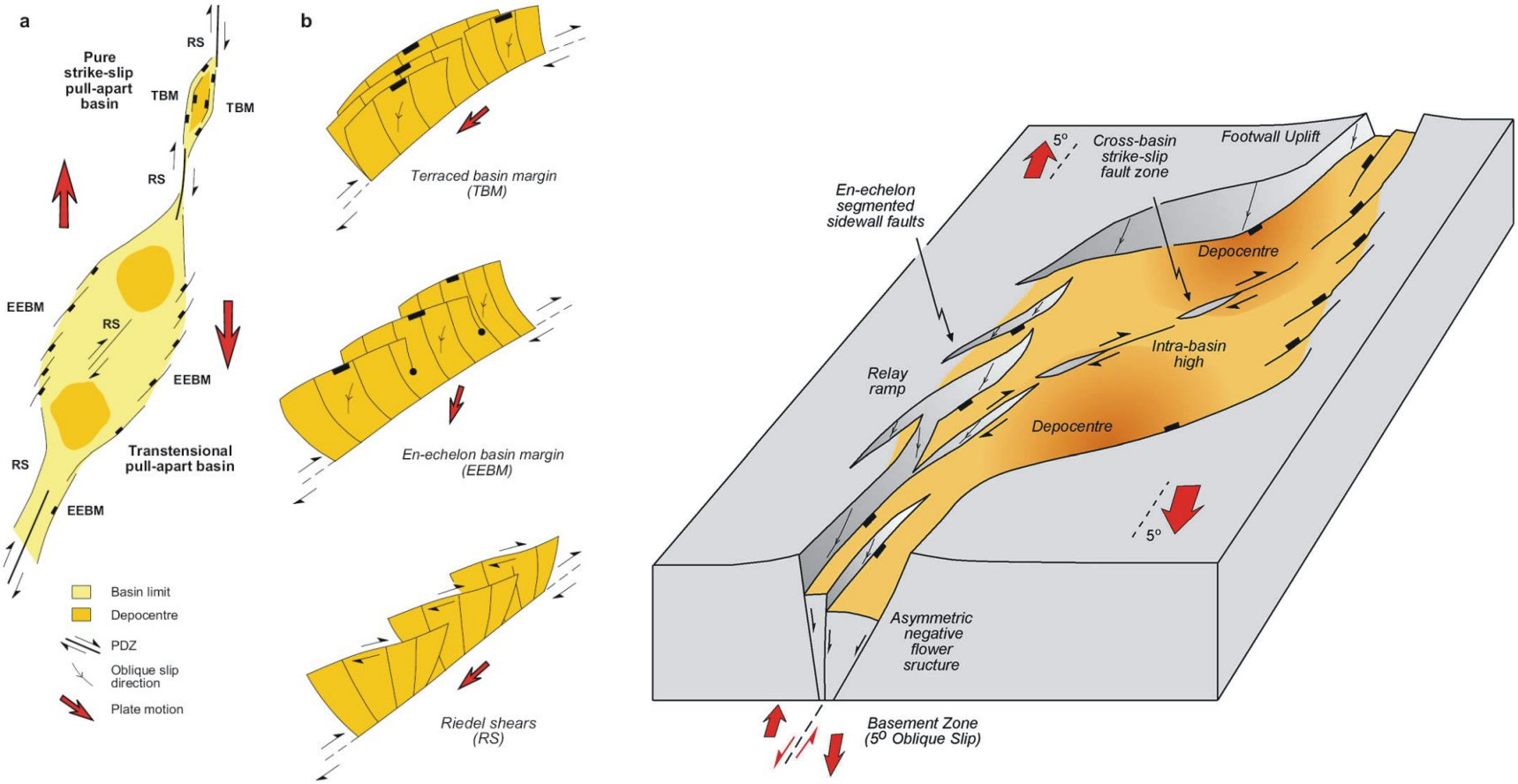

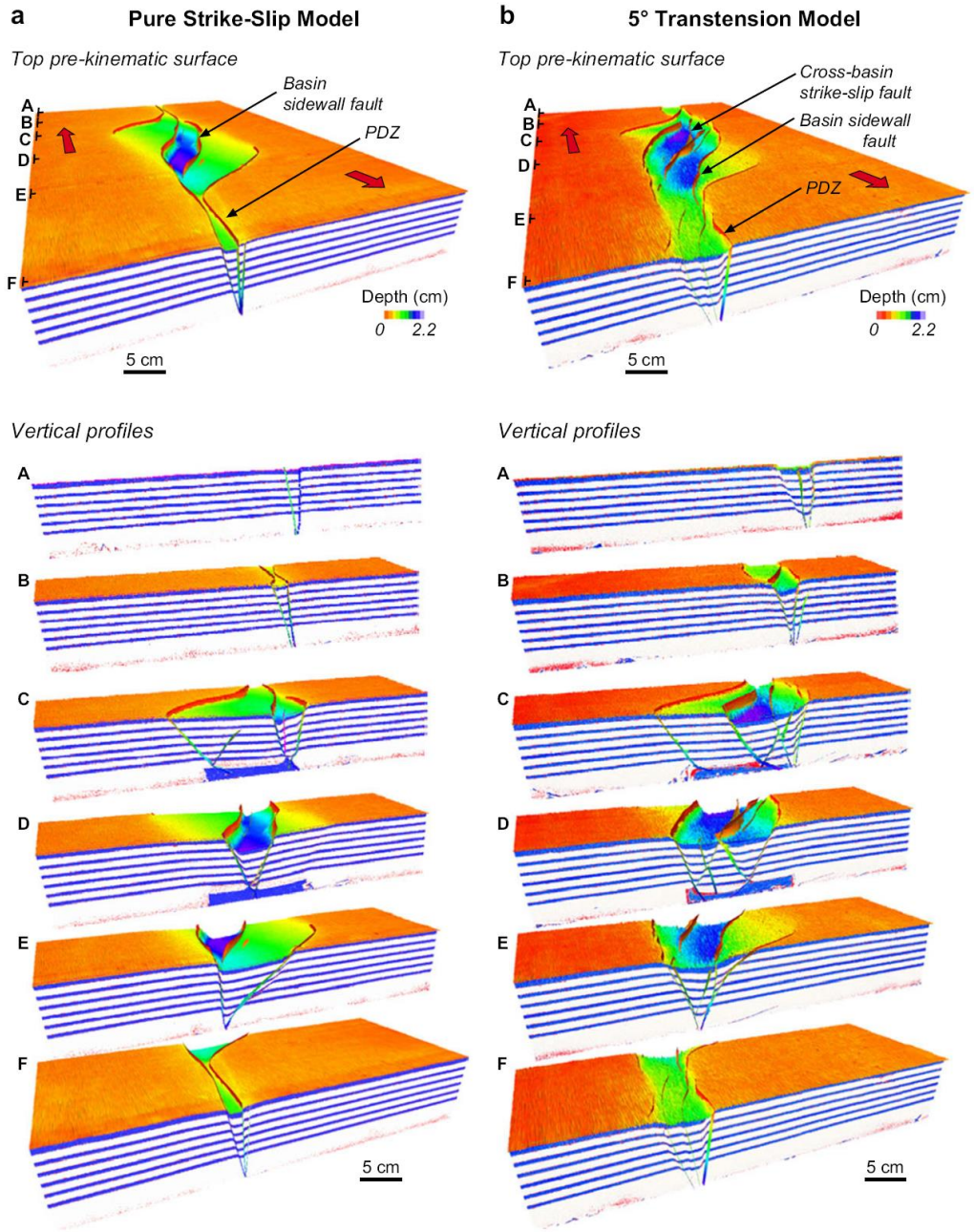

. 5. 3D visualisation of pull-apart basin model reconstructions. (a) Pure strike-slip model; and (b) transtensional model. The top surface is the top of the pre-kinematic sequence.

Физические модели систем горизонтального смещения

Вид на карте модели глинистого слоя, на котором можно увидеть развитие вторичных структур в зоне сдвига вправо.

Увеличение смещения на сдвиговом сбросе от (A) к (B).

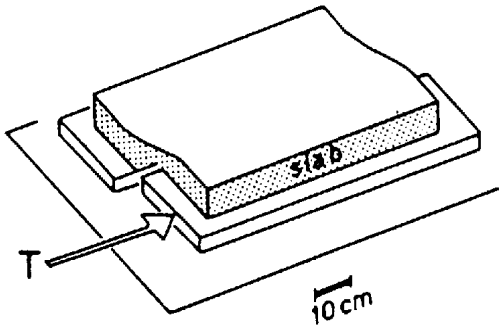

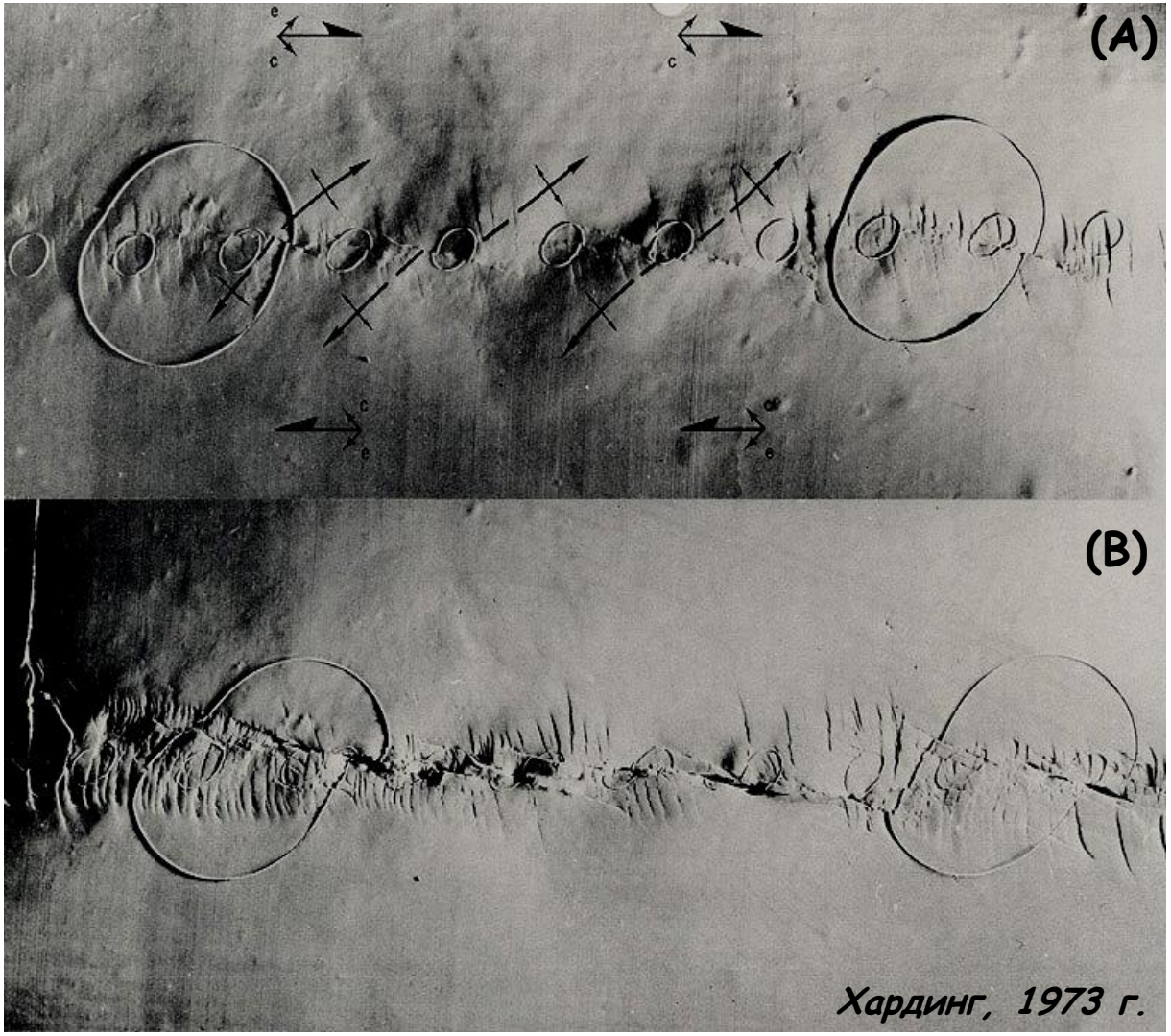

Семинский, Когут, 2008

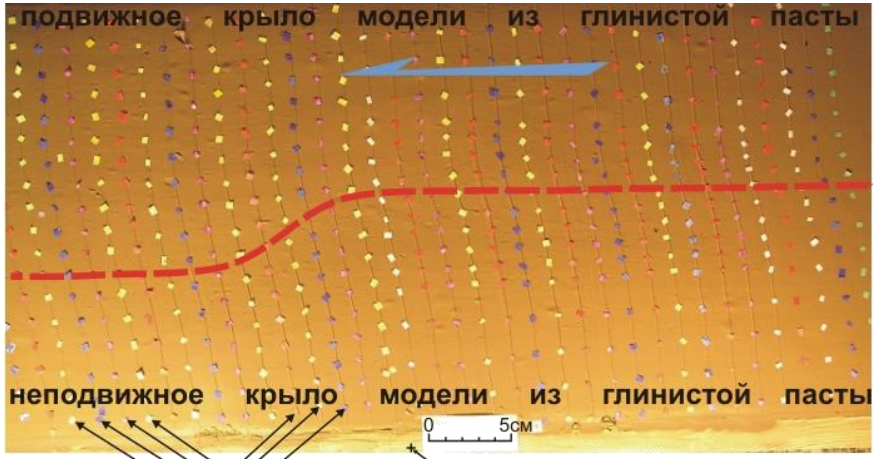

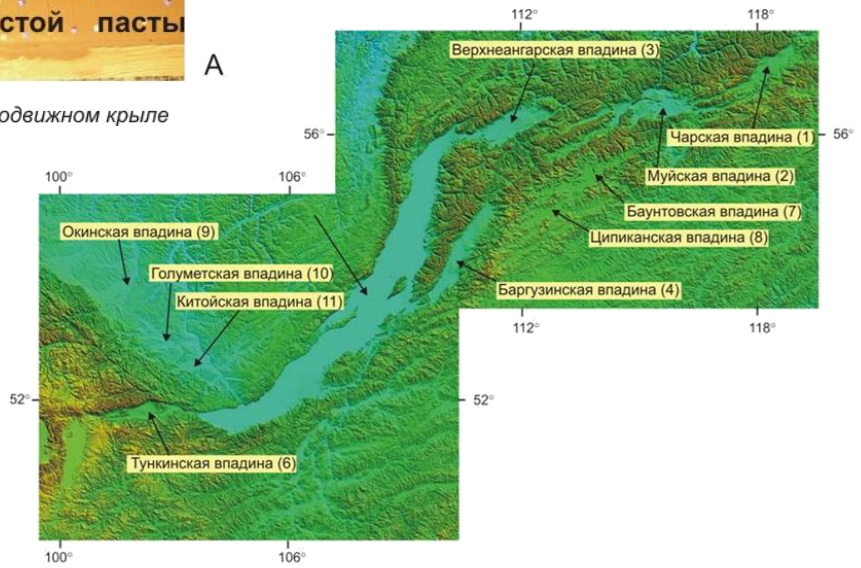

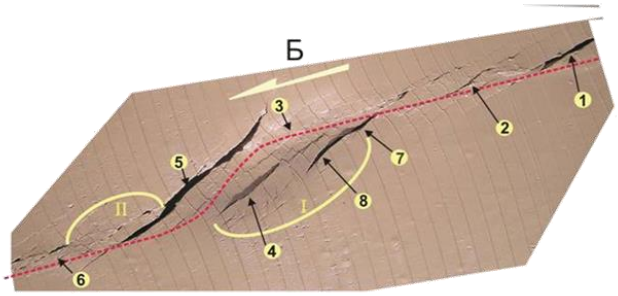

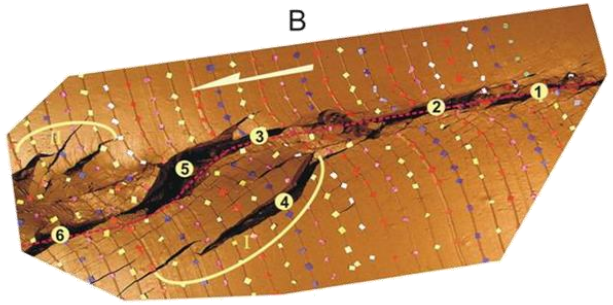

Семинский, Когут, 2008

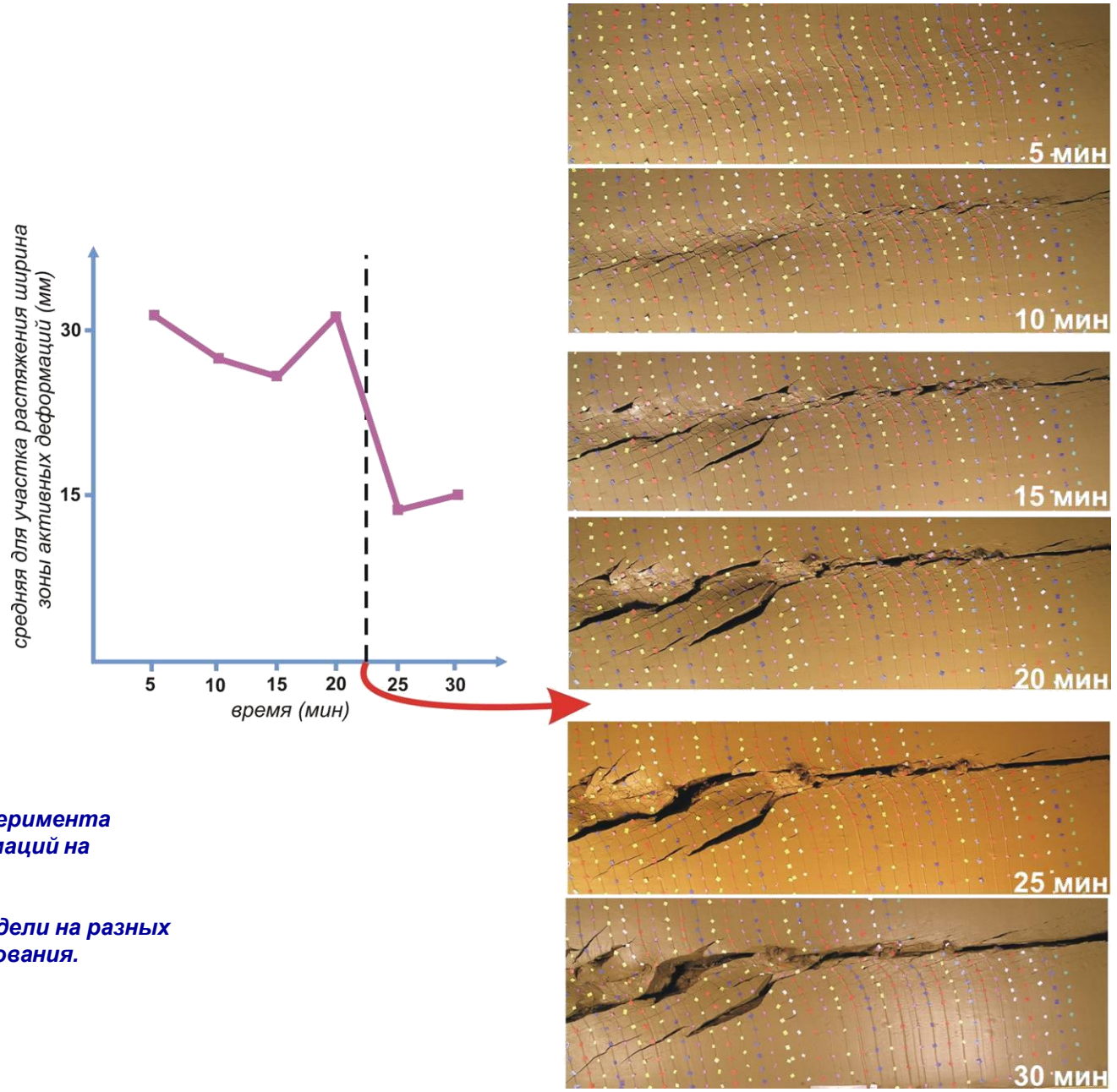

А. График изменения в ходе эксперимента ширины зоны активных деформаций на участке растяжения модели.

Б. Фотографии поверхности модели на разных временных этапах ее деформирования.

H.-U. Schwarz, F.-W. Kilfitt / Journal of Structural Geology 30 (2008) 1126–1137

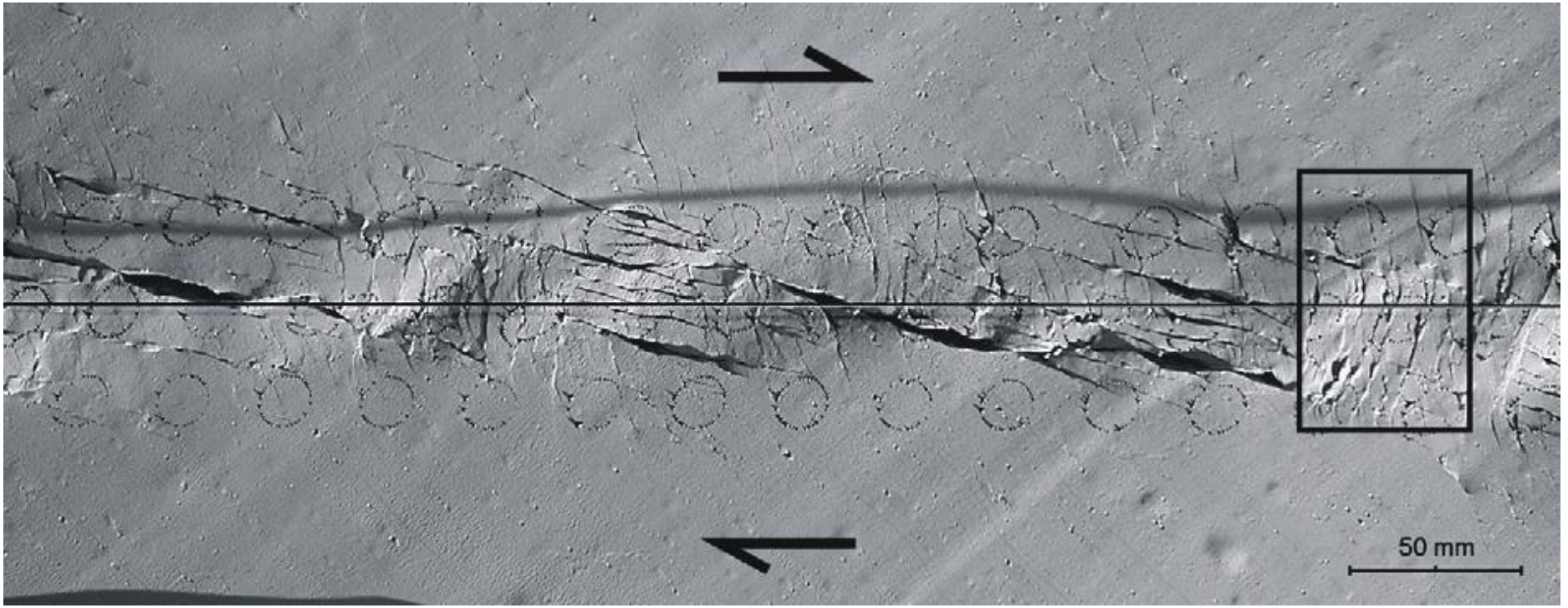

Final stage of simple shear experiment V31 (cf. Table 1) on the parallel dislocation stage with transpression folds and domains of synthetic and antithetic fault sets. Synthetic faults are partly open (black), antithetic faults are compressed and strongly rotated in the central sections. Note thrusting of the faulted blocks with their acute angle corner. The boxed area is the site of detailed drawings of Fig. 8, actually that of Fig. 8j. Black line: position of the table shear plane. Deformed markers: circles of originally 15 mm in diameter.

G.de Joussineau et al. / Journal of Structural Geology 29 (2007) 1831e1842

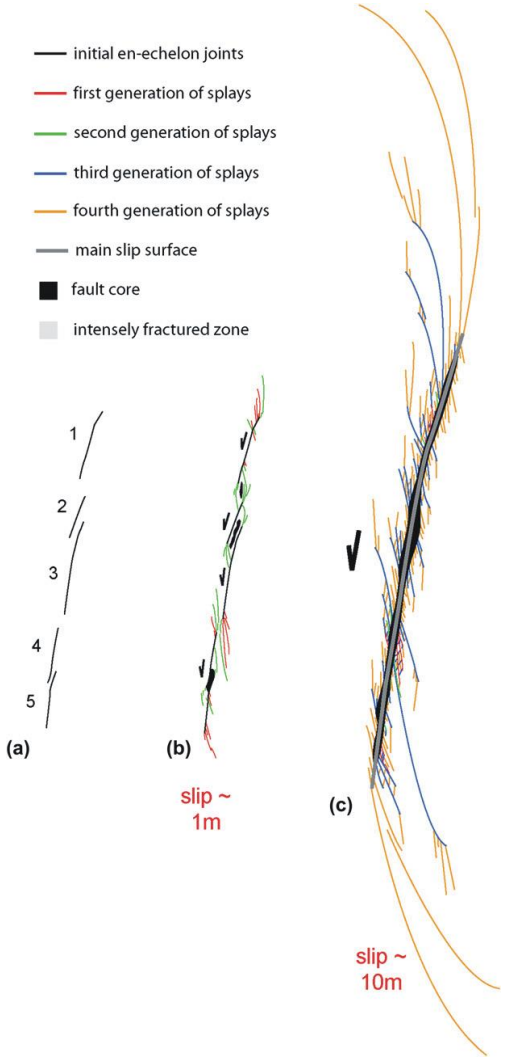

Conceptual model for damage zone evolution with fault growth in the Valley of Fire State Park, Nevada. (a) Initial joint zone. (b, c) Progressive fault growth by segment linkage with the associated successive episodes of splay fracturing (different splay generations color-coded), as a function of the amount of fault slip. Simplified from de Joussineau and Aydin (in press).

Сдвиги Риделя в 3-мерной области

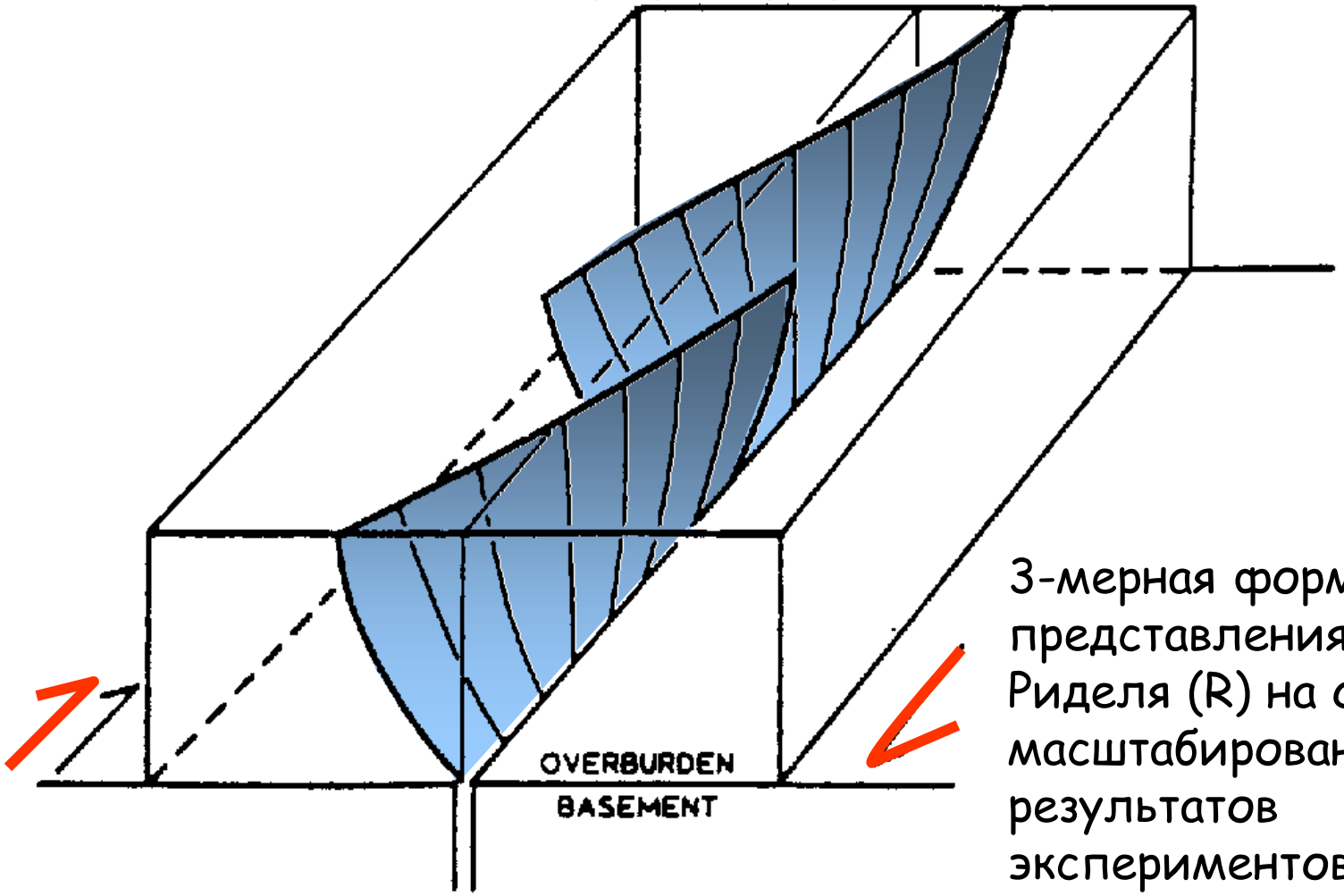

3-мерная форма представления сдвигов Риделя (R) на основе масштабированных результатов экспериментов с ящиком с песком.

Физические модели систем горизонтального смещения

Вид на карте модели глинистого слоя, на котором можно увидеть развитие вторичных структур в зоне сдвига вправо.

Увеличение смещения на сдвиговом сбросе от (A) к (B).

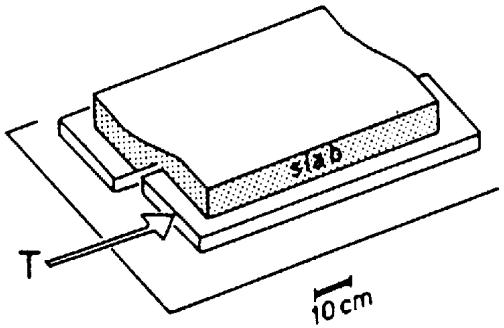

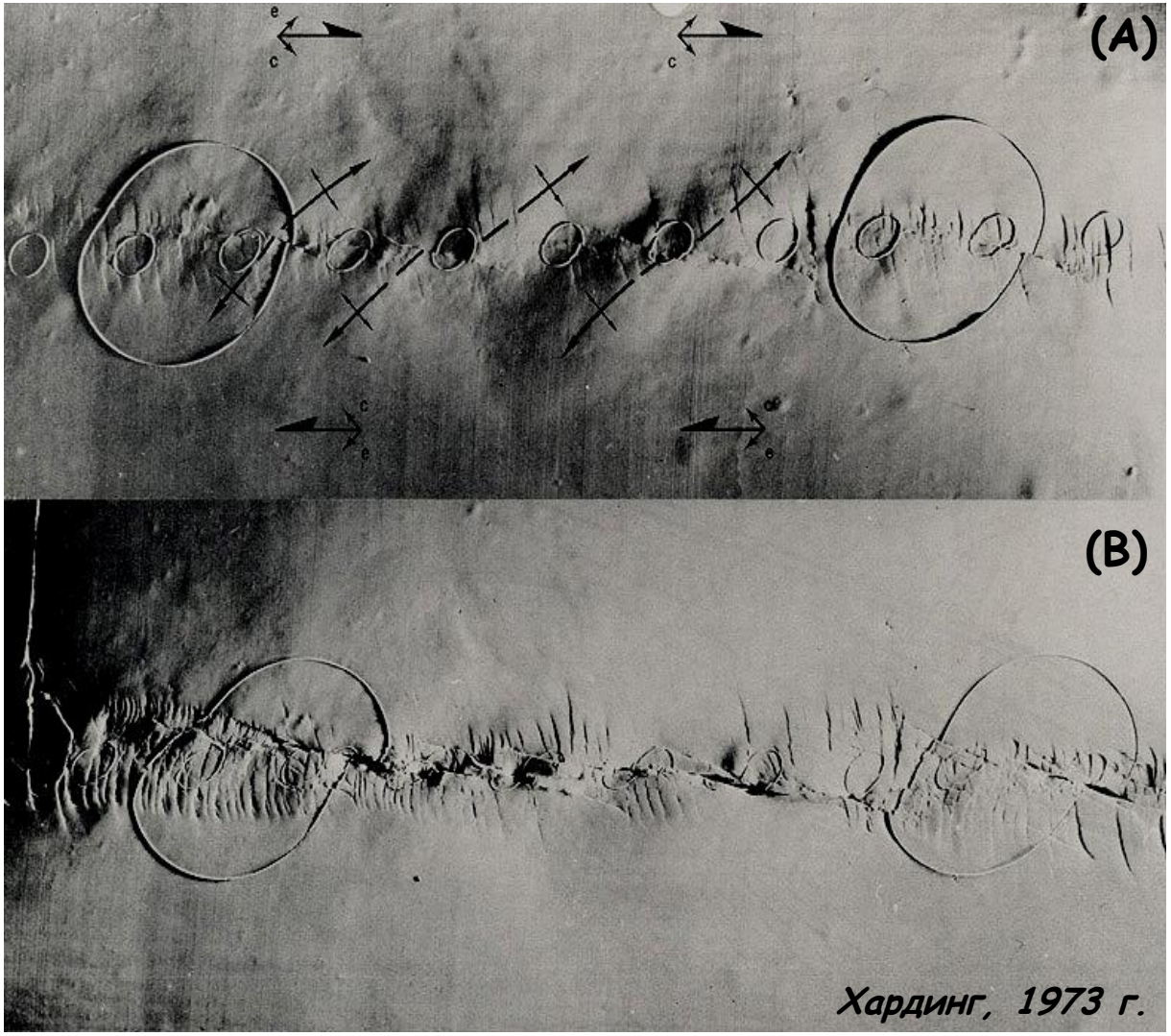

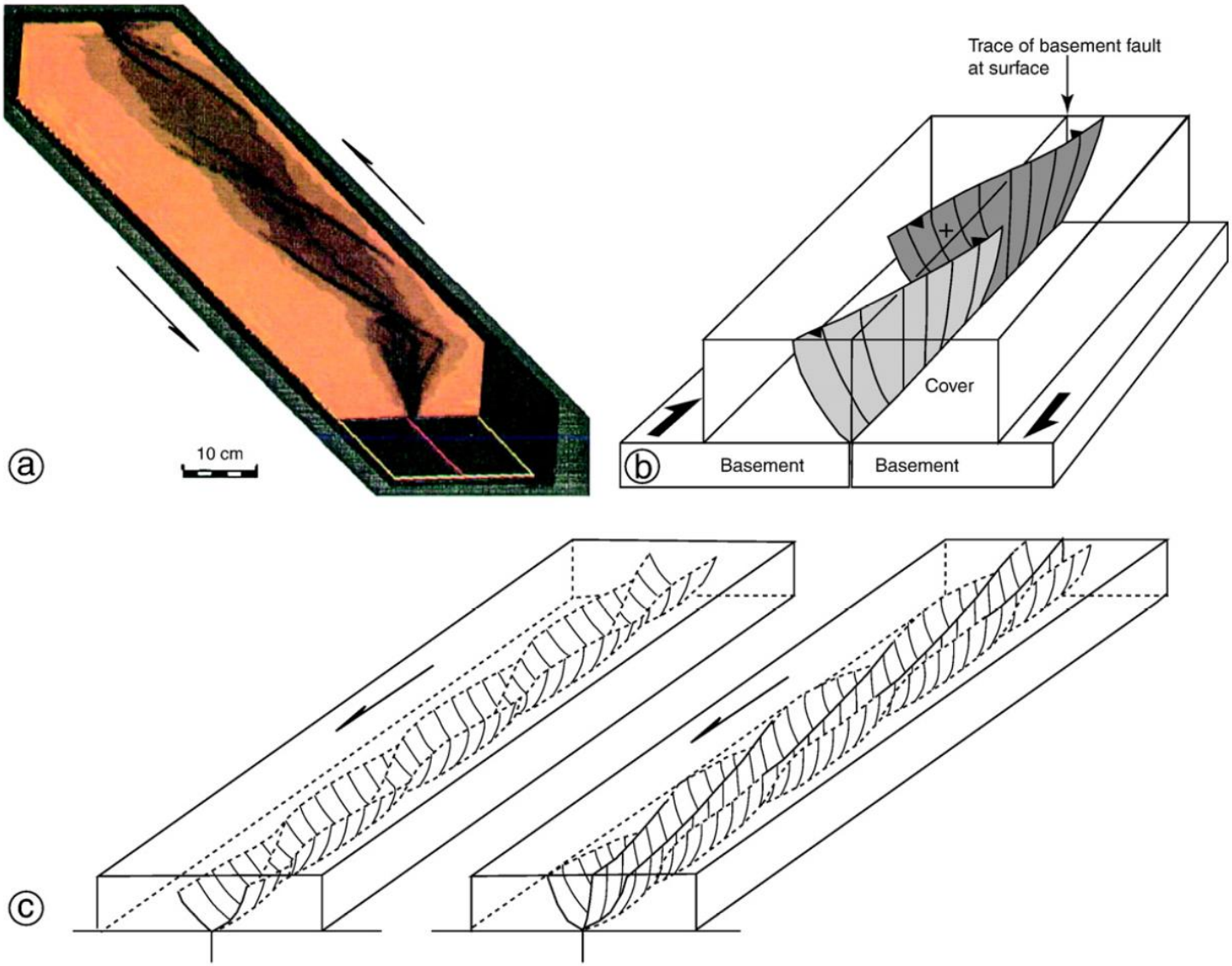

Fig. 7. Geometry of early R shears in Riedel experiments using dry sand. R shears are en echelon at the surface and root into the basement fault at depth. (a) Three-dimensional geometry of R shears in dextral Riedel experiment illustrated by X-ray computer tomography images. R shears have lower density as surrounding sand and are expressed as dark zones. (b) Helicoidal shape of en echelon and partly overlapping R shears in dextral Riedel experiment; "+" indicates uplift between R shears. (c) Schematic diagram of three-dimensional kinematic evolution of R shears after 6- (left) and 12-mm (right) displacements of one base plate resulting in sinistral shear.
a is reproduced from Richard et al. (1995), with permission of the Geological Society of London. b is redrawn from Mandl (1988). c is redrawn from Ueta et al. (2000), with permission of Elsevier.

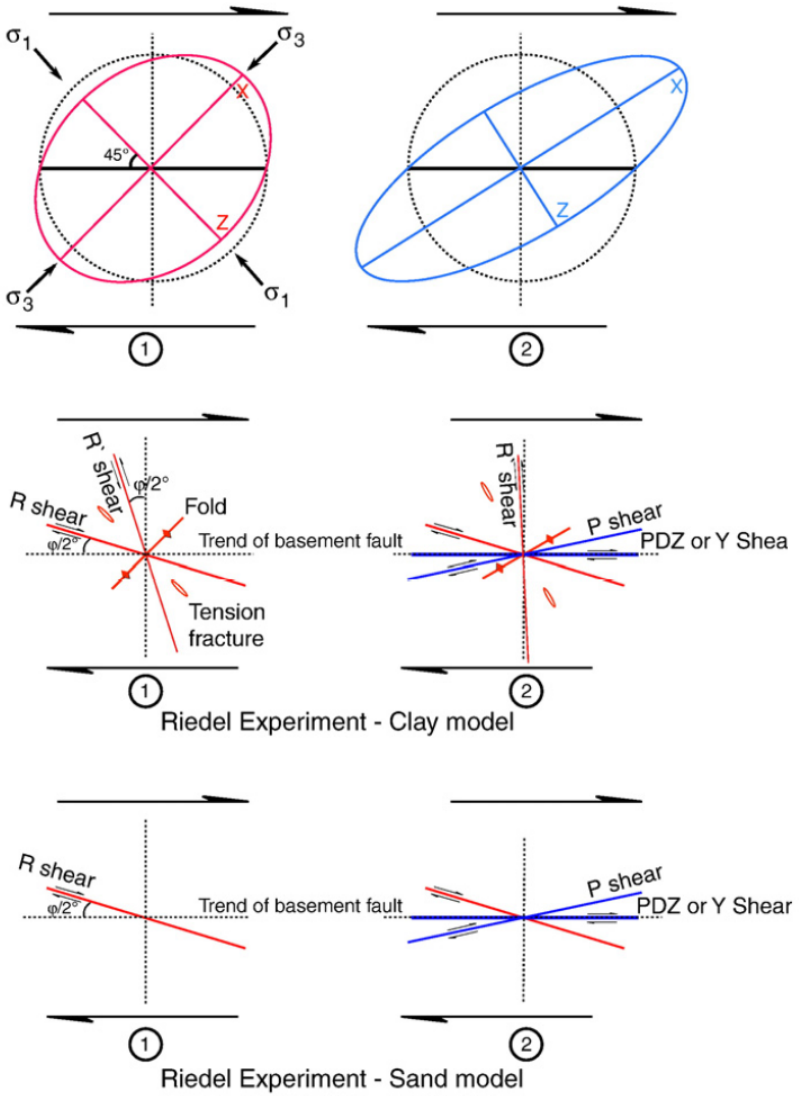

Fig. 9. Schematic sketch diagram of structures forming in the Riedel experiment at two stages of progressive dextral shear deformation for clay model and sand model. The upper diagram shows incremental strain axes and orientation of maximum and minimum compressive principal stress axes at the onset of deformation (left) and strain ellipse at a later increment of progressive dextral shear deformation. Early structures that make a large angle with shear direction rotate clockwise during progressive shear.

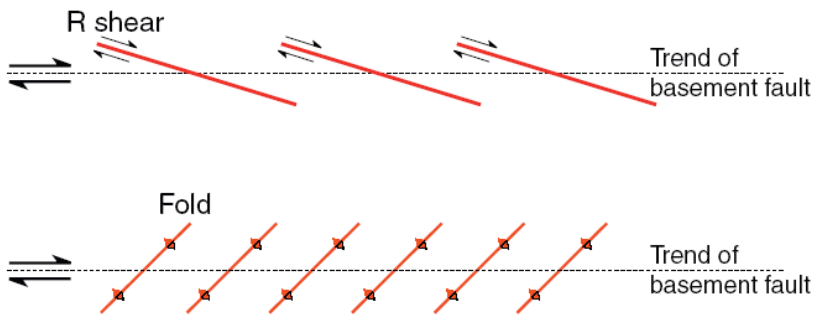

Fig. 10. En echelon structures in Riedel experiments. Left-stepping R shears and right-stepping fold hinges in the overburden indicate dextral displacement along the basement fault.

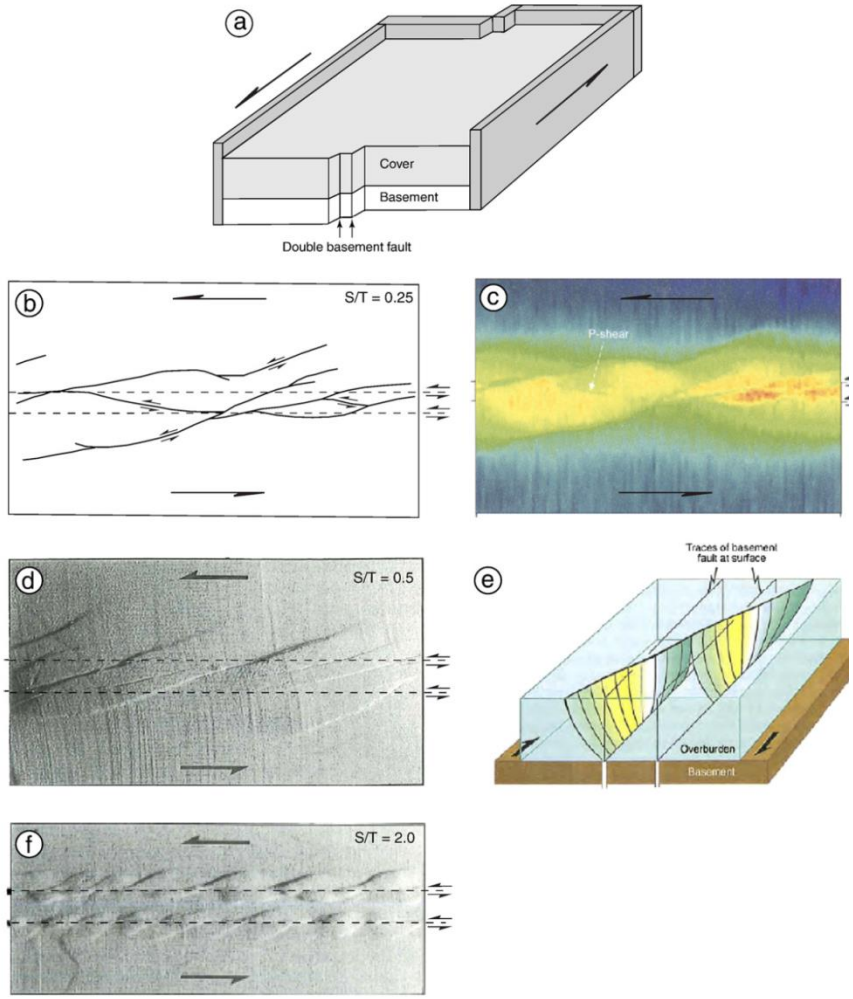

Fig. 15. Faulting in an overburden above two parallel basement faults. (a) Experimental set-up. (b–f) Fault pattern at different ratios of S/T (ratio of basement fault separation to overburden thickness). (b) Line drawing from surface photograph. (c) Corresponding horizontal X-ray CT slice at depth showing R shears and P shear. (d, f) Surface photographs of fault pattern at S/T ratios of 0.5 and 2.0, respectively. (e) Schematic block diagram illustrating three-dimensional geometry of R shears above a double basement fault.
a and b are redrawn from Schellart and Nieuwland (2003). c is reproduced from Schellart and Nieuwland (2003) and d–f are reproduced from Richard et al. (1995) with permission of the Geological Society of London. Note that d and f are mirror images of original figures.

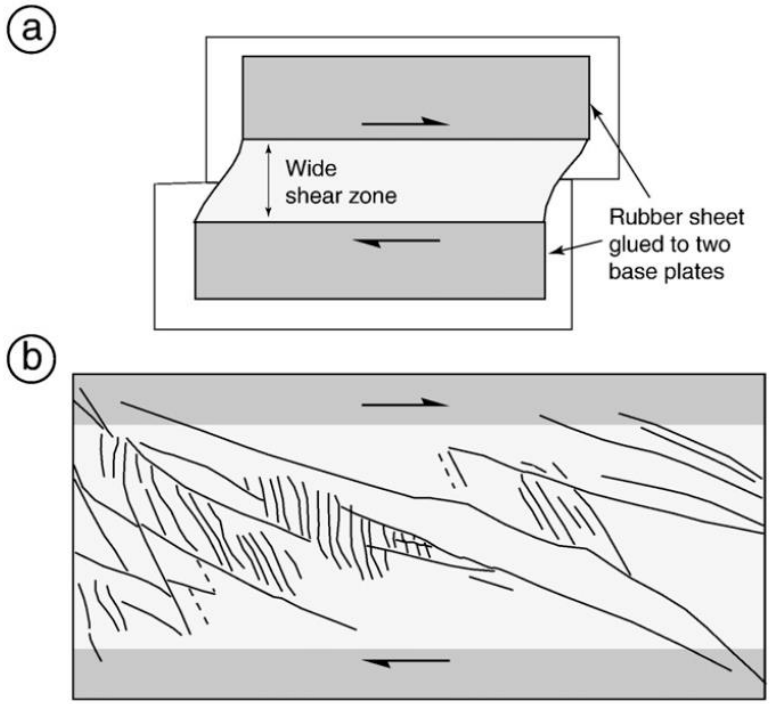

Fig. 16. (a) Riedel experimental set-up modified to obtain a wide basement shear zone. Horizontal shear displacement along basement fault is distributed over a broad zone in the cover by partly gluing a rubber sheet to each half of the shear table. (b) Fault pattern in 10-cm-thick sand pack after 15-cm horizontal displacement distributed over 30-cm-wide shear zone.
b is redrawn from Naylor, private communication in Mandl (1988).

Средний Каспий

Характер плоскостей разломов в доюрском и юрско-меловом комплексах

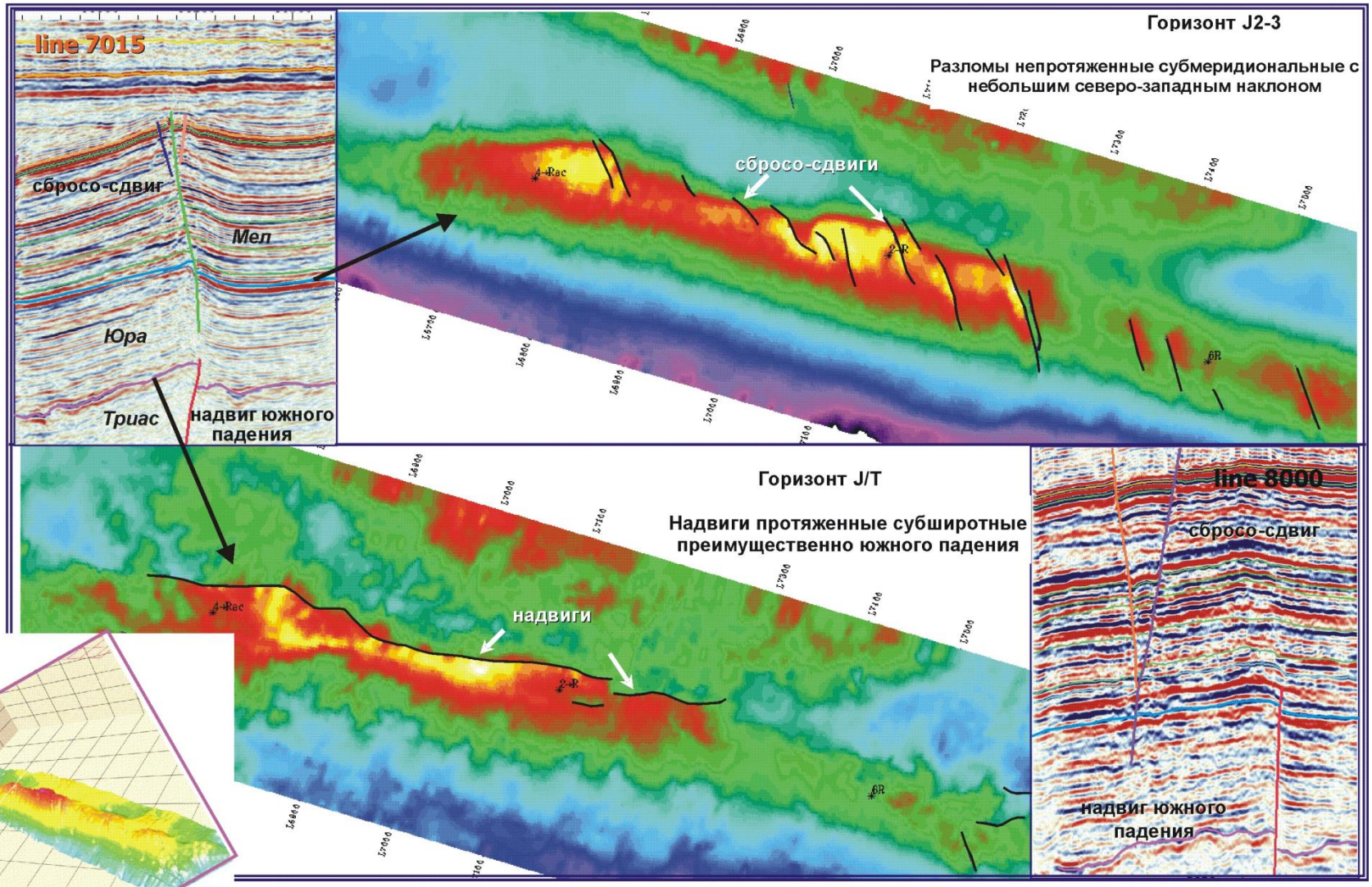

(Delia et al., 2008)

Средний Каспий

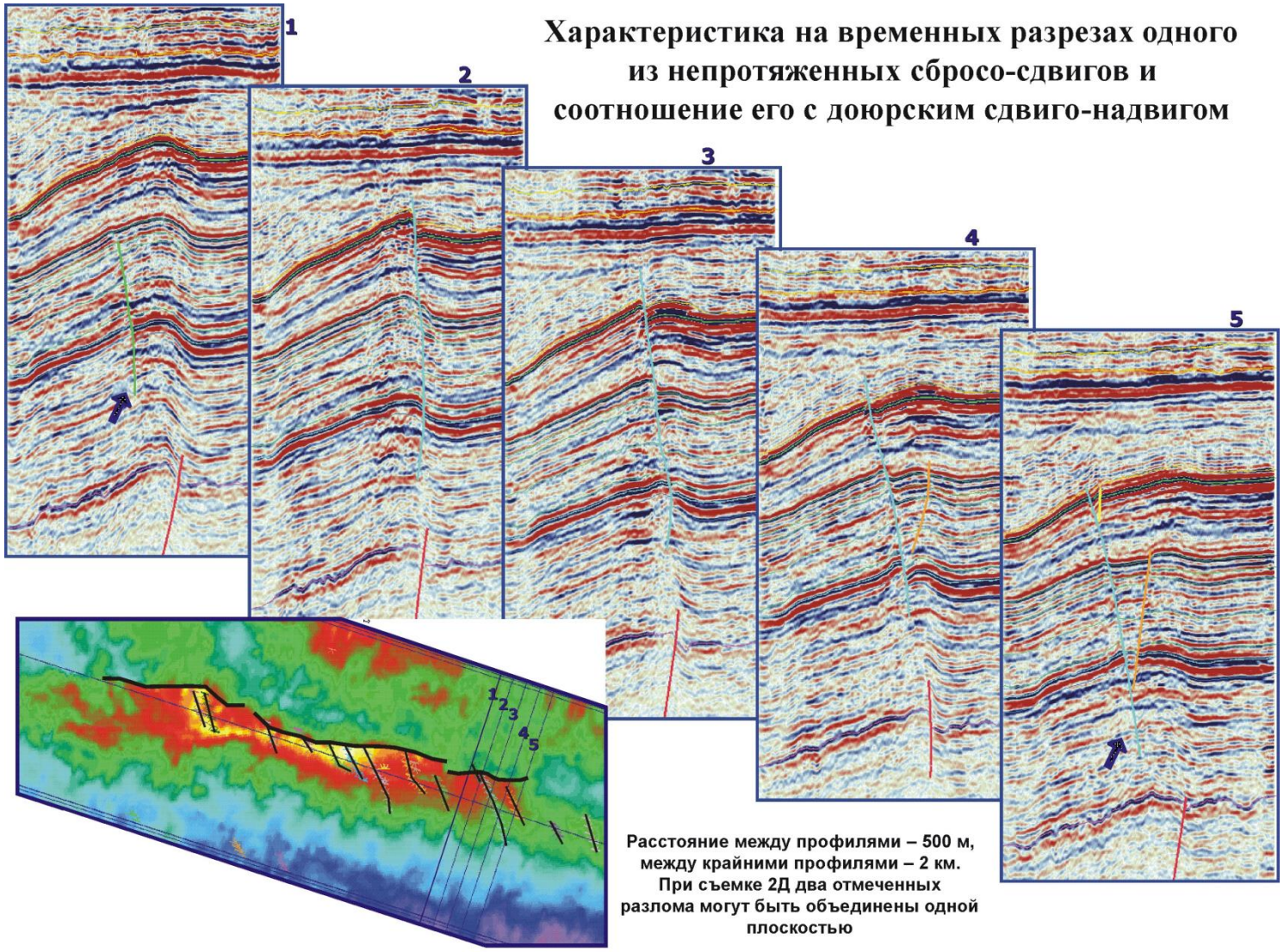

Средний Каспий

срез 1252 мс

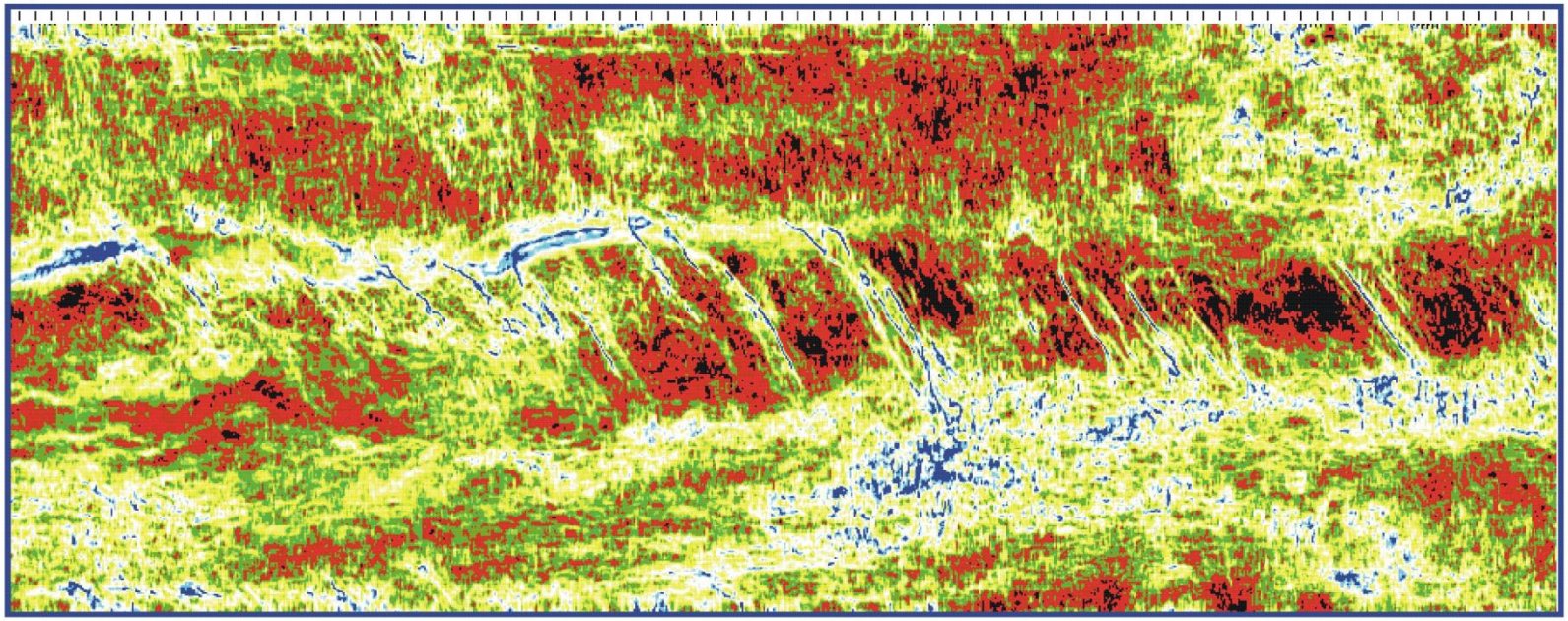

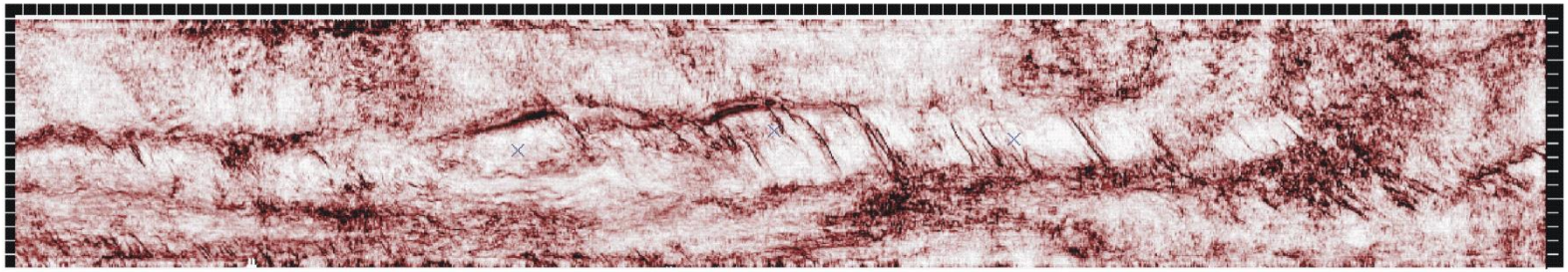

4 км

(Delia et al., 2008)

Средний Каспий

Временной разрез вдоль длинной оси складки

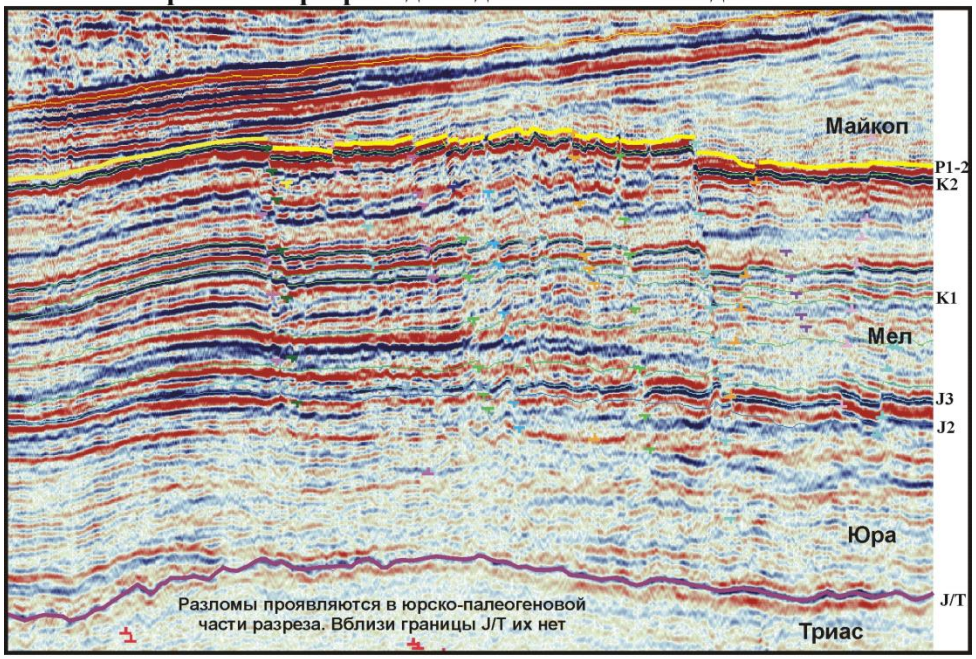

(Delia et al., 2008)

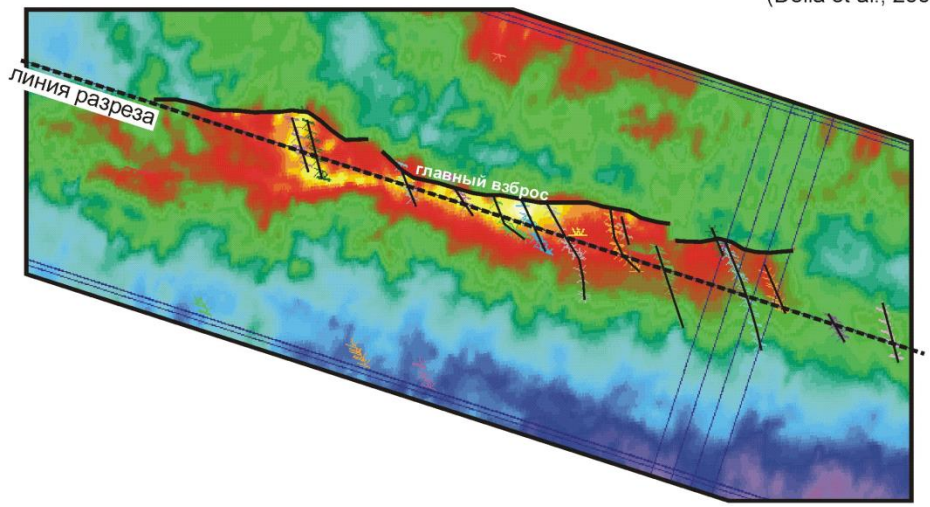

Структурная карта Западно-Сибирского бассейна по кровле альб-сеноманского комплекса

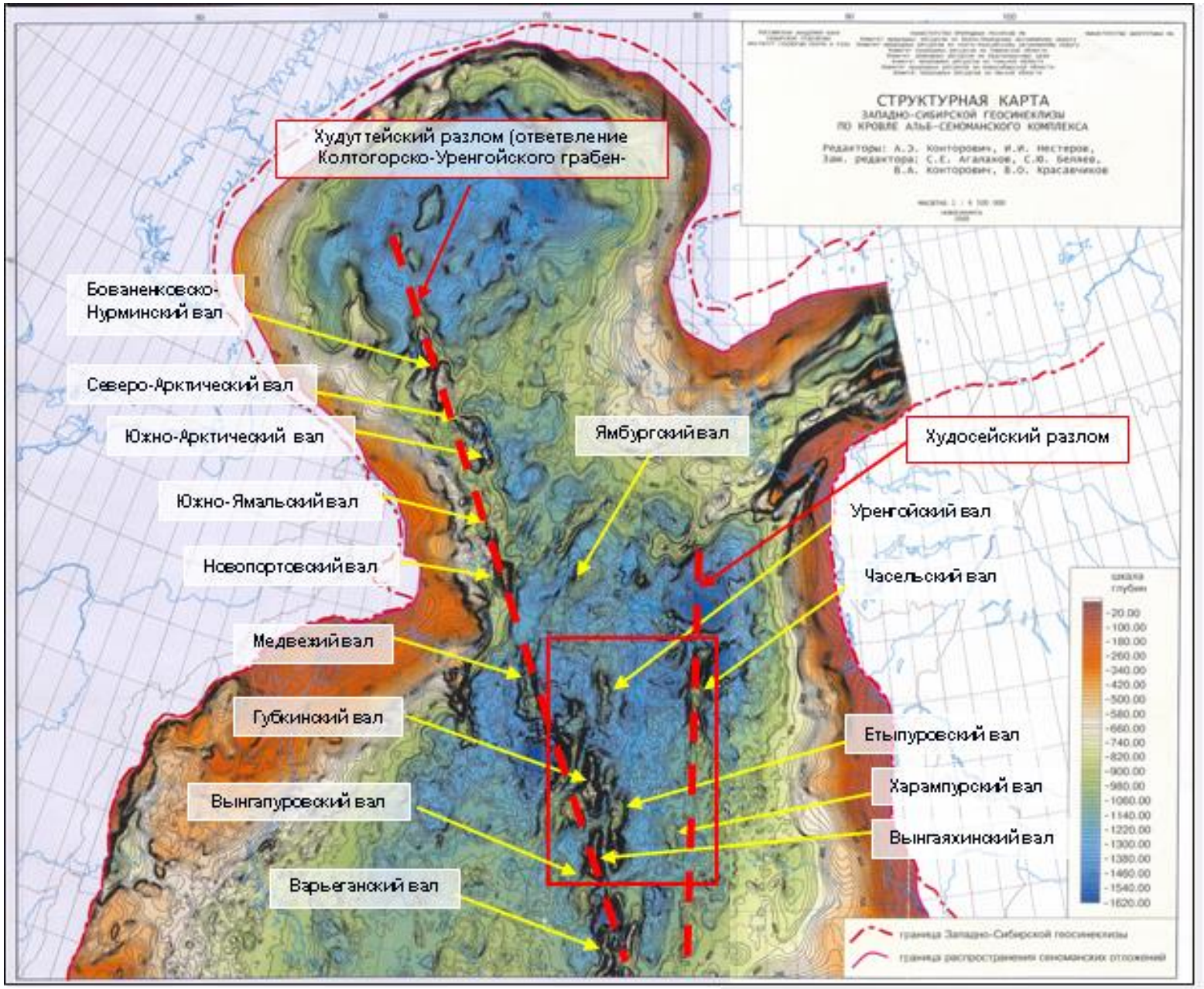

Схема расположения кулисных систем сбросов в осадочном чехле центральной части севера Западно-Сибирской плиты

Г.Н. Гогоненков, А.И. Тимурзиев и др, 2008, ЦГЭ

Структурные карты
по разным горизонтам осадочного чехла

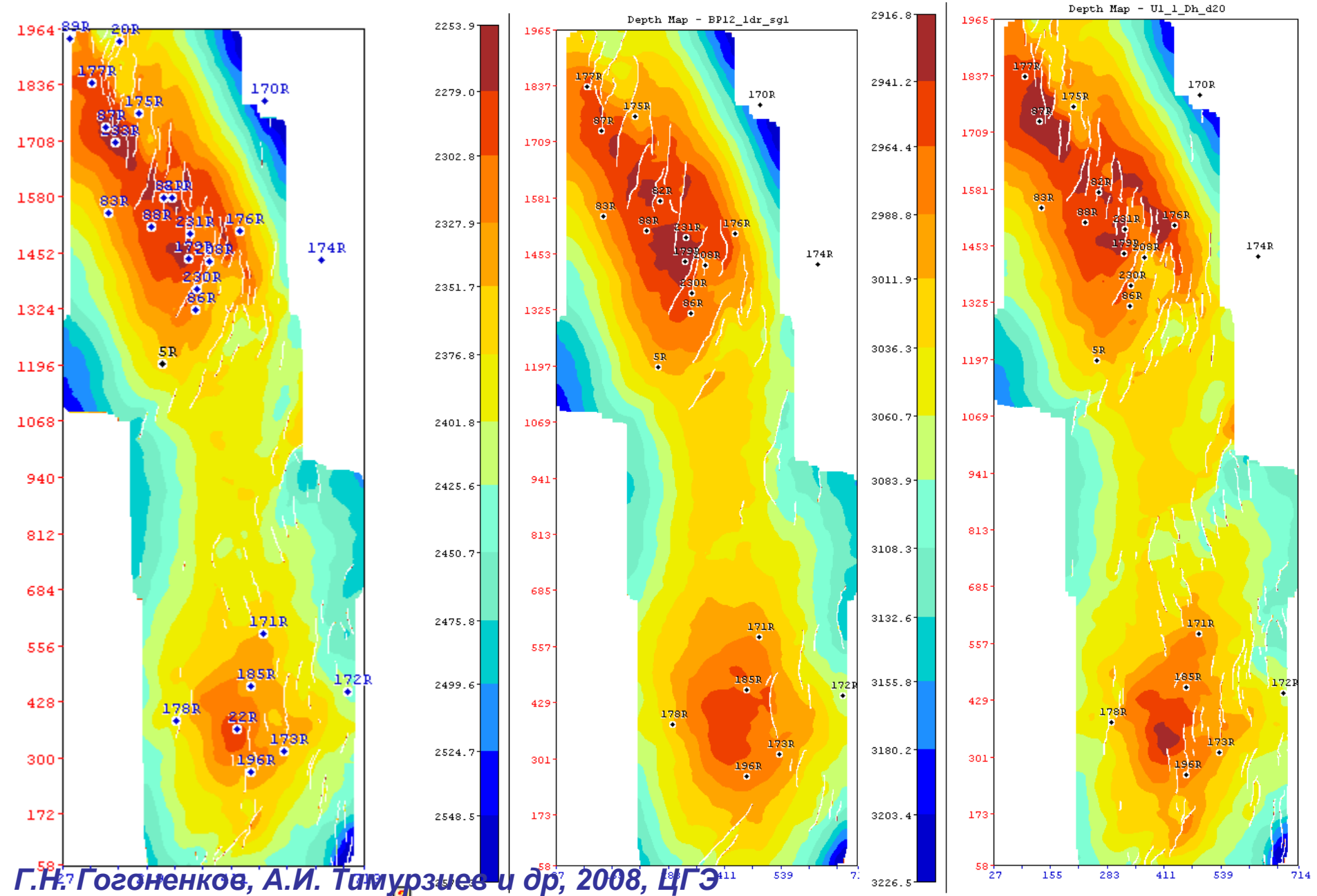

Г.Н.Гогоненков, А.И. Тамурзиев и др, 2008, ЦГЭ

Структурные карты углов падения по разным горизонтам осадочного чехла

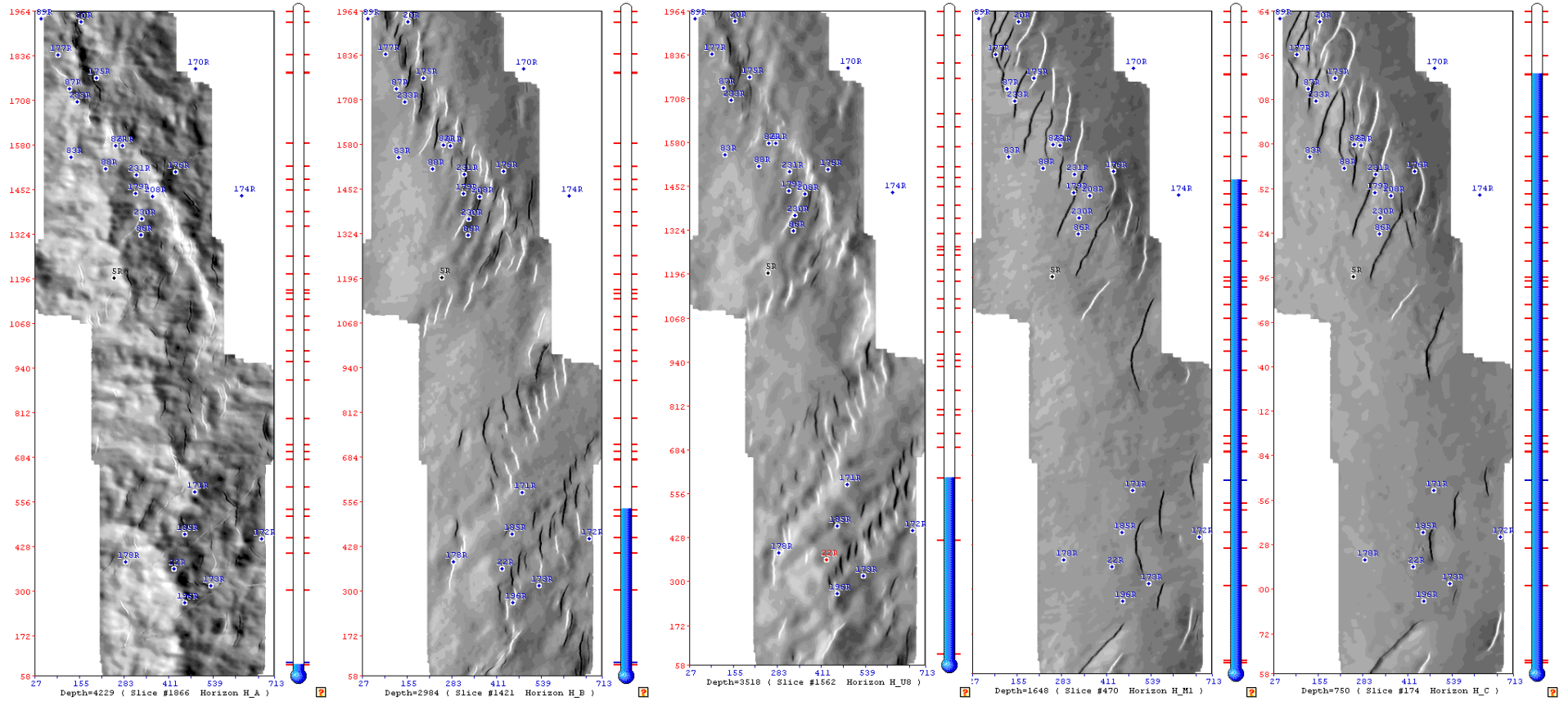

Различный тон обозначает разный угол падения структурной поверхности

Г.Н. Гогоненков, А.И. Тимурзиев и др, 2008, ЦГЭ

Геолого-сейсмические разрезы, косо пересекающие кулисные системы сбросов

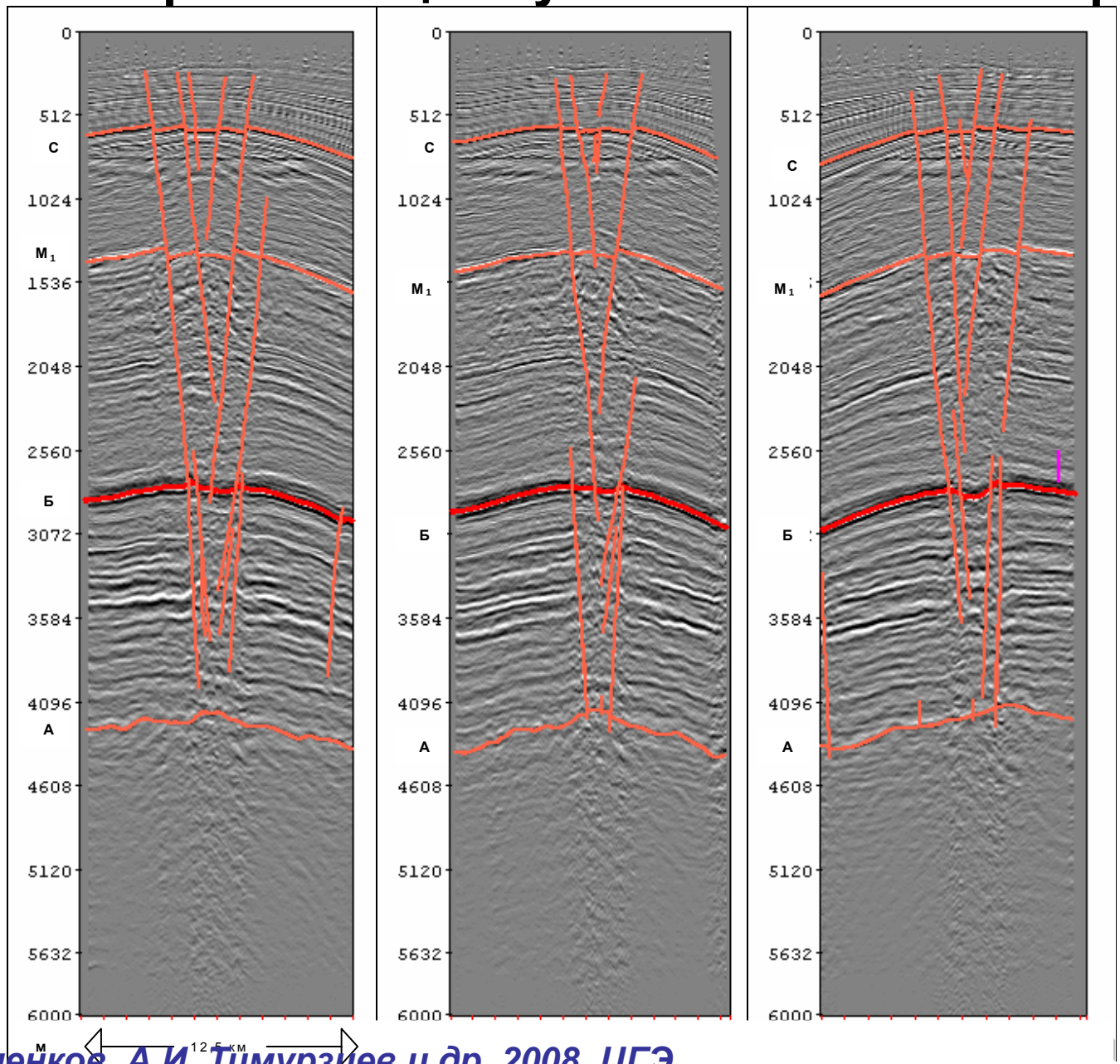

Г.Н. Гогоненков, А.И. Тимурзиев и др, 2008, ЦГЭ

Геолого-сейсмические разрезы, косо пересекающие кулисные системы сбросов

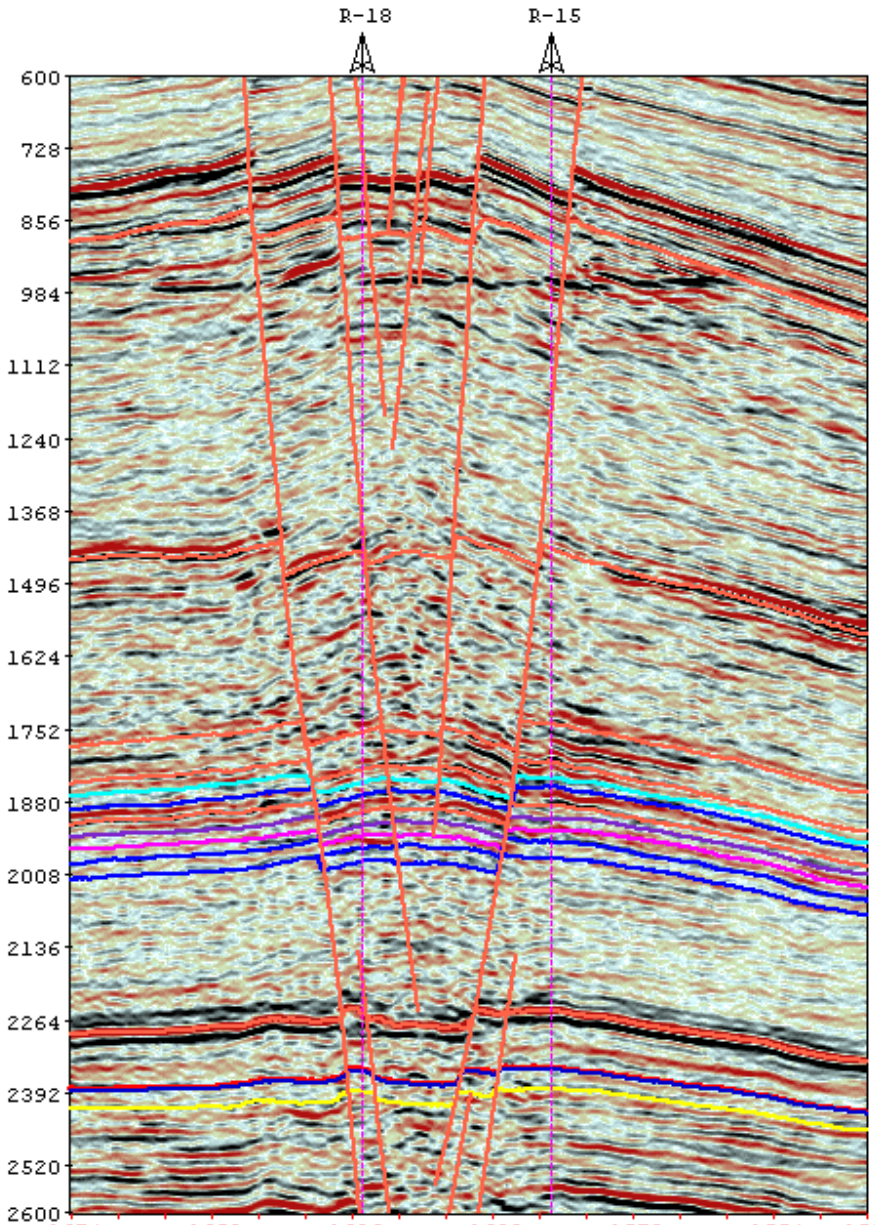

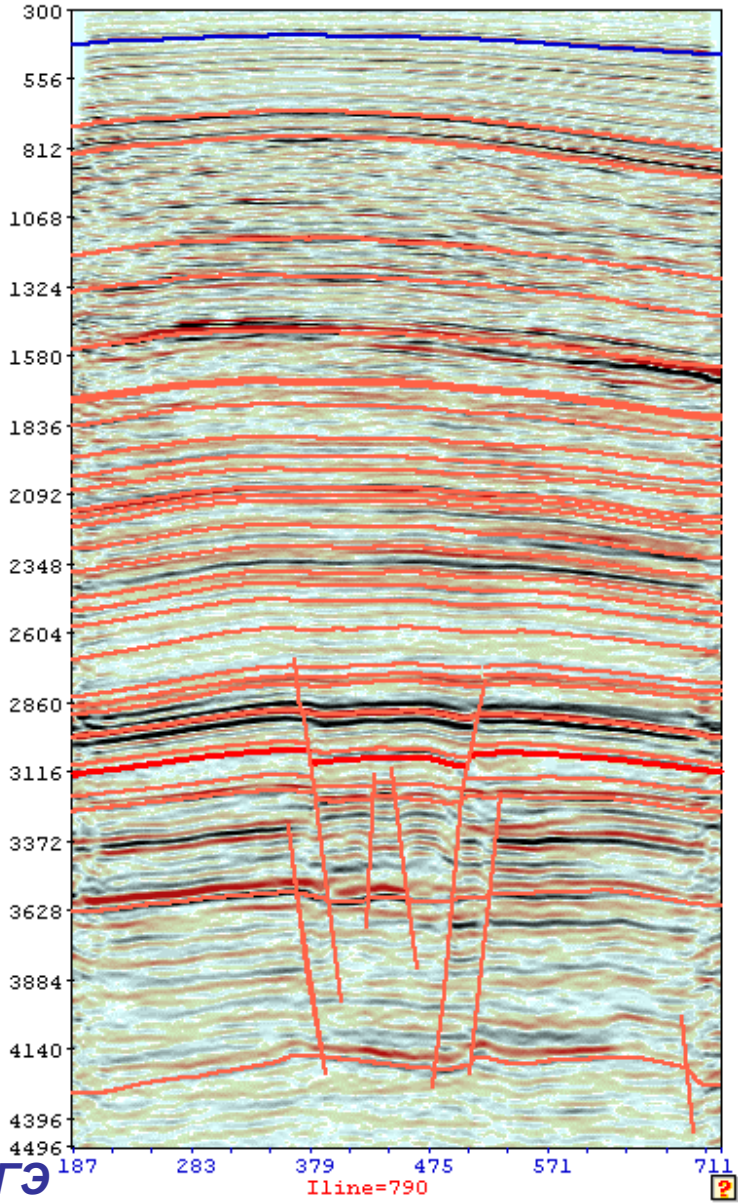

Г.Н. Гогоненков, А.И. Тимурзиев и др, 2008, ЦГЭ

Геолого-сейсмические разрезы, косо пересекающие кулисные системы сбросов

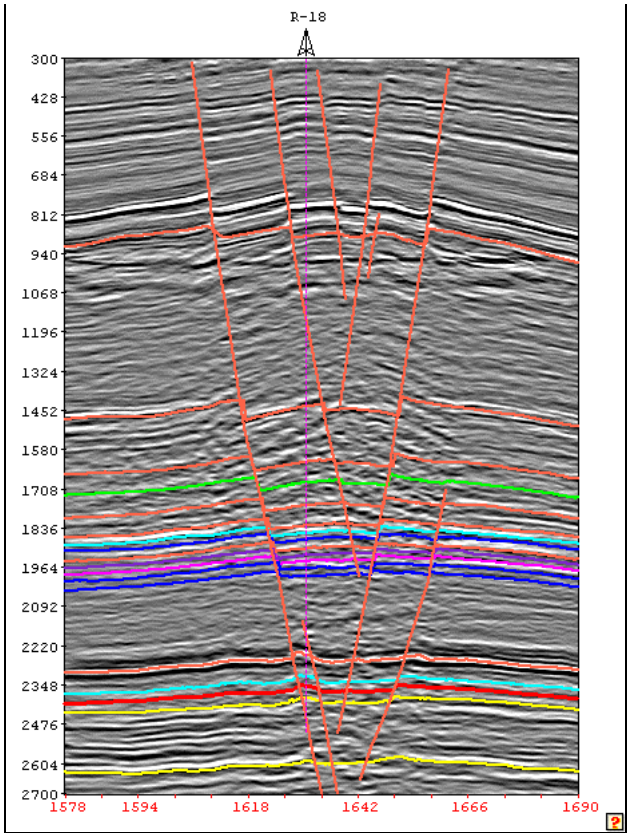

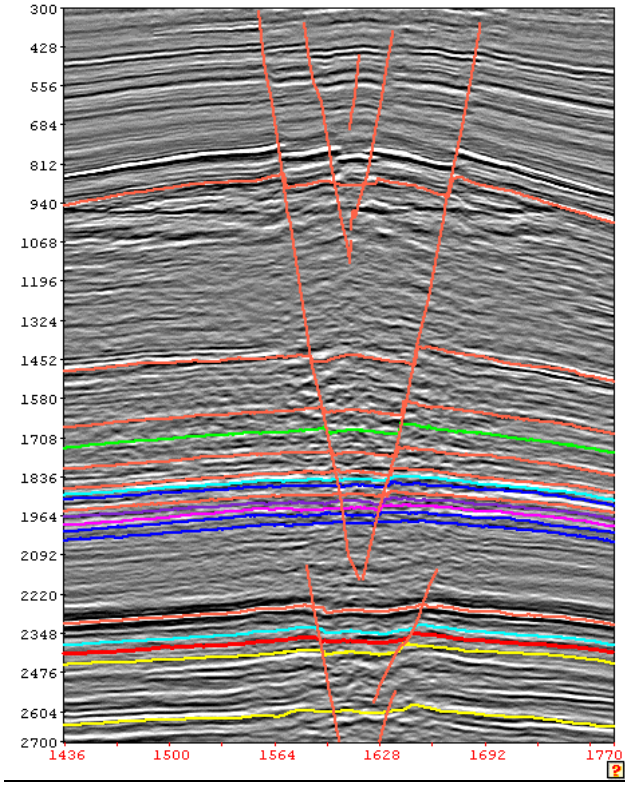

Г.Н. Гогоненков, А.И. Тимурзиев и др, 2008, ЦГЭ

Разрезы с преувеличенным вертикальным масштабом

Косое пересечение
кулисной системы сбросов

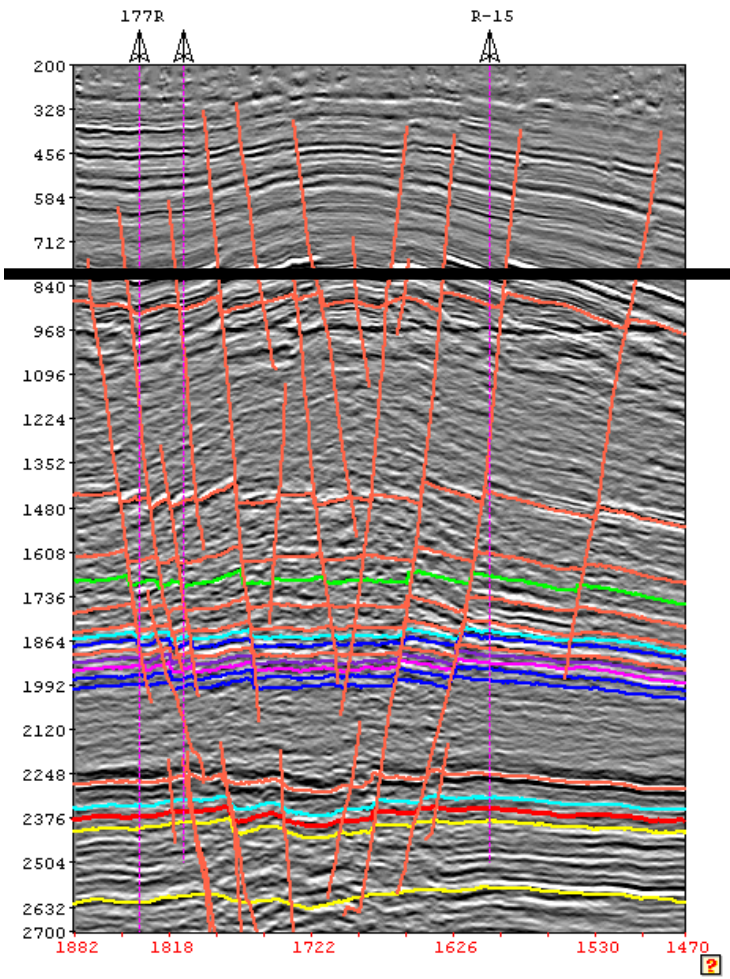

Параллельно
кулисной системе сбросов

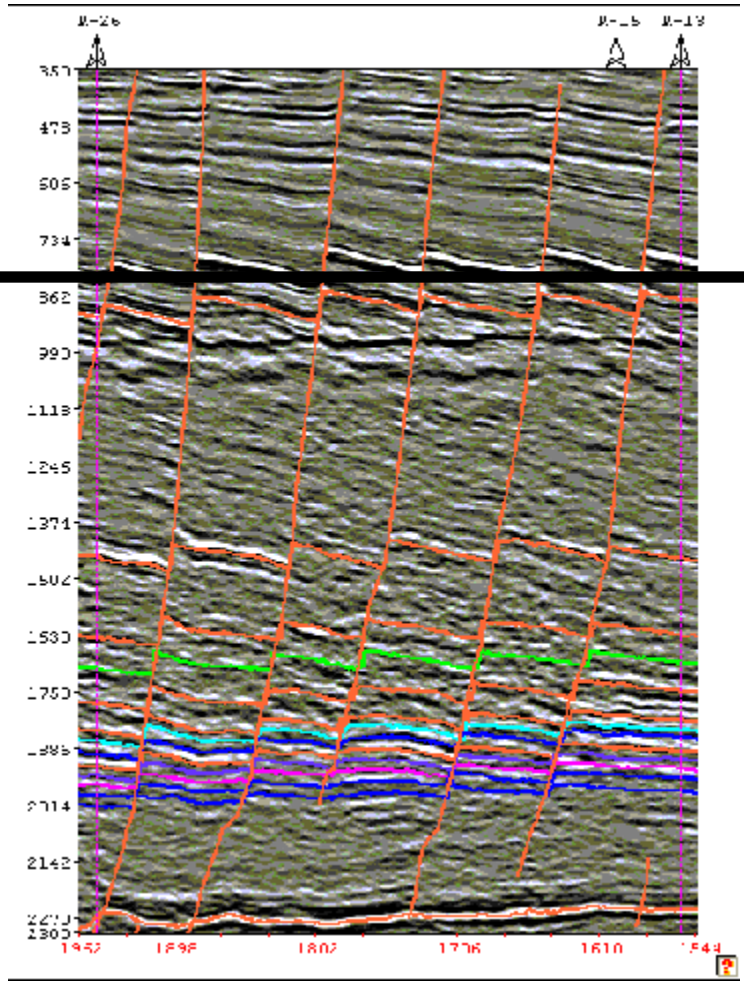

«Складчато-сбросовое зеркало» субгоризонтально
в разрезах разной ориентировки.

Антиклинали затухают вниз и вверх по разрезу.

Г.Н. Гогоненков, А.И. Тимурзиев и др, 2008, ЦГЭ

Сбросы и антиклинали, формирующиеся в зоне динамического влияния сдвигового разлома в фундаменте

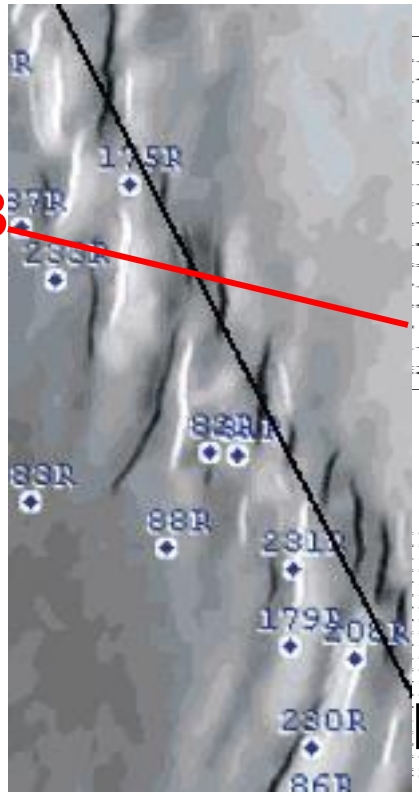

Карта углов наклона сбросов на уровне кровли юры

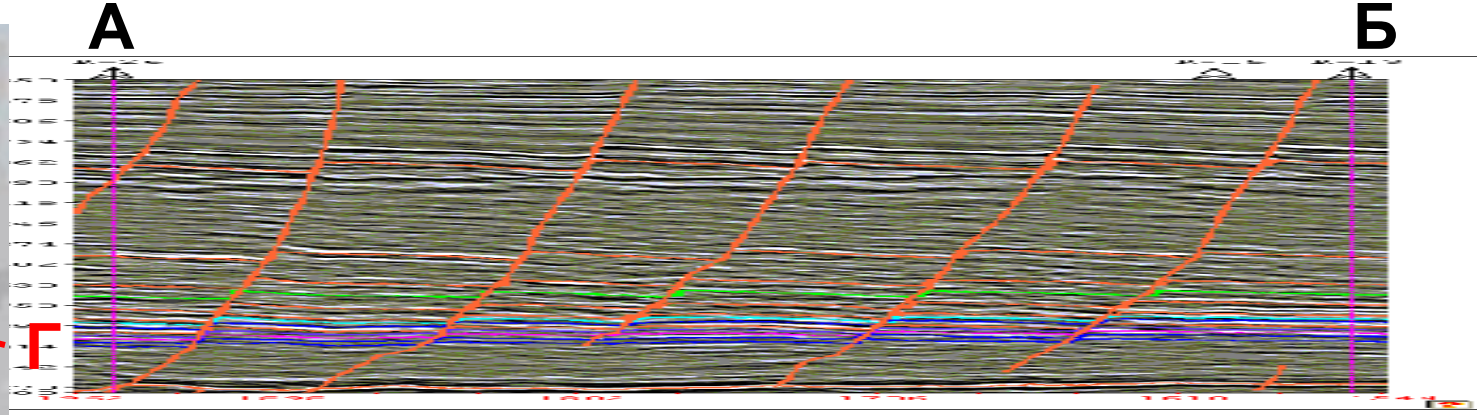

Разрез вдоль простирания сдвигового разлома

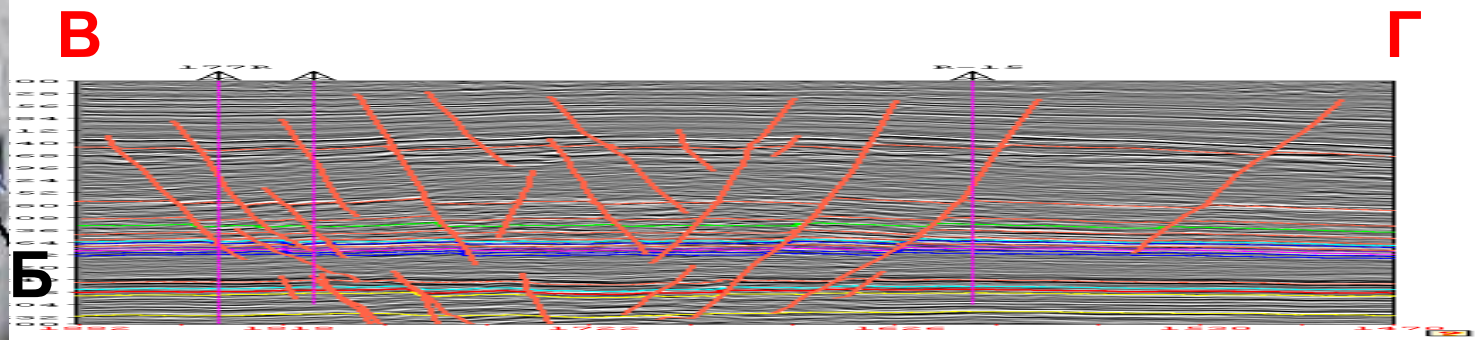

Разрез вкрест простирания

Очень малая амплитуда антиклиналей и смещений по сбросам в масштабе 1:1.

Г.Н. Гогоненков, А.И. Тимурзиев и др, 2008, ЦГЭ

Примеры сдвиговых дислокаций Пур-Тазовского региона

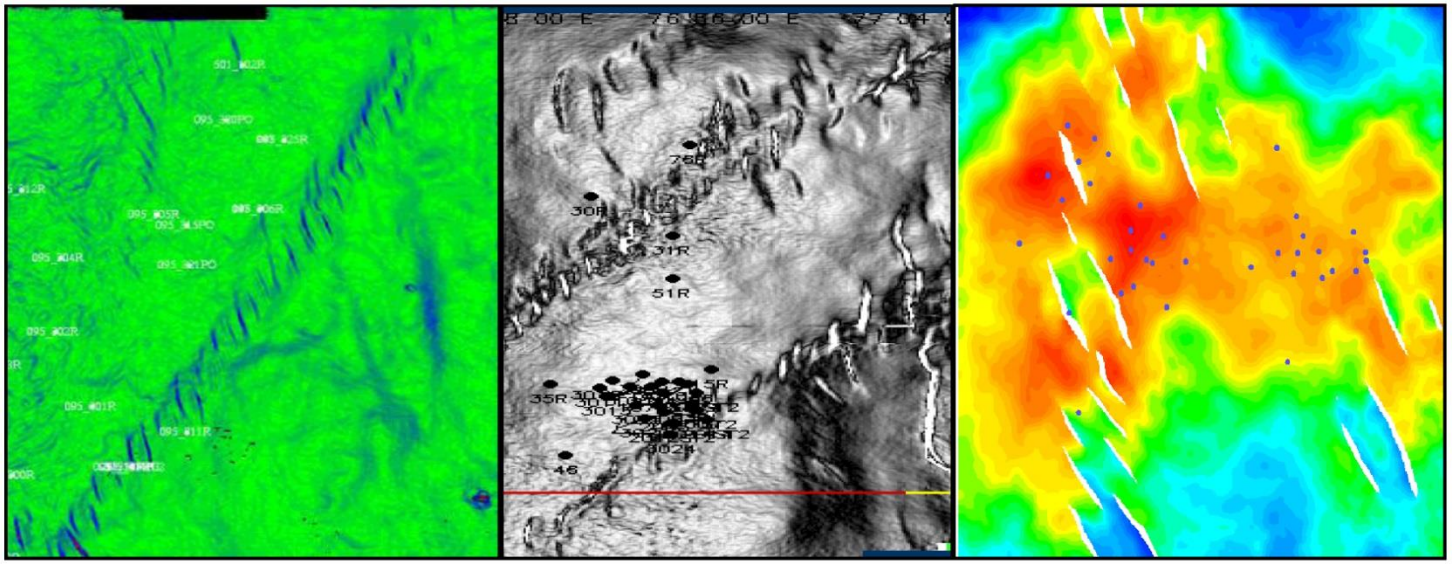

1 2 3

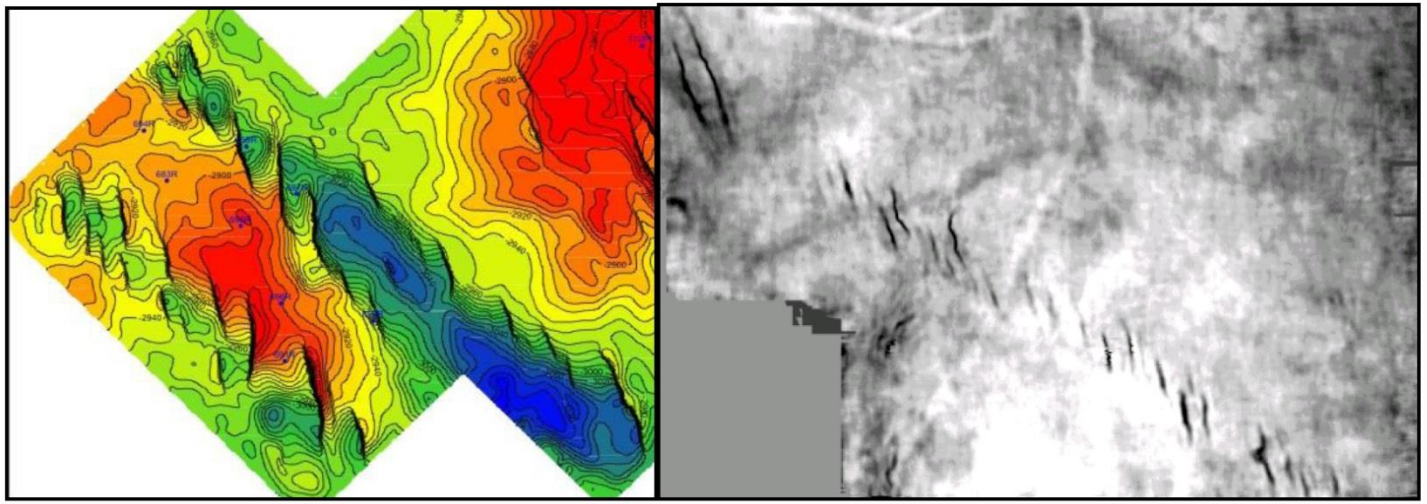

4 5

Ю.В. Филиппович, 2011, Газпромнефть

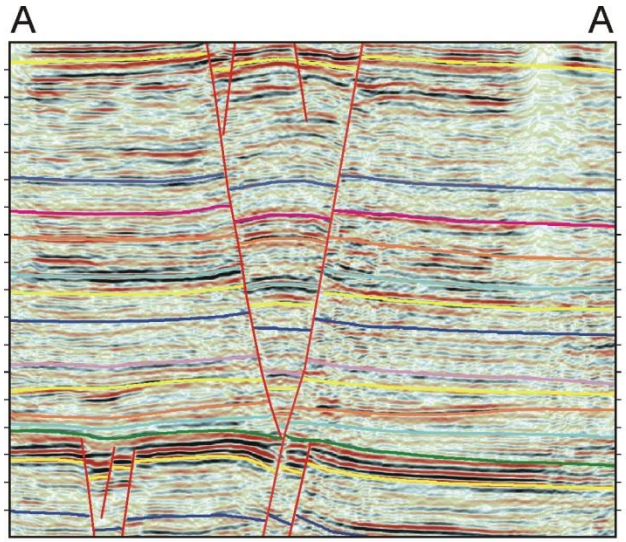

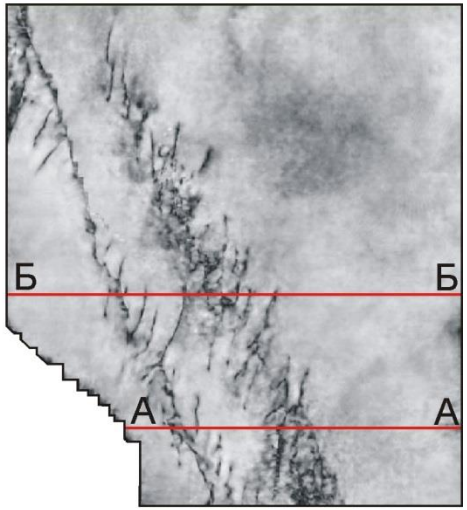

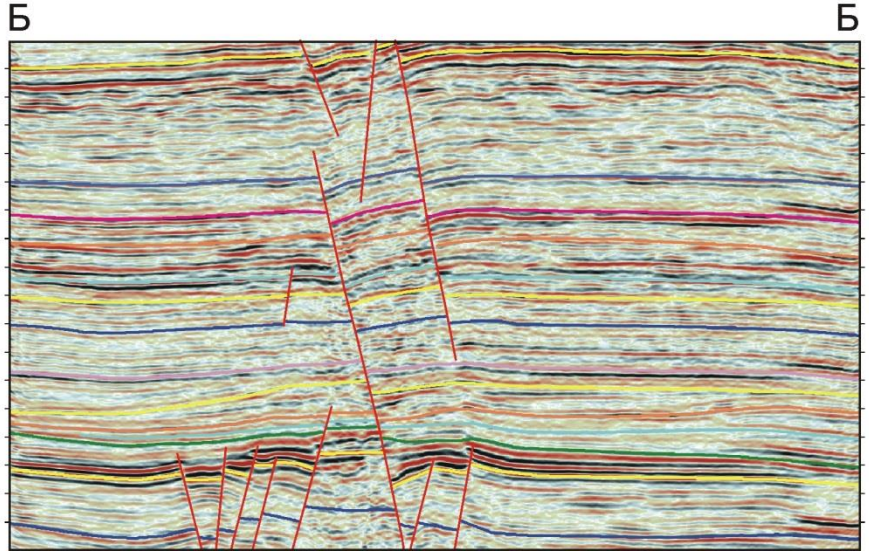

В. Жемчугова и др., 2010

Gupkin Field

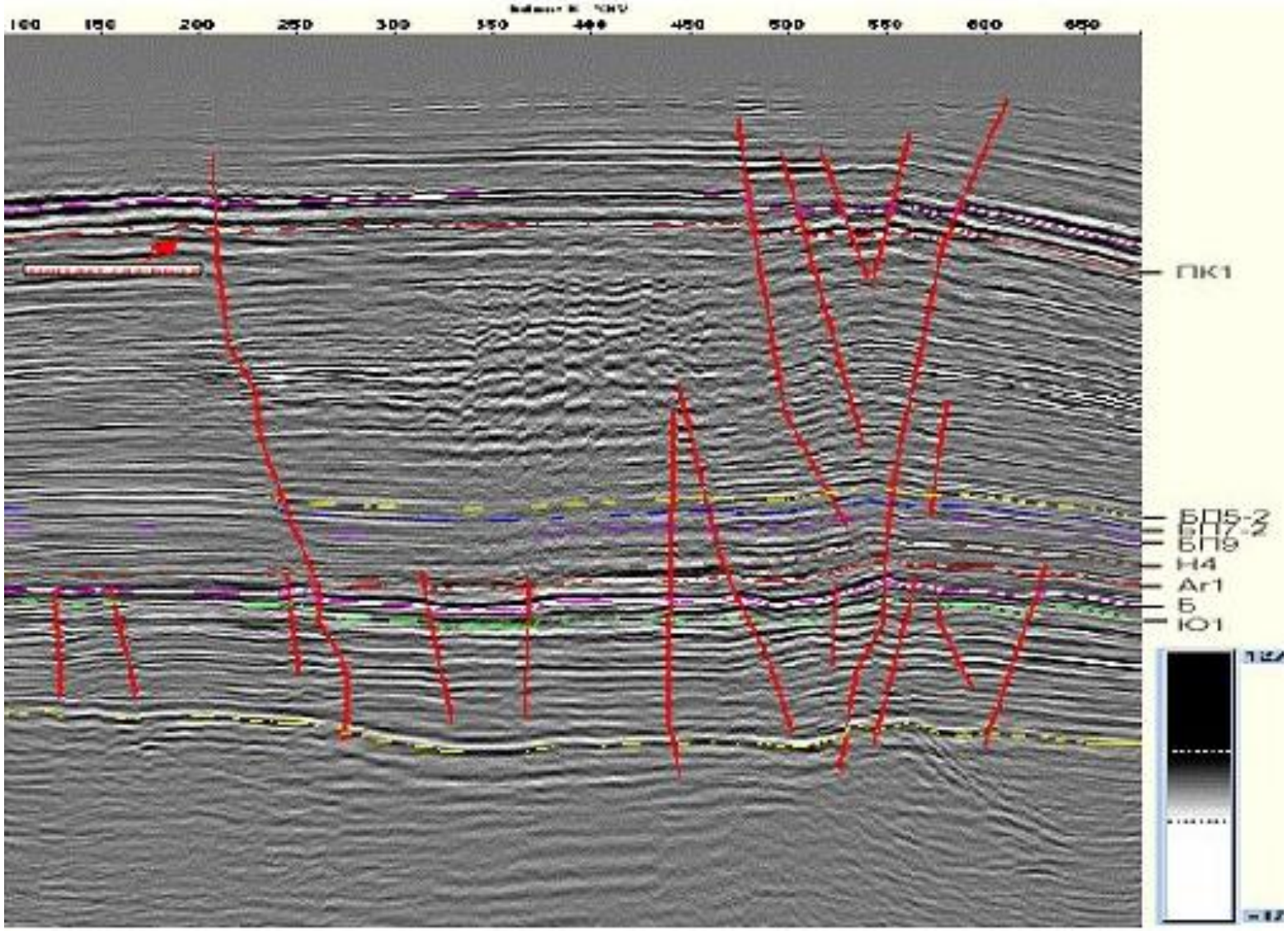

Gupkin Field

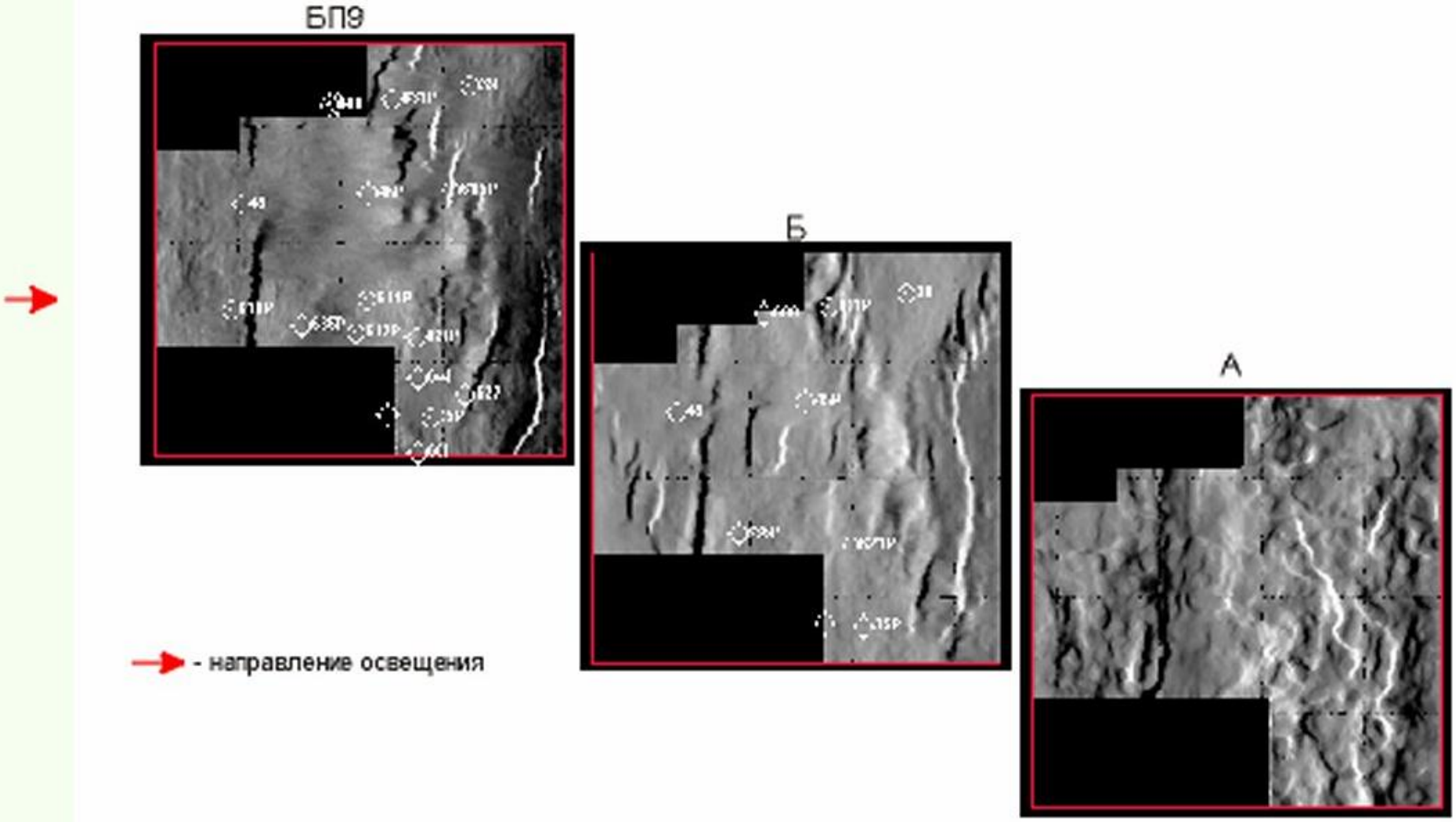

Komsomolsk Field

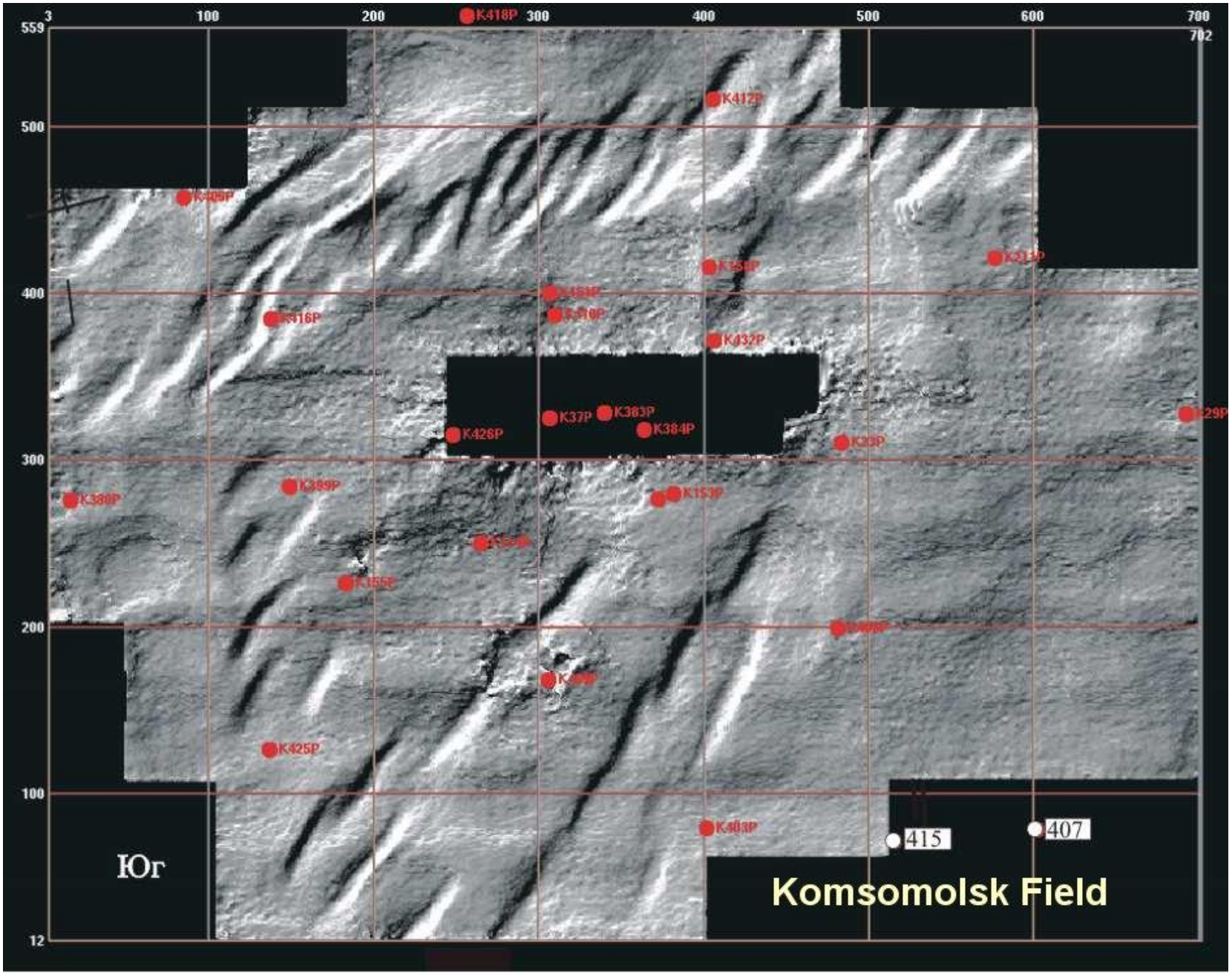

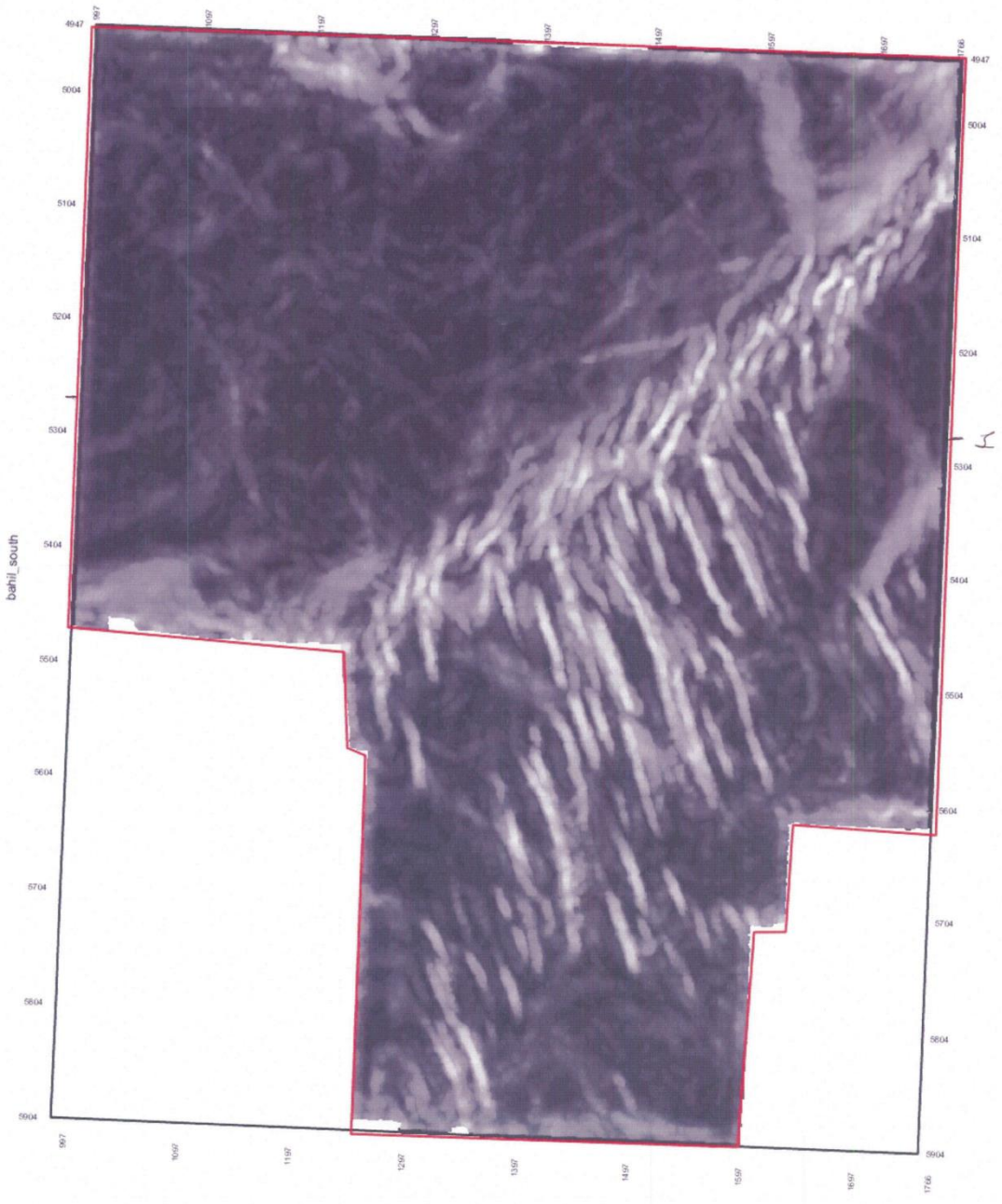
bahil_south
4947
5004
5104
5204
5304
5404
5504
5604
5704
5804
5904
997
1097
1197
1297
1397
1497
1597
1697
1766

Модель строения сдвиговой зоны в объеме (Никишин, Старцева, 2015)

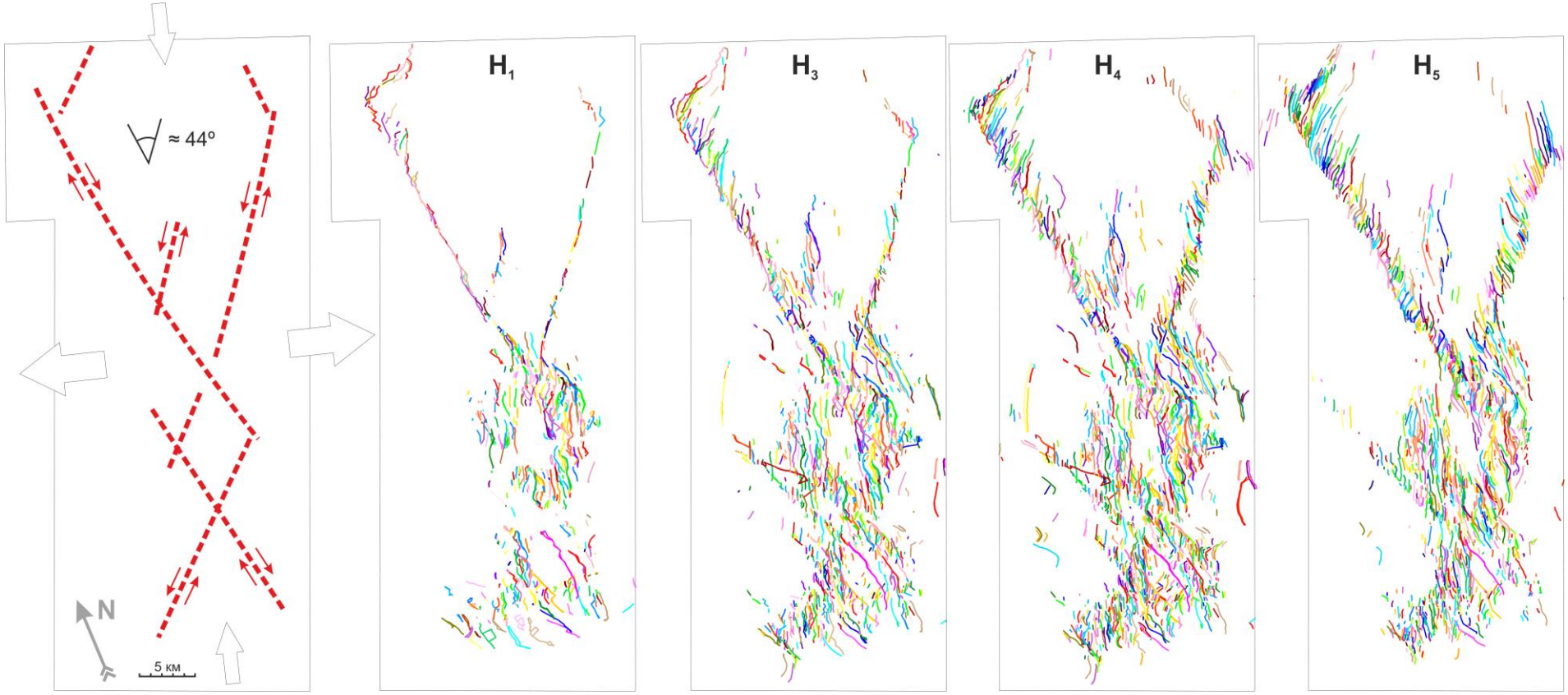

Геологическая интерпретация строения сдвиговых зон по анализу 3D сейсмических данных. Рисунок слева показывает гипотетическое расположение сдвиговых зон в условном фундаменте. Далее, рисунки показывают расположение разломов на разных стратиграфических уровнях снизу вверх над зонами сдвигов. H1-H5 – разные структурные поверхности.

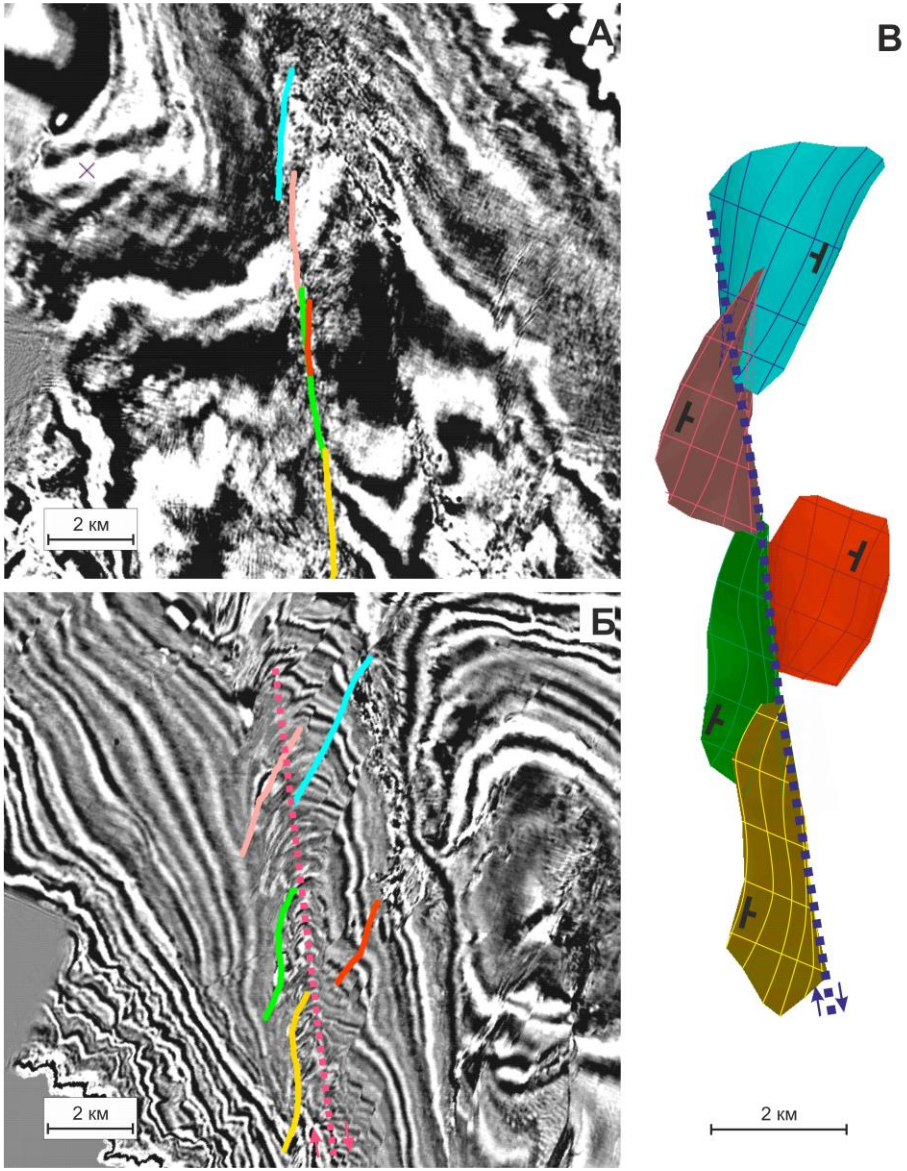

А – суброгизонтальный разрез (слайс) примерно в кровле условного фундамента; отдельные разломы выстраиваются в единую линию сдвиговой зоны. Б – субгоризонтальный разрез (слайс) в осадочном чехле над зоной сдвига. Отдельные единичные сдвиго-сбросы ориентированы диагонально относительно линии сдвига в фундаменте. В – графическая иллюстрация строения разломной зоны в объёме. Знаки показывают направление наклона сбросов.

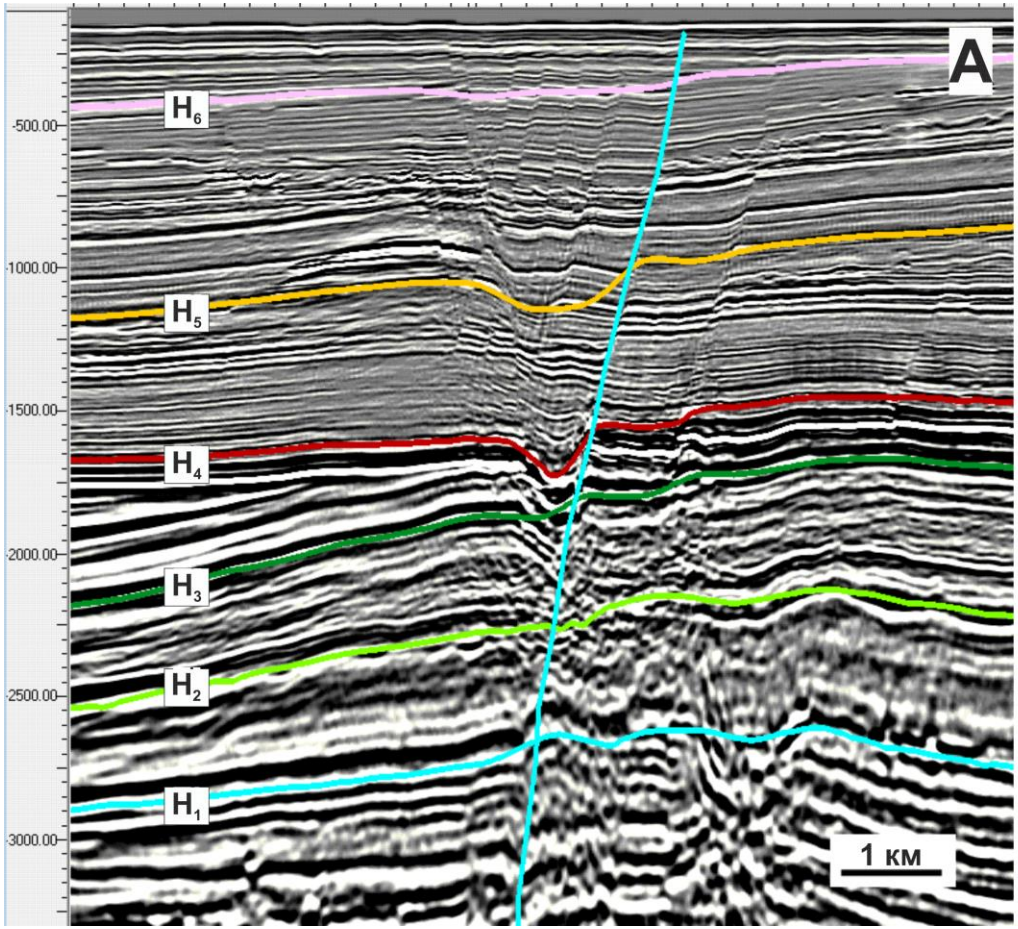

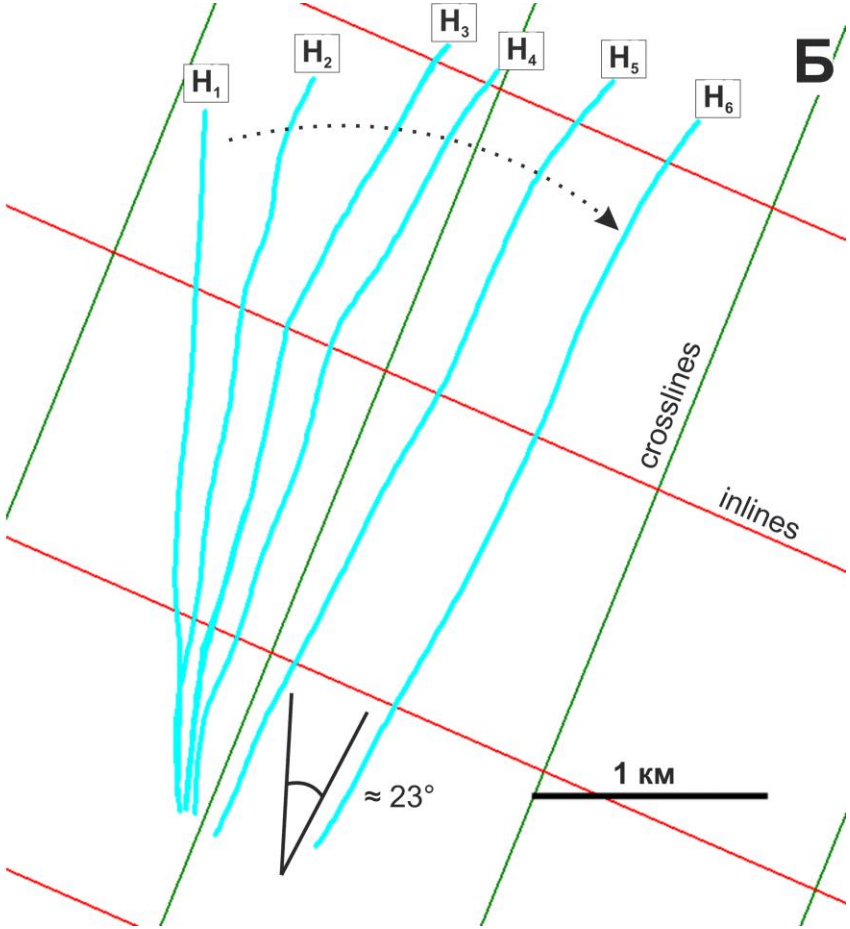

А – пример вида единичного сдвиго-сброса на 2D глубинном сейсмическом разрезе.
Б – изменение простирания единичного сдвиго-сброса по мере его продвижения вверх от нижней структурной поверхности H1 к верхней структурной поверхности H6. Видно плавное изменение простирание разлома на 23 градуса.

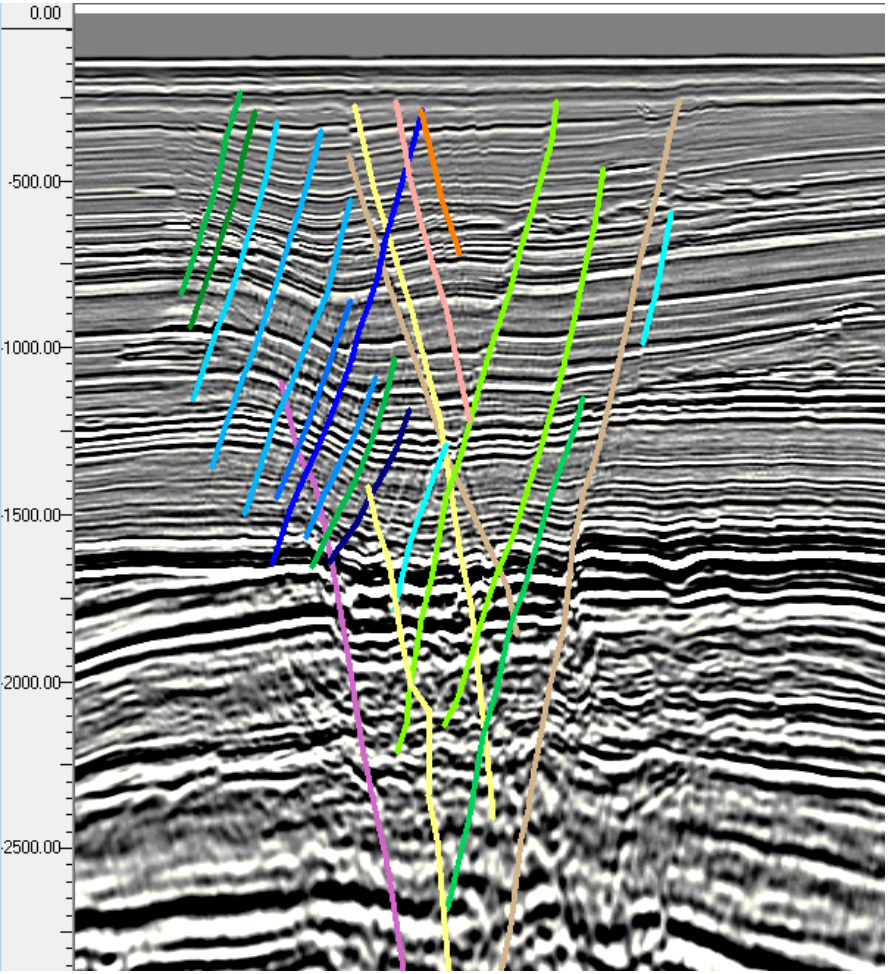

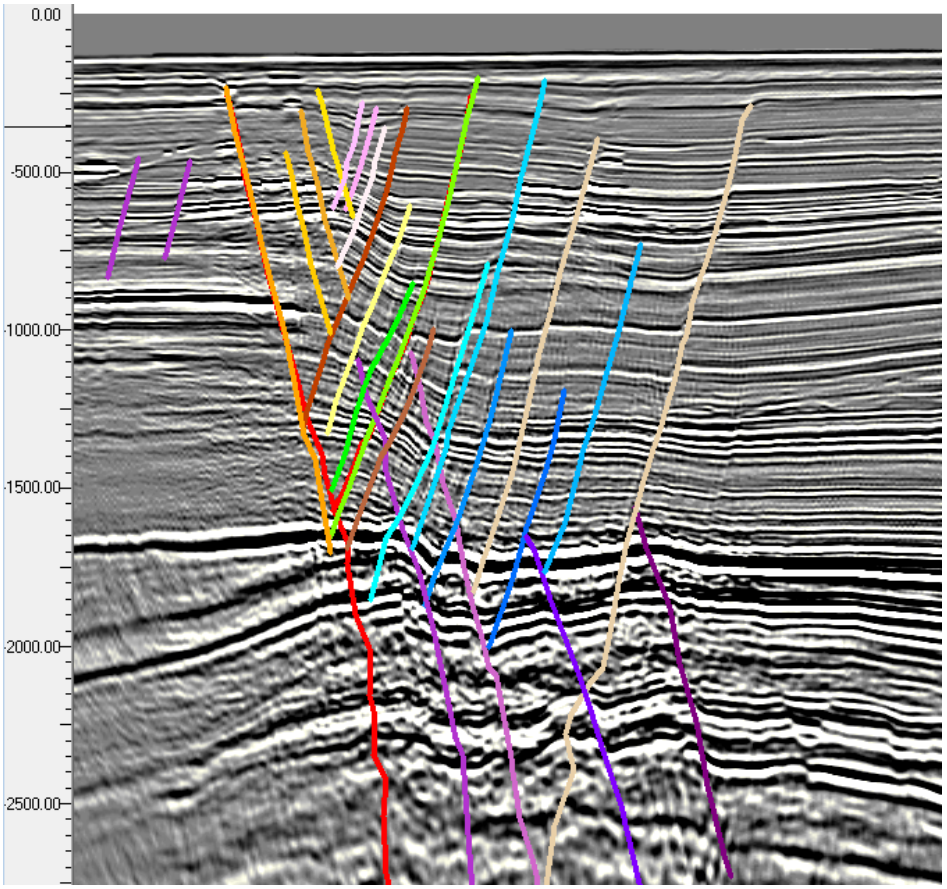

Вид единичных сбросов на 2D сейсмическом разрезе. С единичными сдвиго-сбросами связаны миниатюрные отрицательные цветковые структуры (зоны сдвиго-растяжения). Синтетические и антитетические сбросы относительно главных единичных сбросов являются оперяющими относительно последних

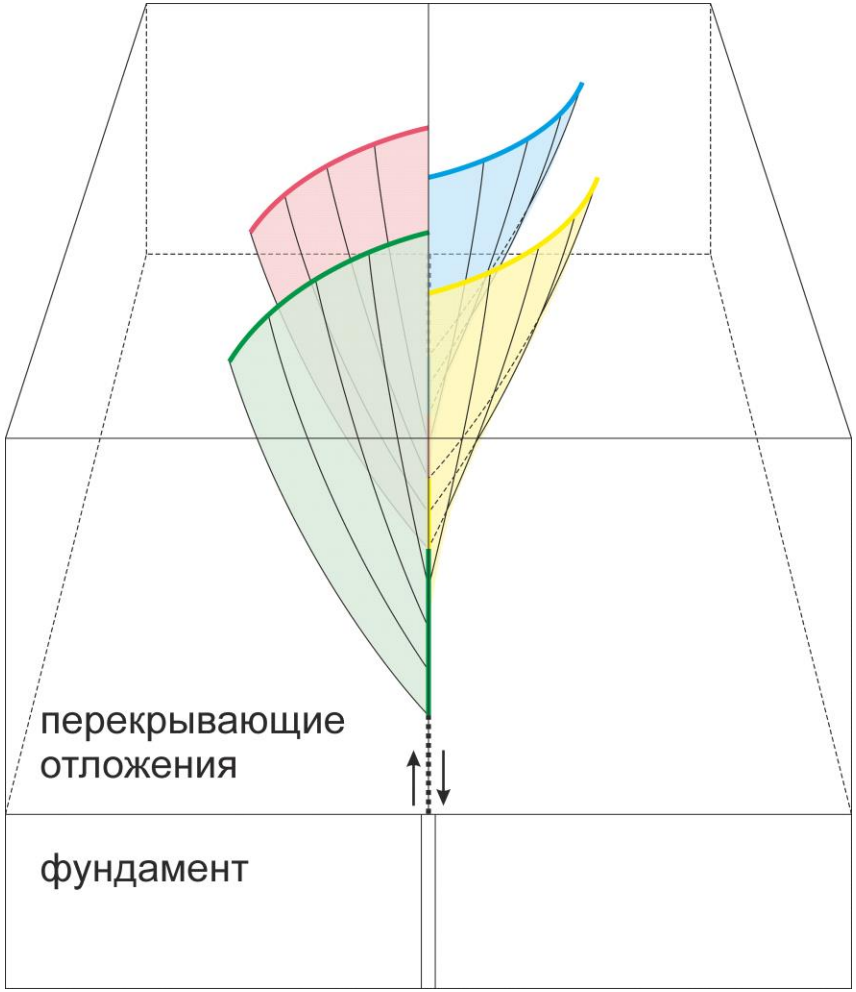

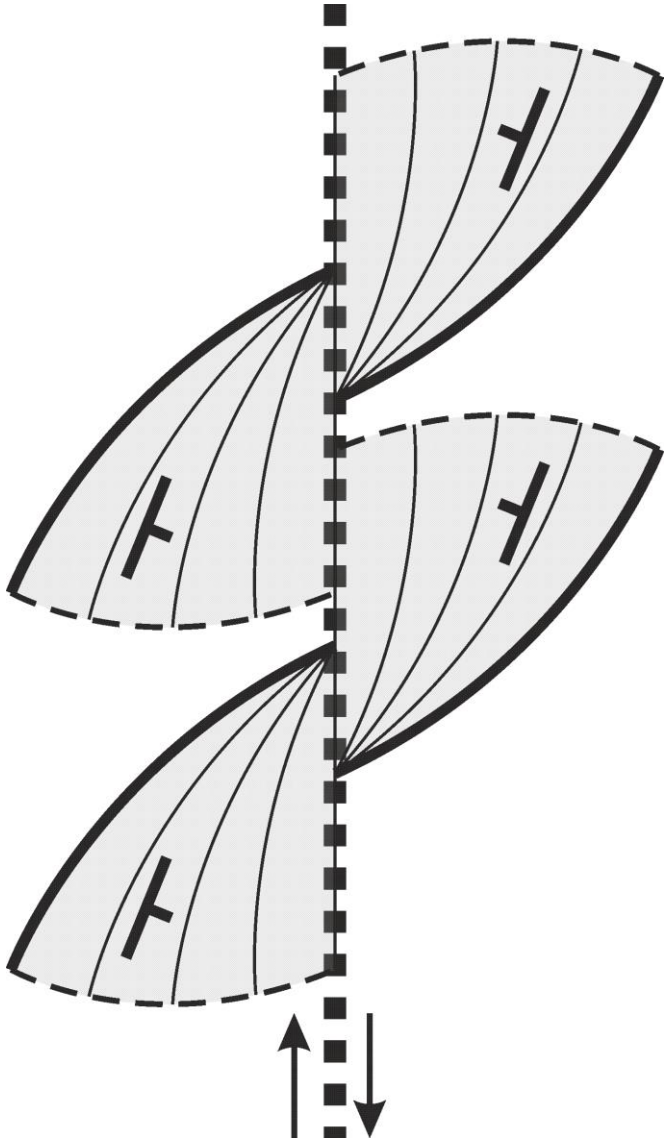

Модель соотношения сдвига в условном фундаменте и единичных сбросов в осадочном чехле.
А – вид в объеме, Б – вид сверху. Единичные сдвиго-сбросы образуют кулисные серии разломов по разную сторону сдвига, при этом кулисные серии сдвиго-сбросов по разную сторону сдвига наклонены в противоположные стороны. Плоскости единичных сдвиго-сбросов вверх меняют простирание с увеличением угла с зоной сдвига.

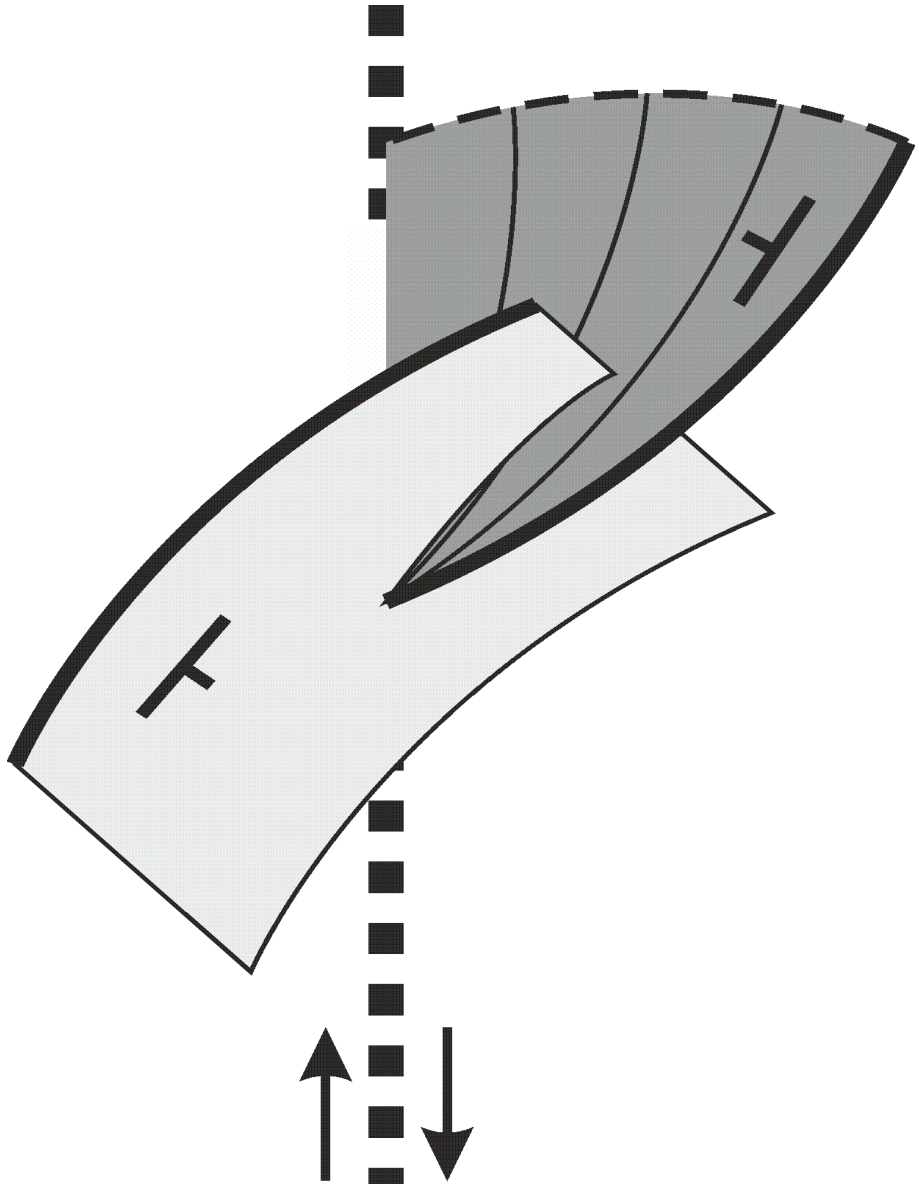

Модель строения единичного сдвиго-сброса и оперяющего его сброса меньшего ранга. Плоскость оперяющего сброса пересекает линию главного сдвига и наклонена в противоположную сторону наклона единичного сброса

Модель формирования новейших сдвиговых систем на площади ЛУ

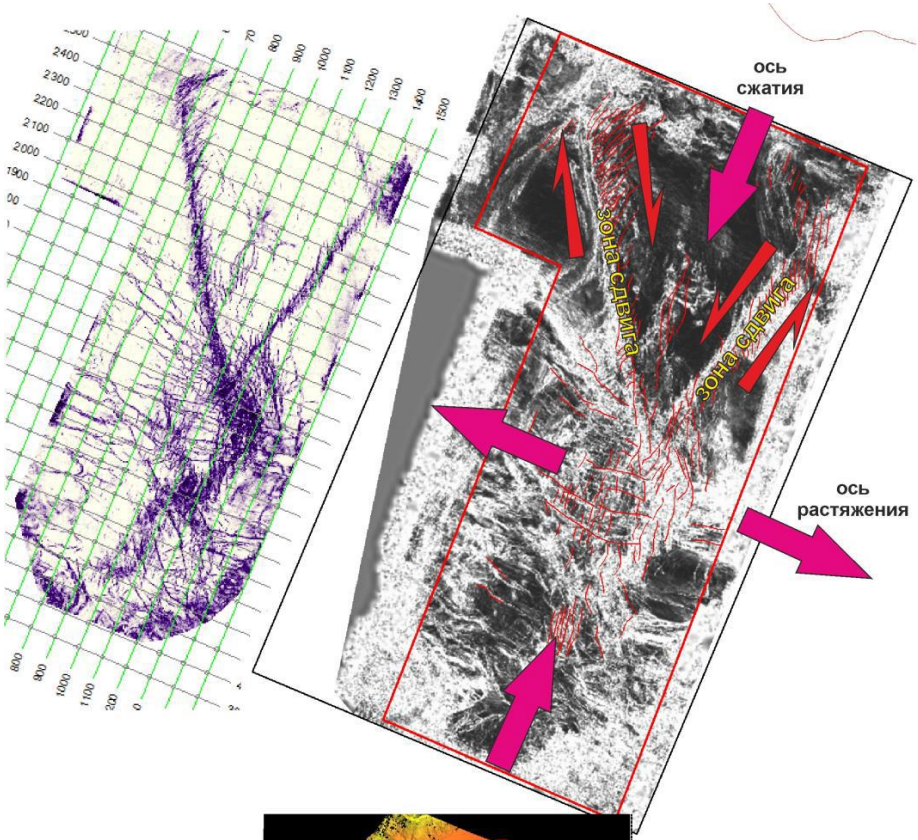

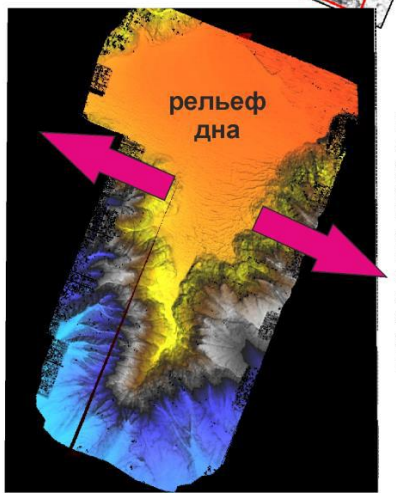

Понт-Четвертичное растяжение обусловлено гравитационным расползанием поднятия по слою солей синхронно со сжатием по оси ЮЗ-СВ

Сдвиговый разлом - Китай

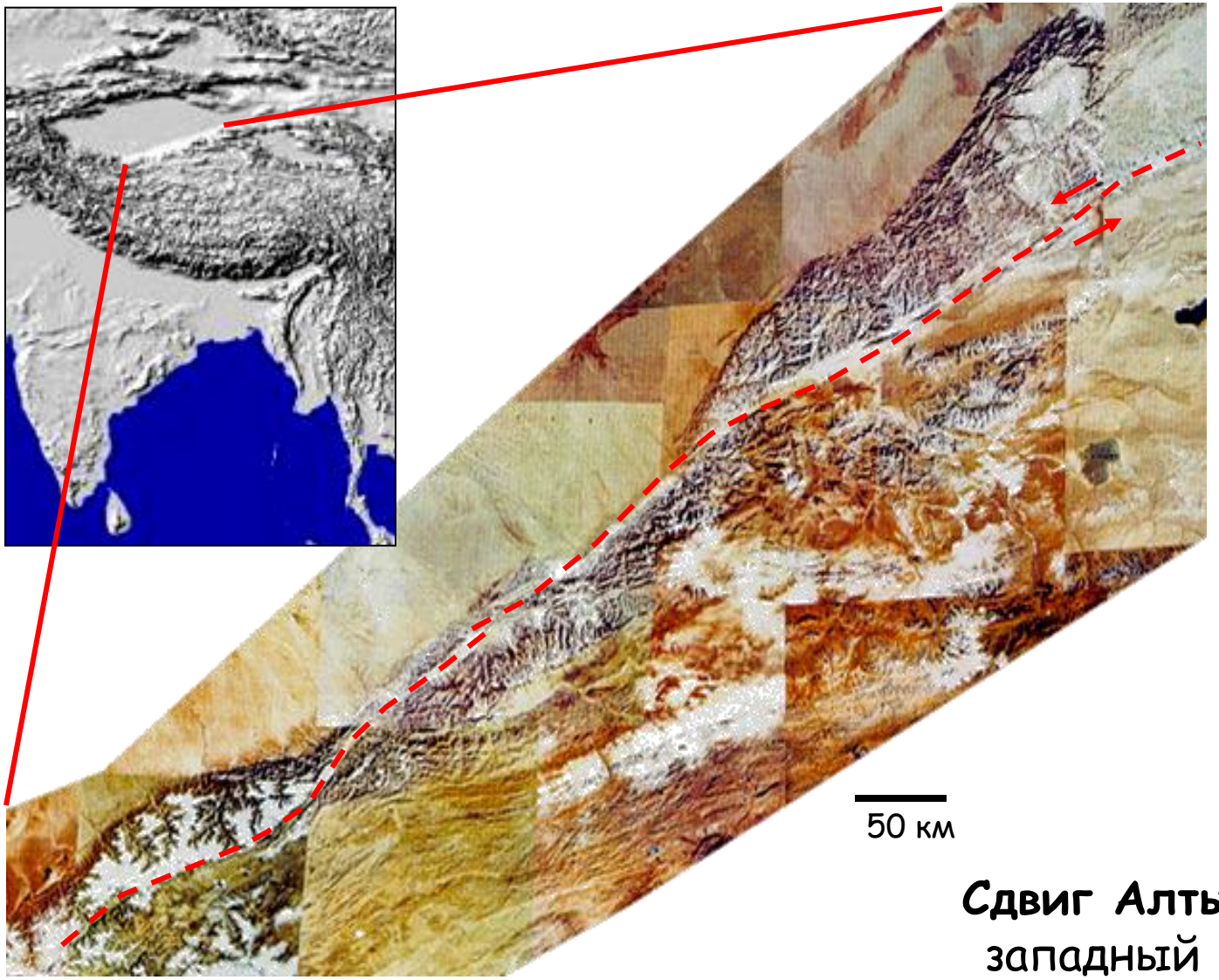

Сдвиг Алтынтаг,
западный Китай

Позитивный профиль в виде цветка

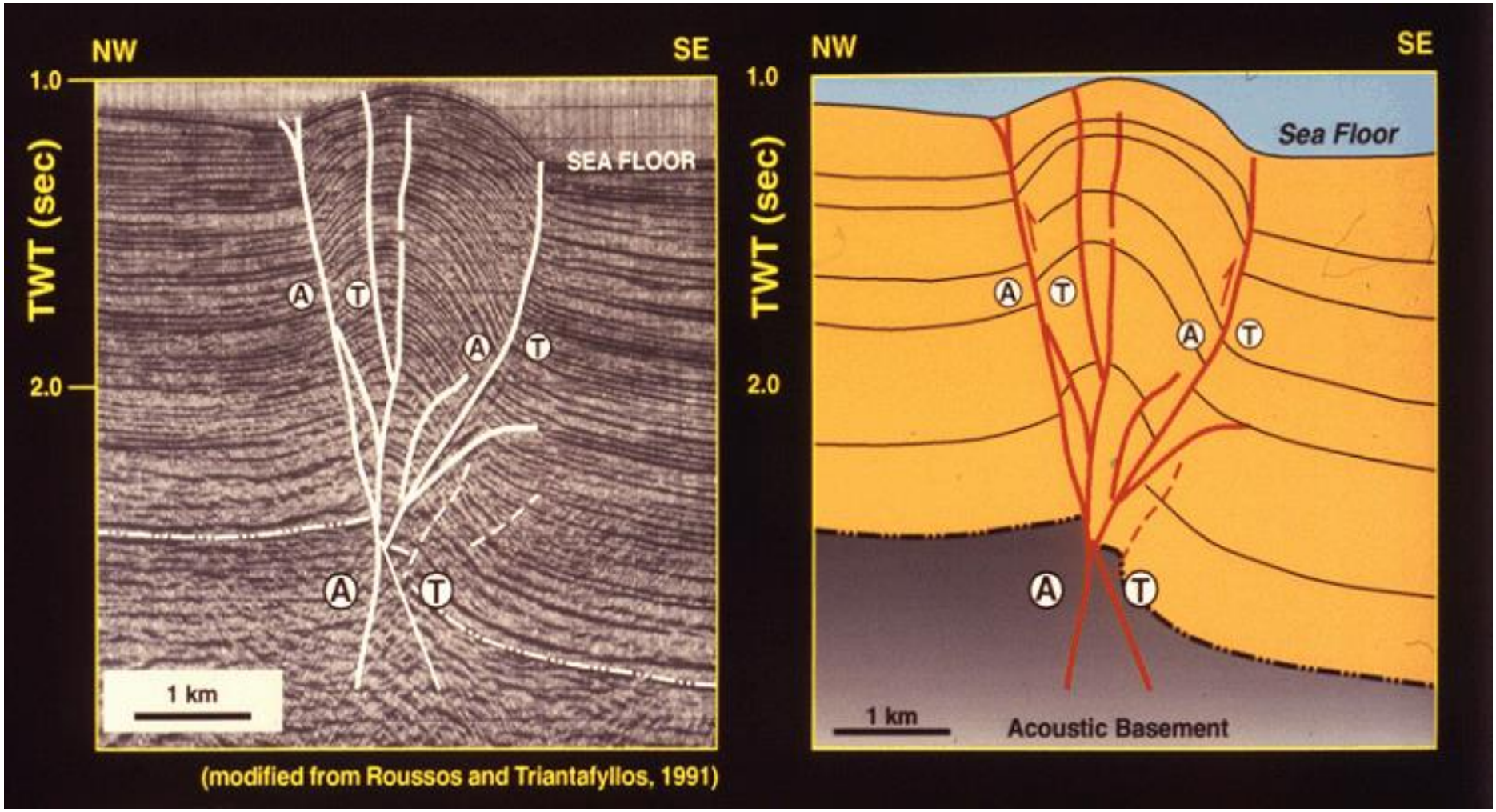

Позитивный профиль в виде цветка в сейсмическом и геологическом разрезе, зона сбросов Атос

Характеристики и обозначения на карте

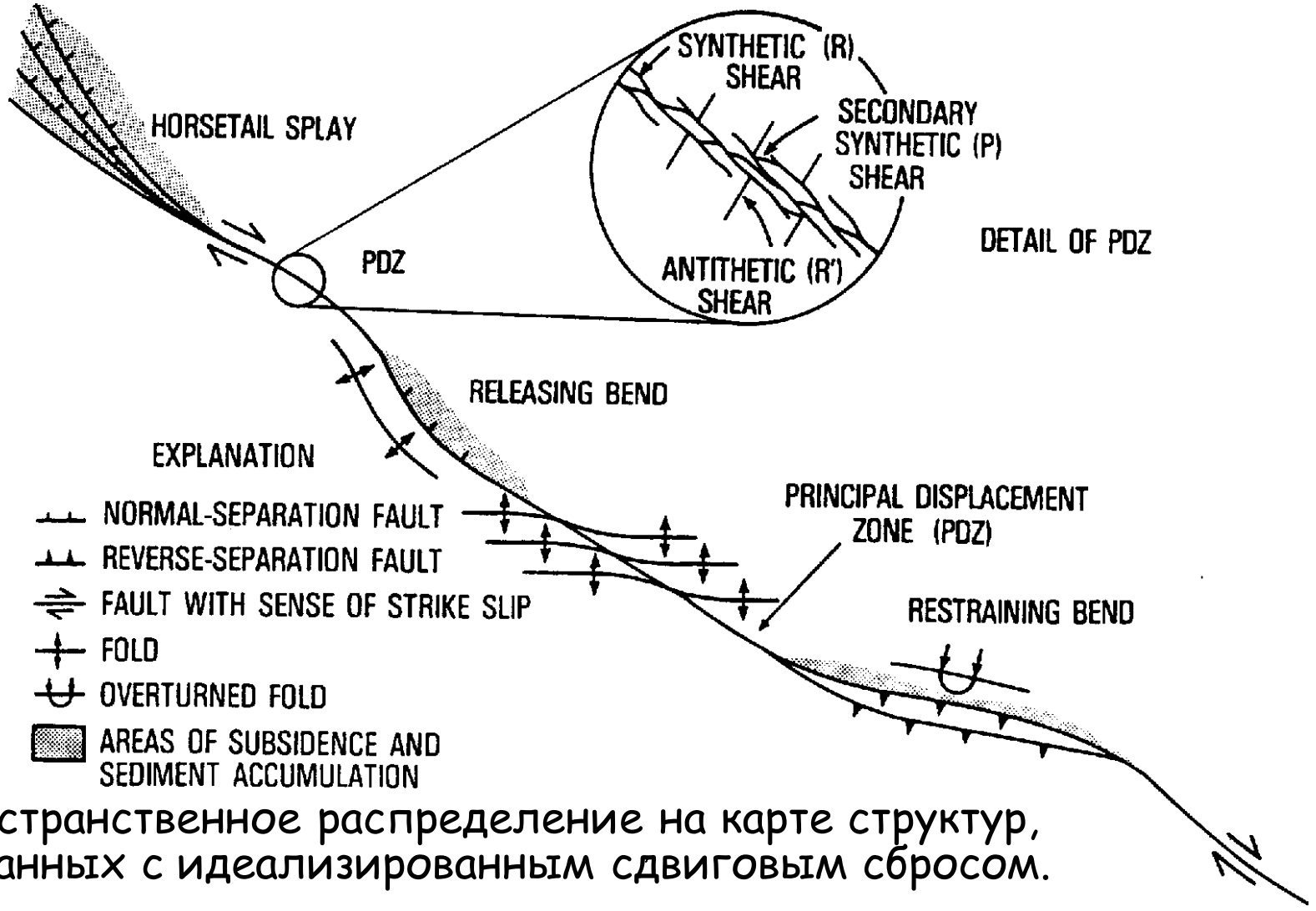

Пространственное распределение на карте структур, связанных с идеализированным сдвиговым сбросом.

Ограничивающие ступени

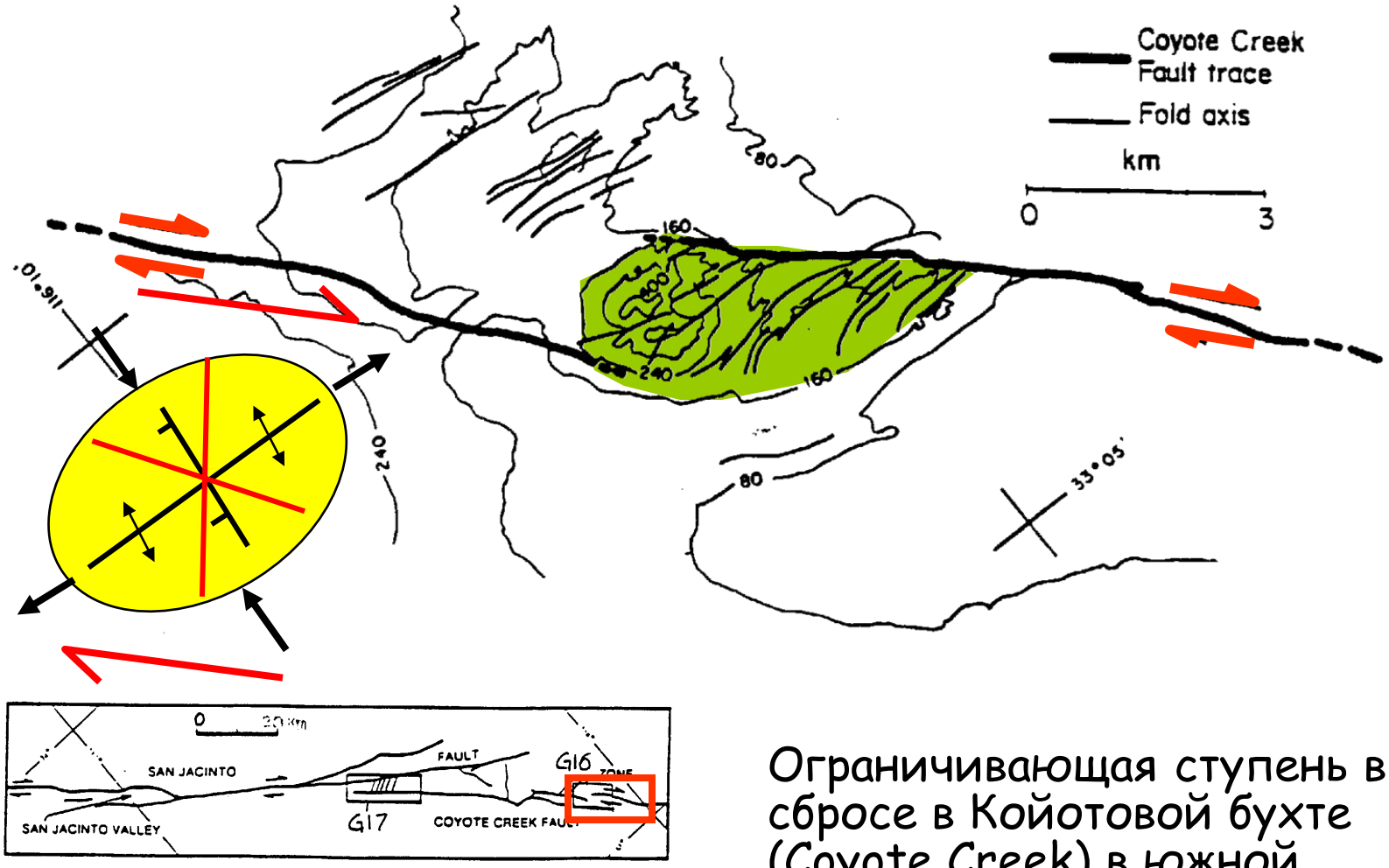

Ограничивающая ступень в сбросе в Койотовой бухте (Coyote Creek) в южной Калифорнии.

Ограничивающие изгибы – месторождение R.E.B., Алжир

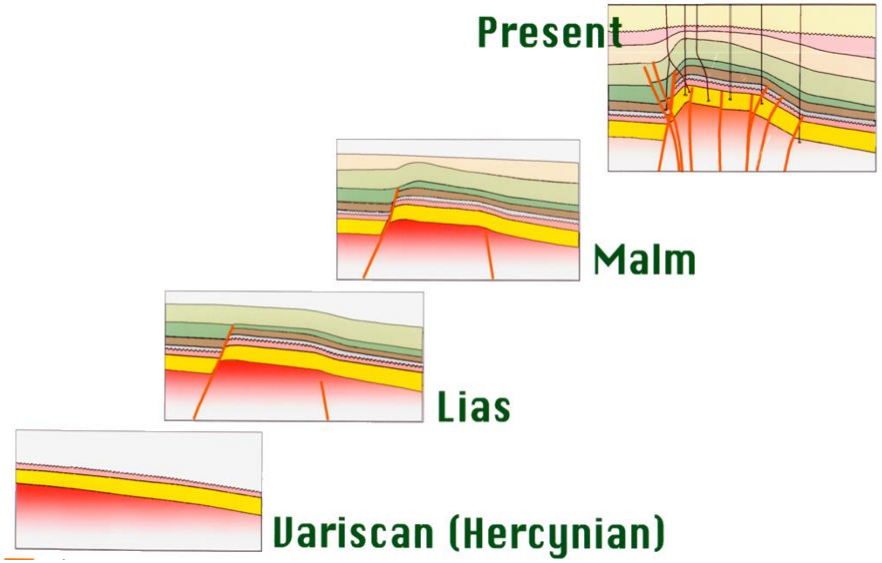

- Восстановление разреза, иллюстрирующего 3 основные стадии деформации
  - –Образование обыкновенных сбросов на ранней стадии.
  - –Верхнеюрский диапиризм
  - –Австрийская (средний меловой период) транпрессия

- Очевиден транспрессиональный характер структуры Rhourde El Baguel.
  - –Структурный выгиб, представленный месторождением, образован главным образом вследствие сдвигового смещения вправо в области ограничивающего изгиба вдоль сброса, несогласного или почти согласного с простиранием пород.

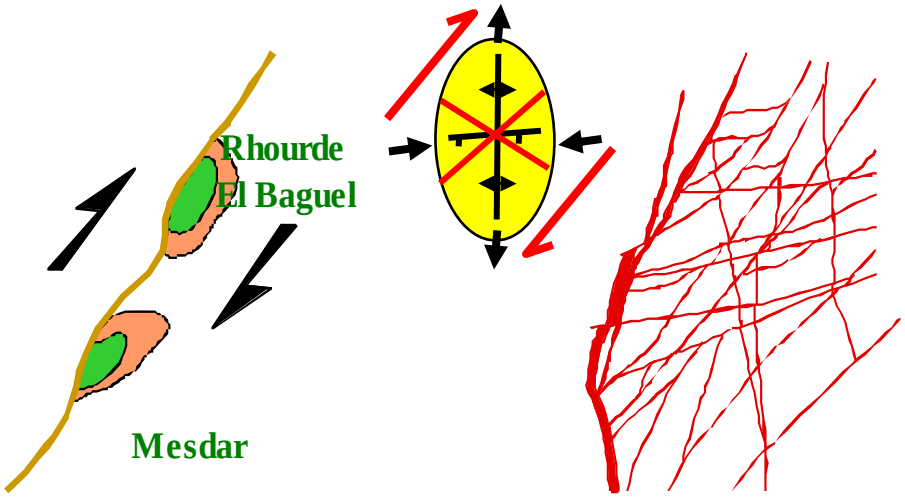

Ушаковская транспрессионная структура, Южно-Чукотский бассейн

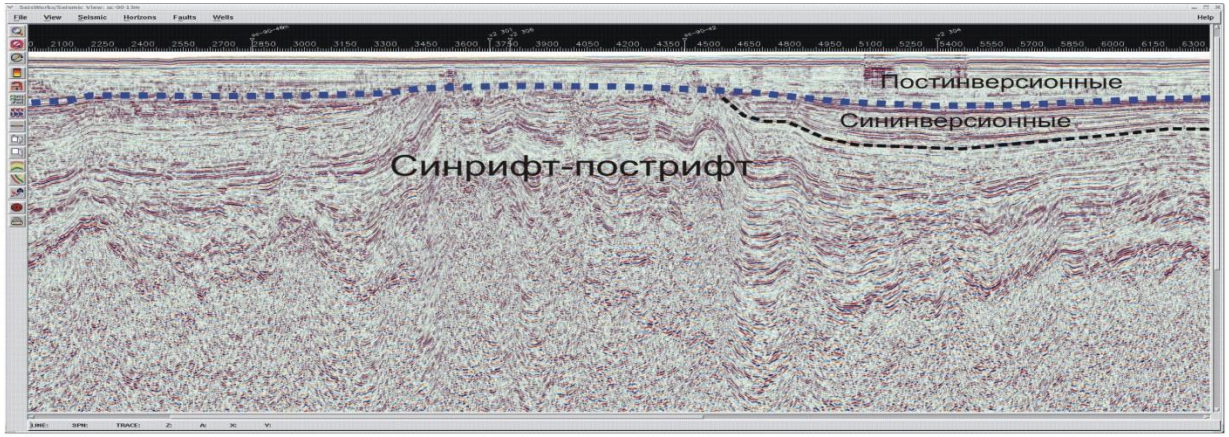

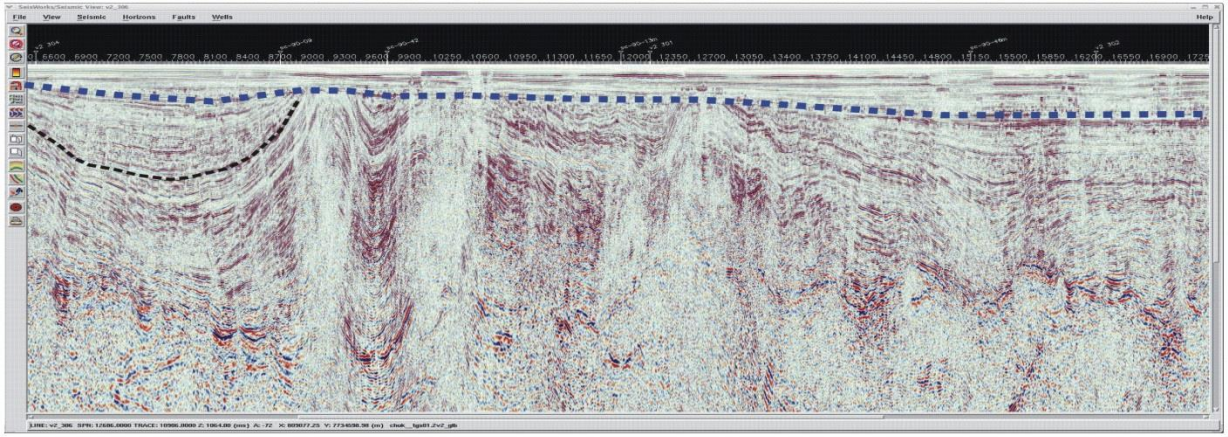

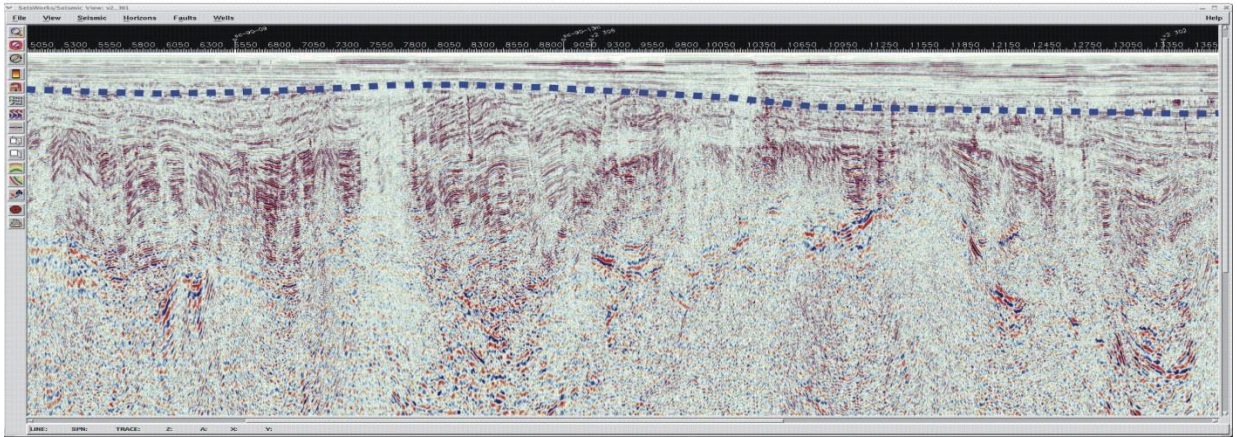

(Ихсанов, Роснефть, 2009)

Structural geometry and evolution of releasing and restraining bends: Insights from laser-scanned experimental models

Shankar Mitra and Debapriya Paul

AAPG Bulletin, v. 95, no. 7 (July 2011), pp. 1147–1180

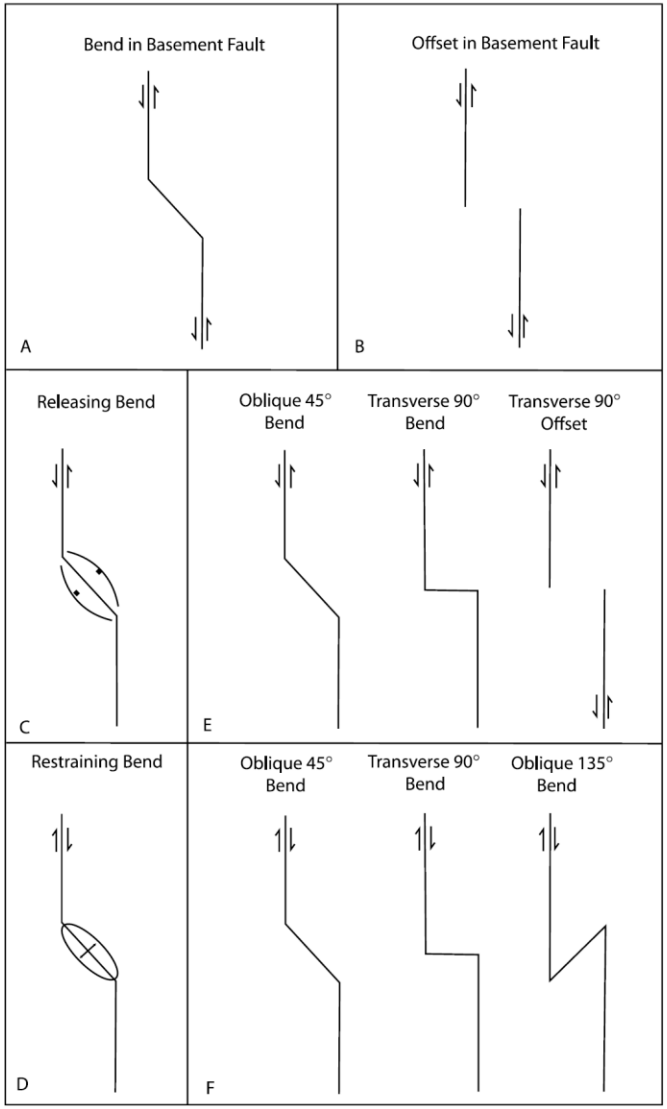

Figure 1. (A, B) Possible basement fault configurations for strike-slip faults. (A) Bend. (B) Offset. (C) Releasing bend. (D) Restraining bend. (E) Initial basement fault configurations used in experiments for releasing bends and offsets. (F) Initial basement fault configurations used in experiments for restraining bends. Figures 2 and 13 show details of the experimental setup for (E) and (F).

is modeled with stiff clay, which is significantly more rigid than the overlying soft clay representing the sedimentary cover, but which allows for a small component of deformation of the basement, especially in the immediate vicinity of the major faults. Sliding metal plates, which underlie the basement, are used only to control the nature of deformation and the position of the bend or offset. Preexisting vertical cuts in the stiff clay define the initial geometry of the basement faults. This configuration also enables us to study the difference between releasing offsets and bends, which result

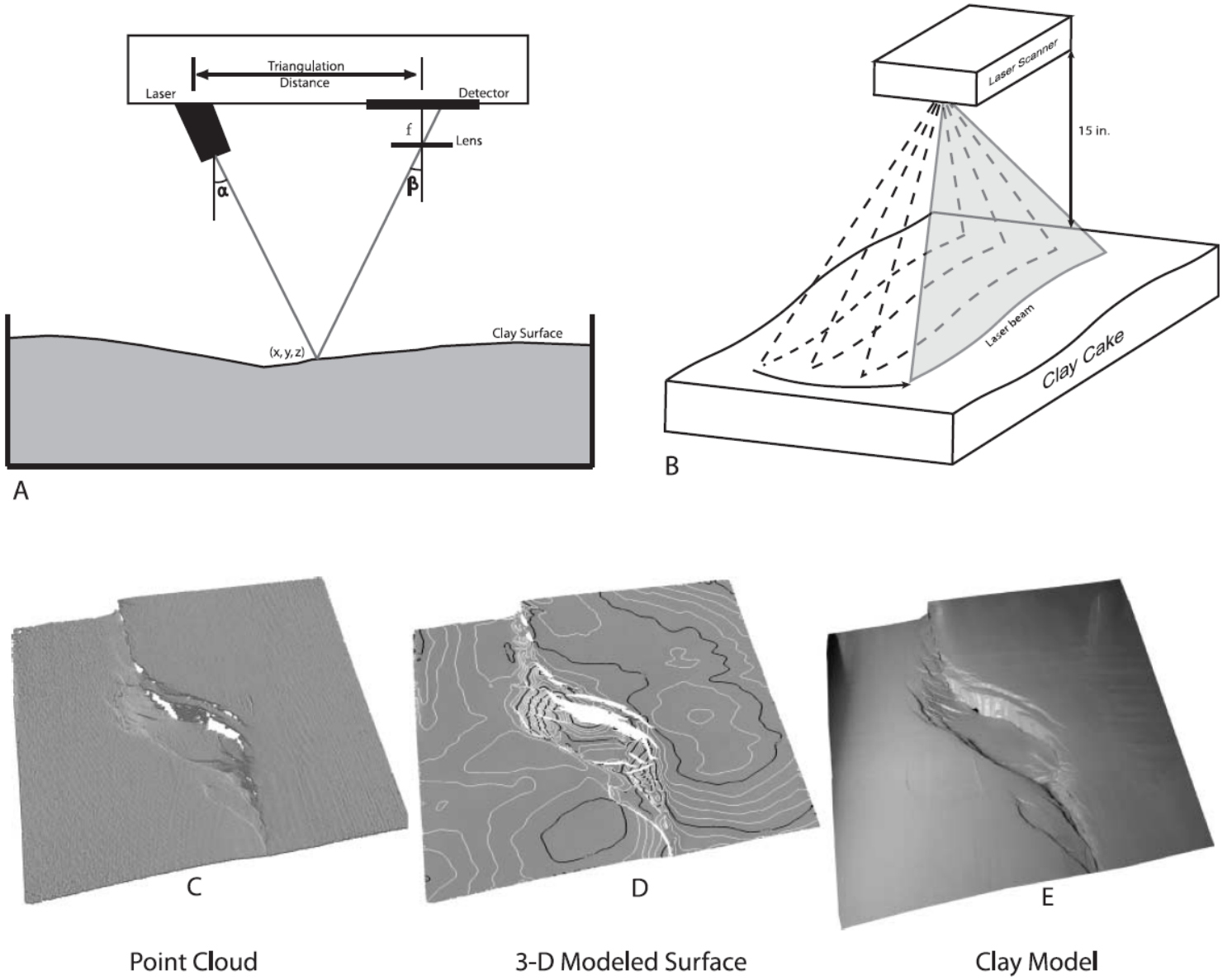

Figure 3. Laser scanning of experimental clay models. (A) Schematic diagram of the working principle of the laser scanner with the triangulation formed by the laser source, the detector, and the point on the clay surface from which the laser beam is reflected. (B) Schematic view of the laser scanner projecting a line and sweeping across the clay surface at a constant velocity (from Bose and Mitra, 2010; used with permission from AAPG). (C) Cloud of points obtained from the scanned surface and visualized in GO-CAD. (D) Modeled surface in GO-CAD cut by faults. (E) Oblique photograph of the top of the clay surface.

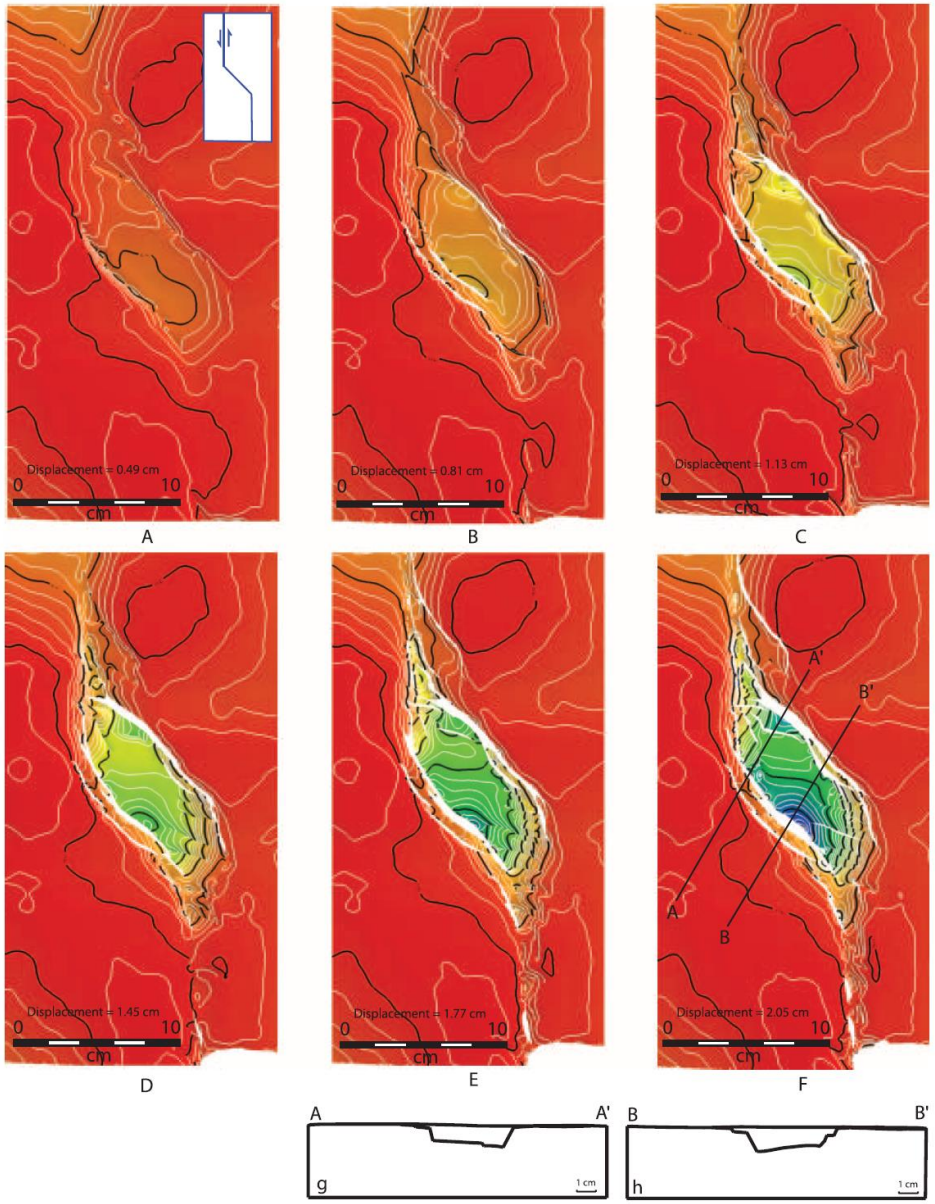

Figure 5. Three-dimensional geometry of the top of the sedimentary cover for a releasing bend with an oblique (45°) bend connecting two strike-slip fault segments in the basement. Panels A–F show the progressive evolution of the structure with increasing strike-slip displacement. Contours in this and subsequent diagrams are in intervals of 0.4 mm. Every fifth contour is shown in black. Color grids reflect structural elevation with red and yellow representing high areas and blue and green representing low areas. Note the formation of two diametrically opposite lows in the pull-apart basin. (G, H) Cross sections through top of clay showing final basin geometry and shift in polarity for cross sections AA′ and BB′. Locations of the cross sections are shown in (F).

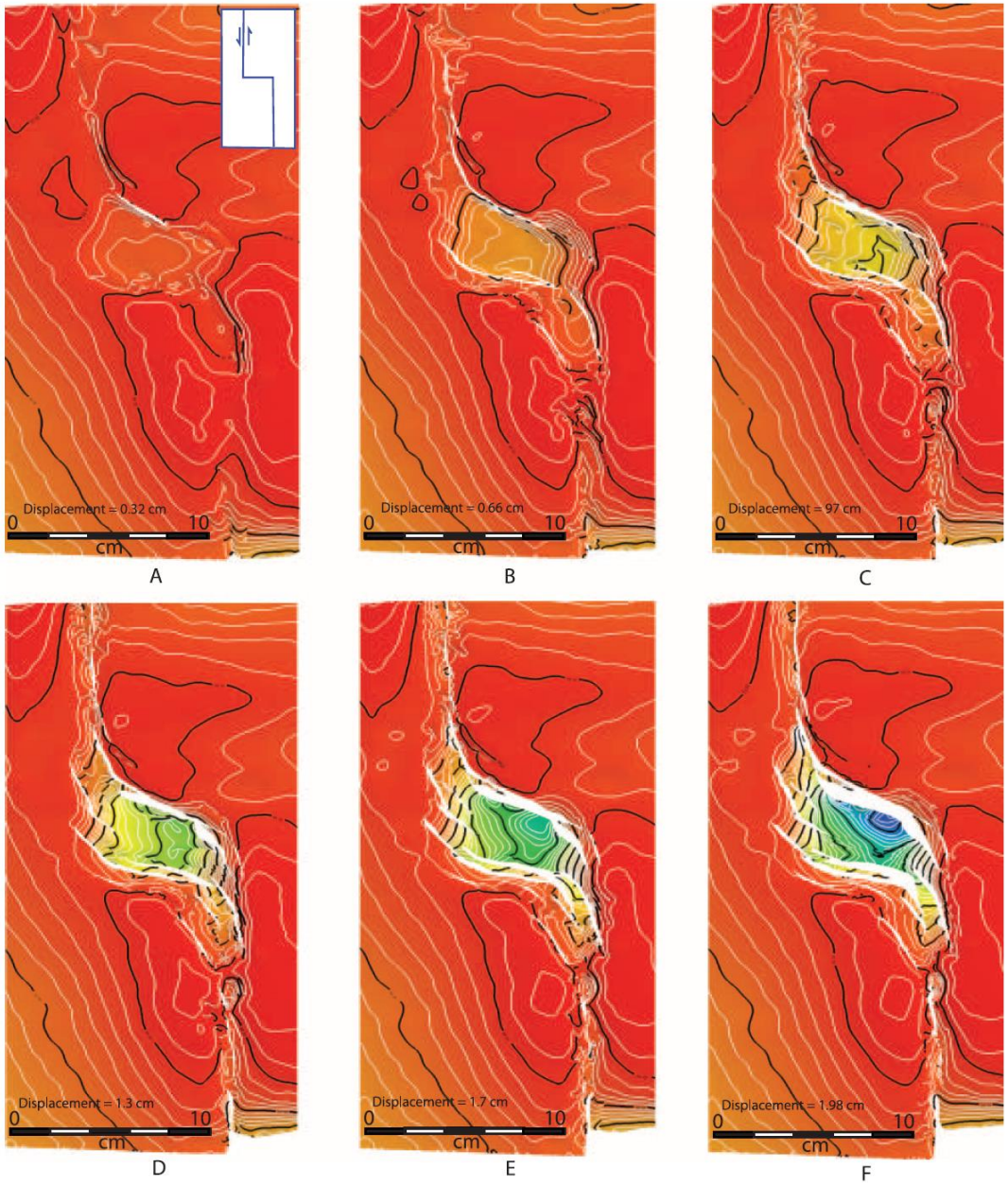

Figure 7. Three-dimensional geometry of the top of the sedimentary cover for a releasing bend with a transverse (90°) bend connecting two strike-slip fault segments in the basement. Panels A–F show the progressive evolution of the structure with increasing strike-slip displacement.

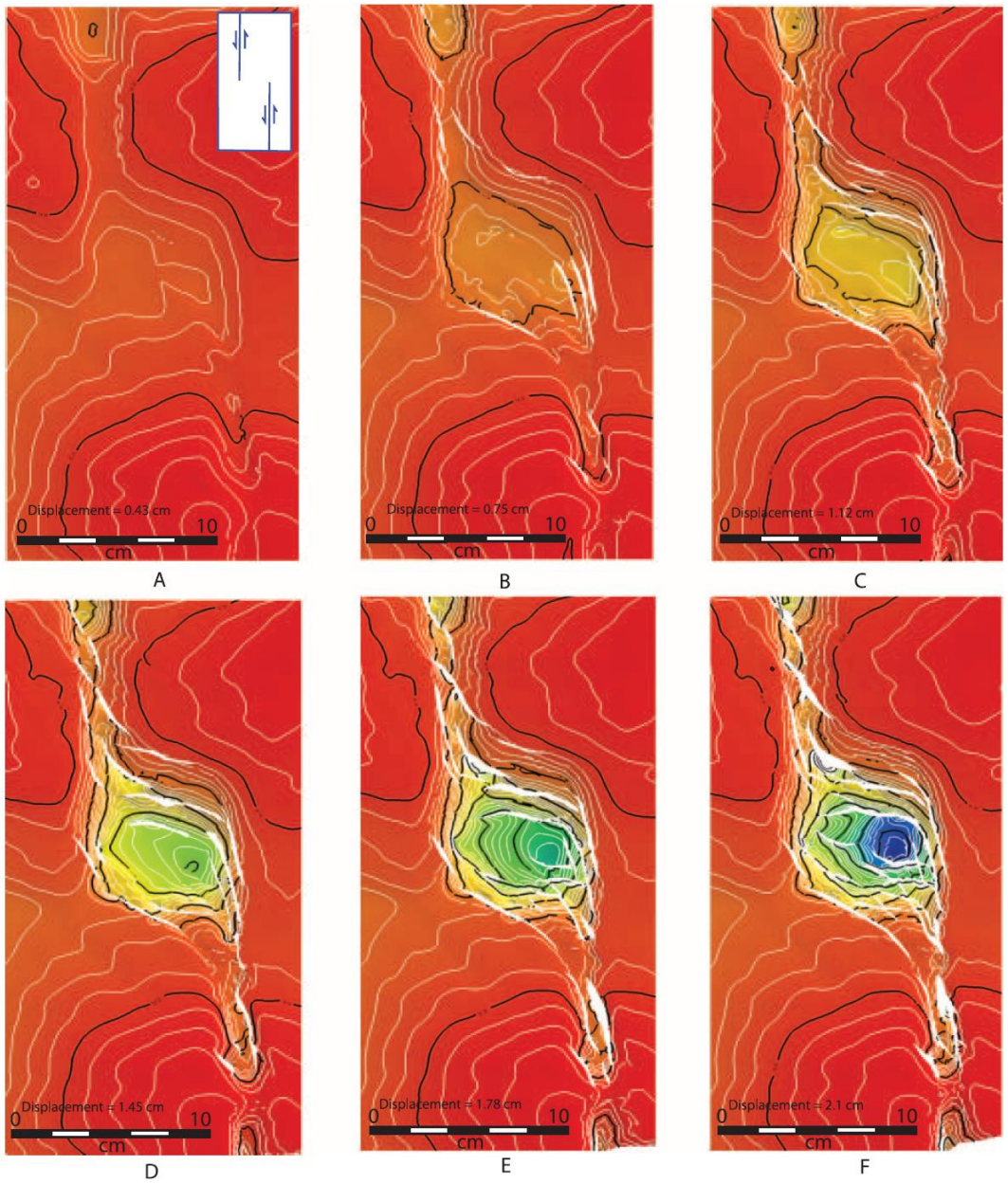

Figure 9. Three-dimensional geometry of the top of the sedimentary cover for a releasing offset with a transverse (90°) offset between two strike-slip fault segments in the basement. Panels A–F show the progressive evolution of the structure with increasing strike-slip displacement.

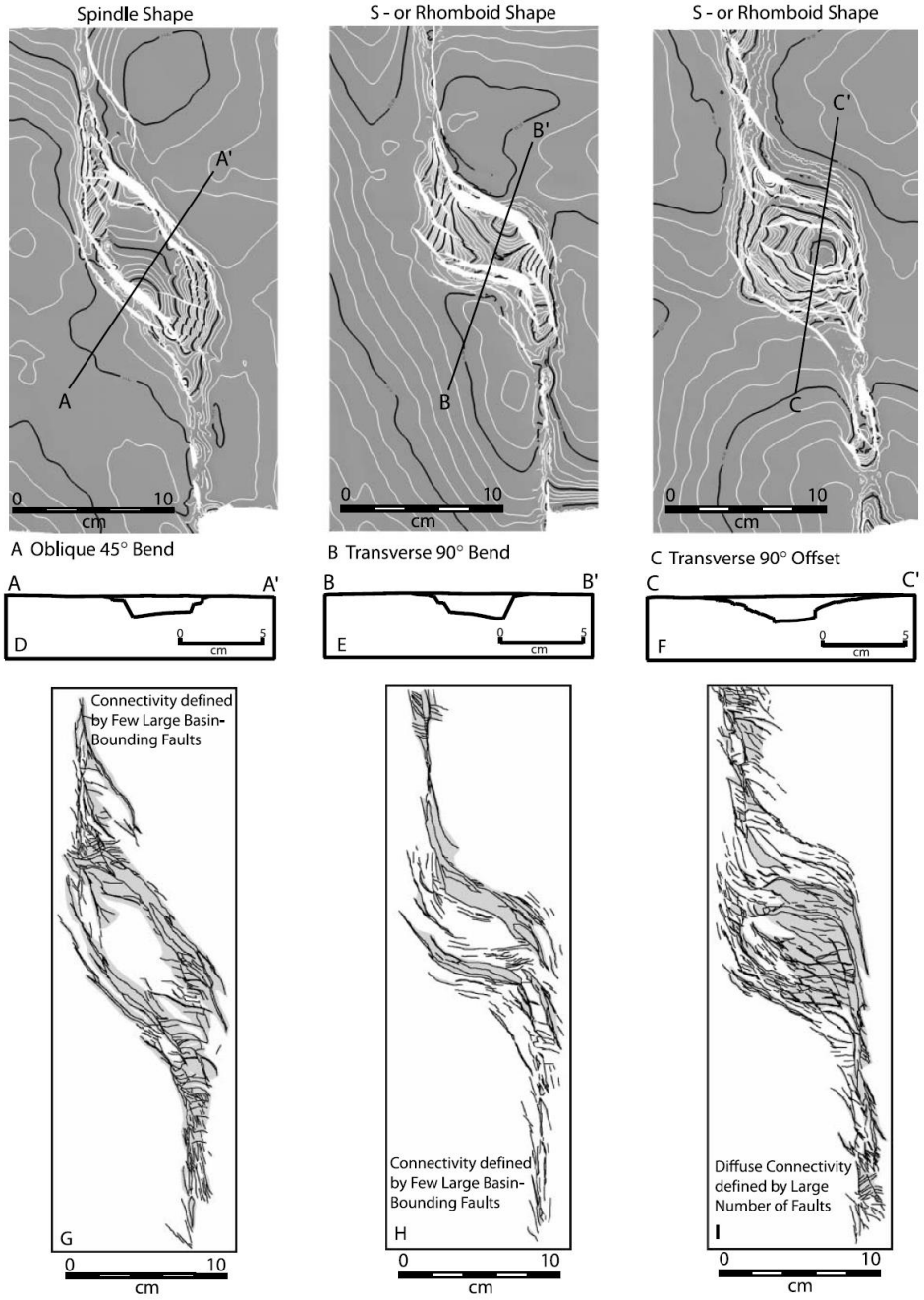
Spindle Shape
S - or Rhomboid Shape
S - or Rhomboid Shape
A'
A
B'
B
C'
C
0
10
cm
A Oblique 45° Bend
B Transverse 90° Bend
C Transverse 90° Offset
A
A'
B
B'
C
C'
D
E
F
0
5
cm
Connectivity defined by Few Large Basin-Bounding Faults
G
Connectivity defined by Few Large Basin-Bounding Faults
H
Diffuse Connectivity defined by Large Number of Faults
I

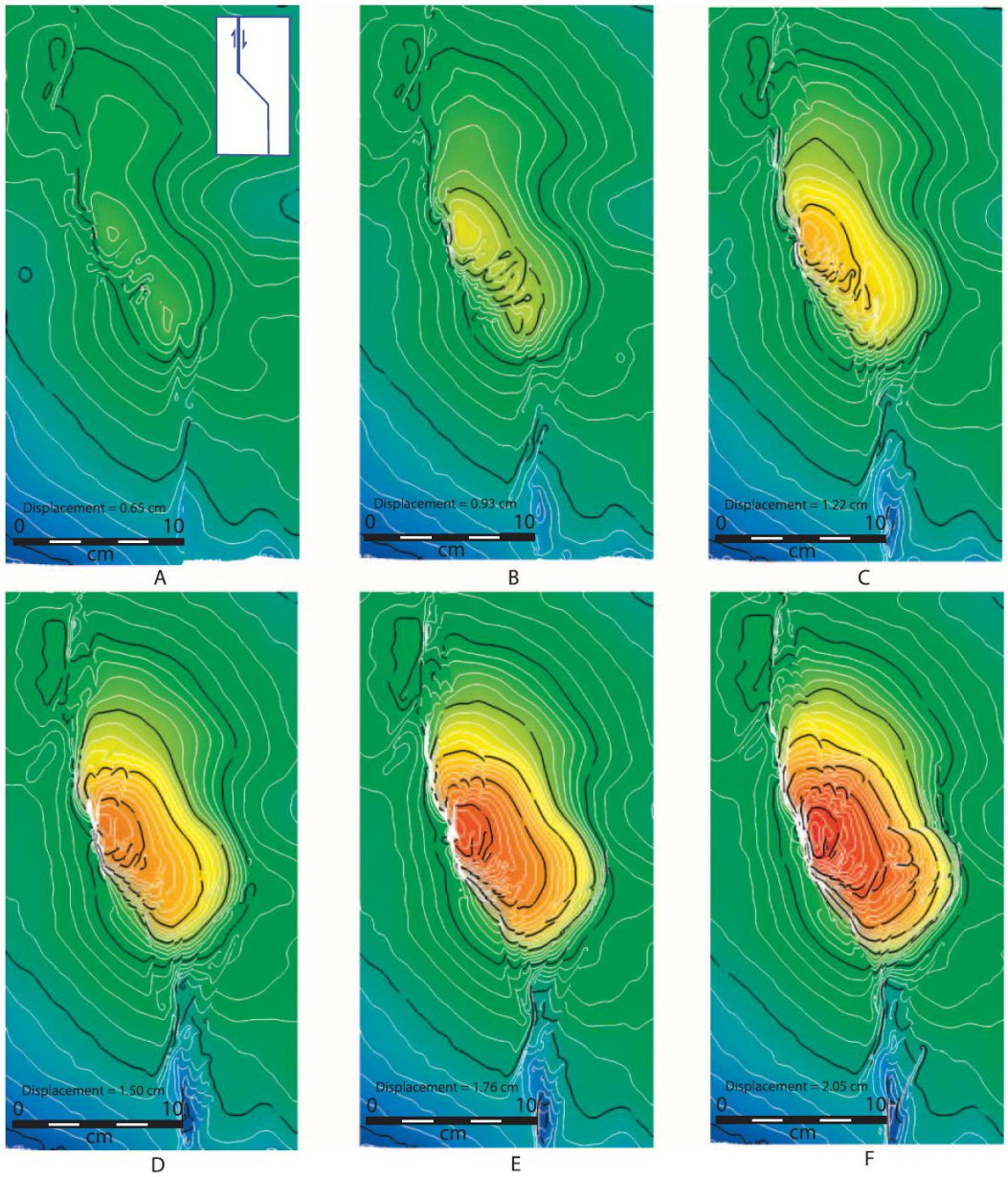

Figure 15. Three-dimensional geometry of the top of the sedimentary cover for a restraining bend with an oblique (45°) bend connecting two strike-slip fault segments in the basement. Panels A–F show the progressive evolution of the structure with increasing strike-slip displacement.

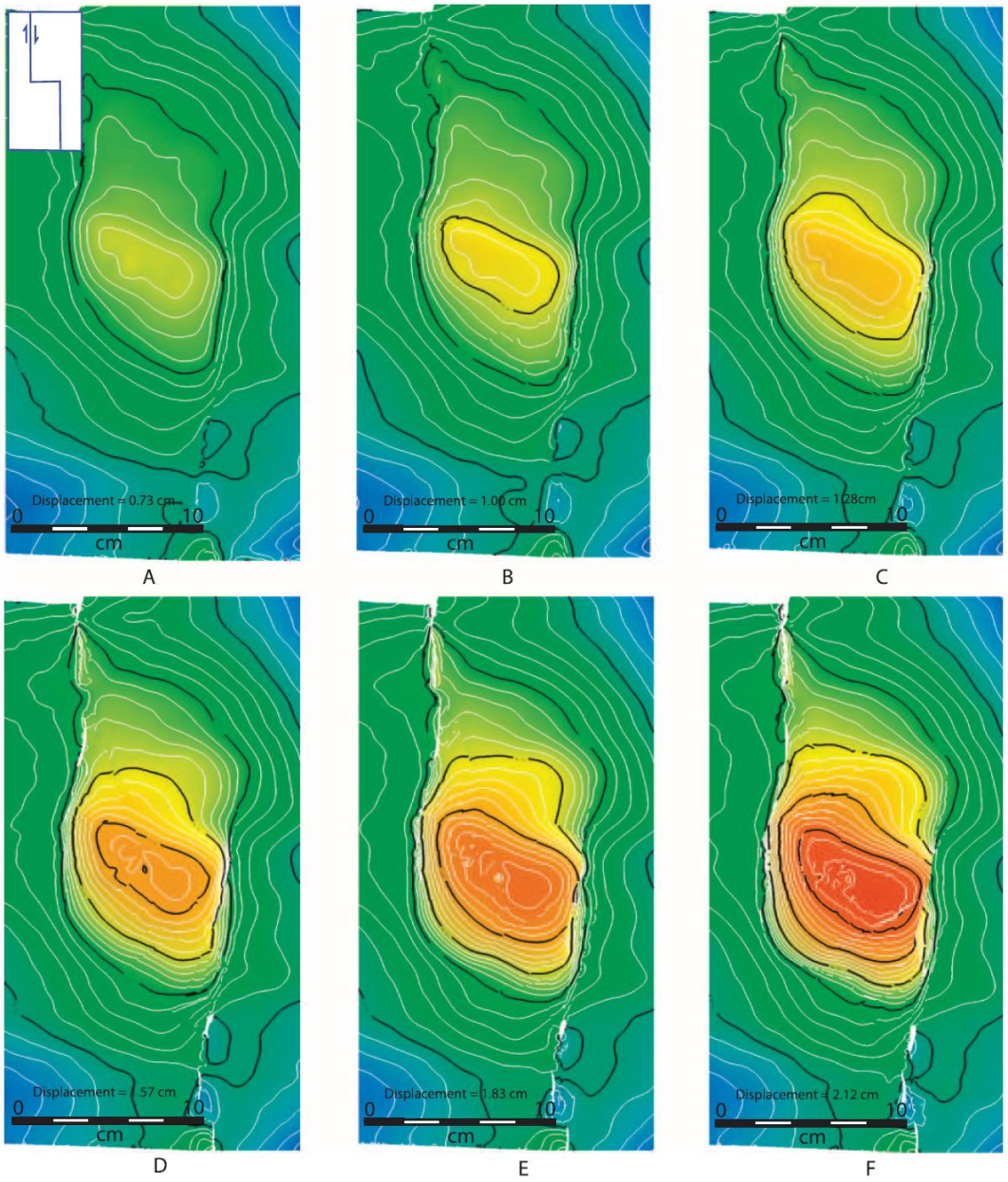

Figure 17. Three-dimensional geometry of the top of the sedimentary cover for a restraining bend with a transverse (90°) bend connecting two strike-slip fault segments in the basement. Panels A–F show the progressive evolution of the structure with increasing strike-slip displacement.

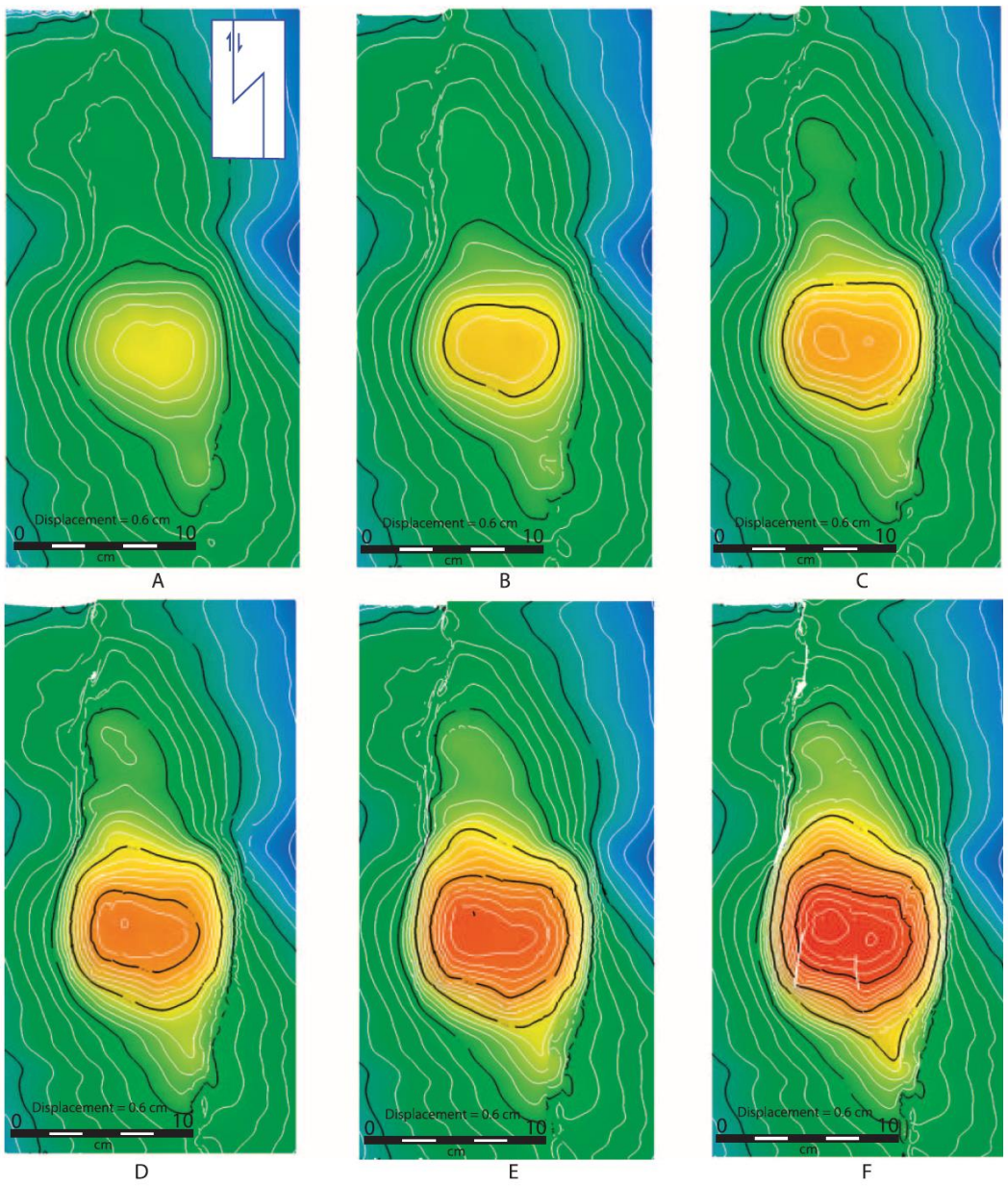

Figure 19. Three-dimensional geometry of the top of the sedimentary cover for a restraining bend with an oblique overlapping (135°) bend connecting two strike-slip fault segments in the basement. Panels A–F show the progressive evolution of the structure with increasing strike-slip displacement.

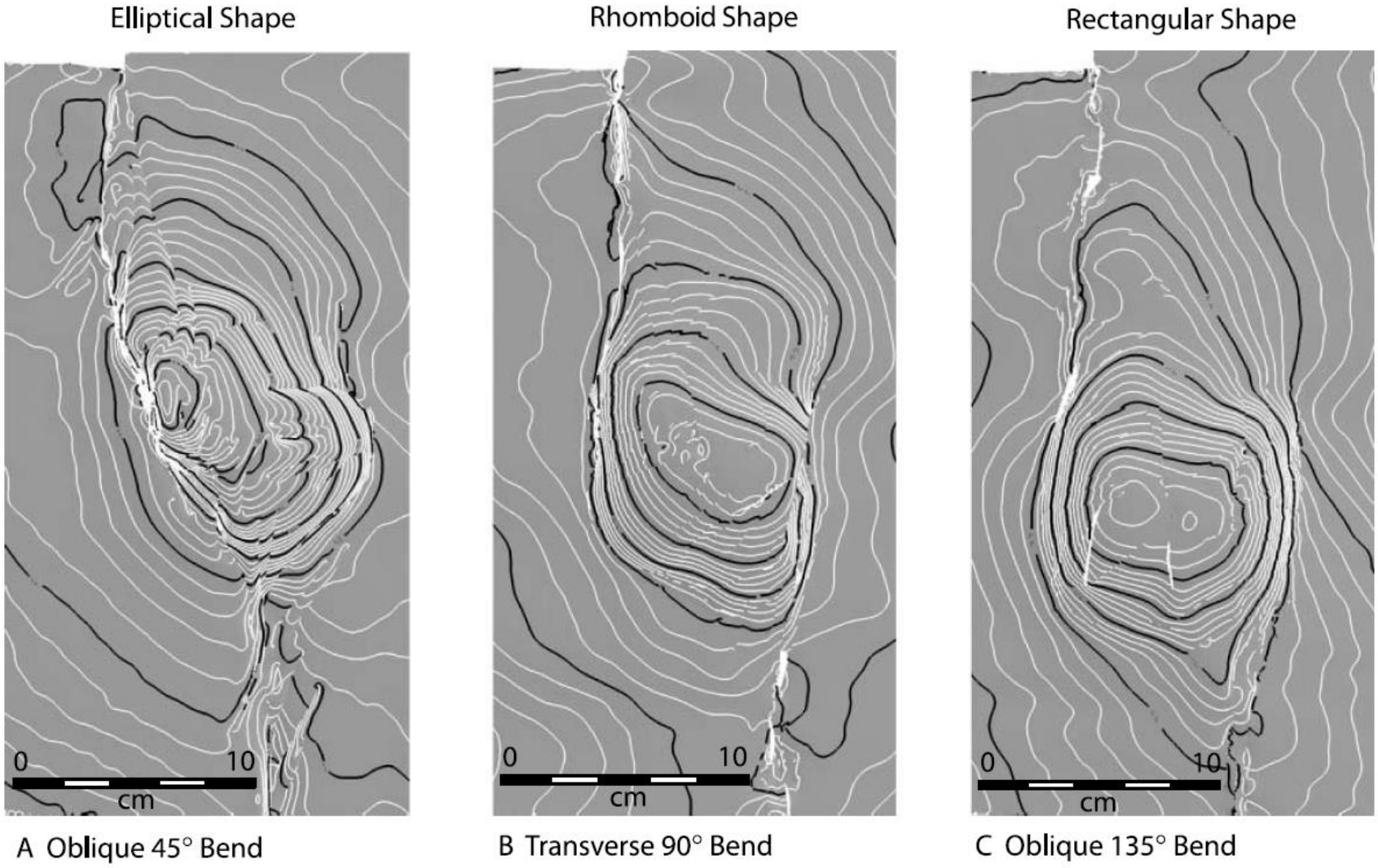

Figure 20. Comparison of final geometries and fault patterns for three restraining bend experiments, with approximately the same amount of strike-slip deformation. (A) Oblique (45°) bend in basement fault. (B) Transverse (90°) bend in basement fault. (C) Overlapping oblique (135°) bend in basement fault. Note the lower angle between axis of the structure and the main strike-slip faults leading to a more elliptical shape in (A) compared with the higher angle leading to a rhomboid shape in (B) and rectangular shape in (C).

Analog models of restraining stepovers in strike-slip fault systems

Ken McClay and Massimo Bonora

AAPG Bulletin, v. 85, no. 2 (February 2001), pp. 233–260

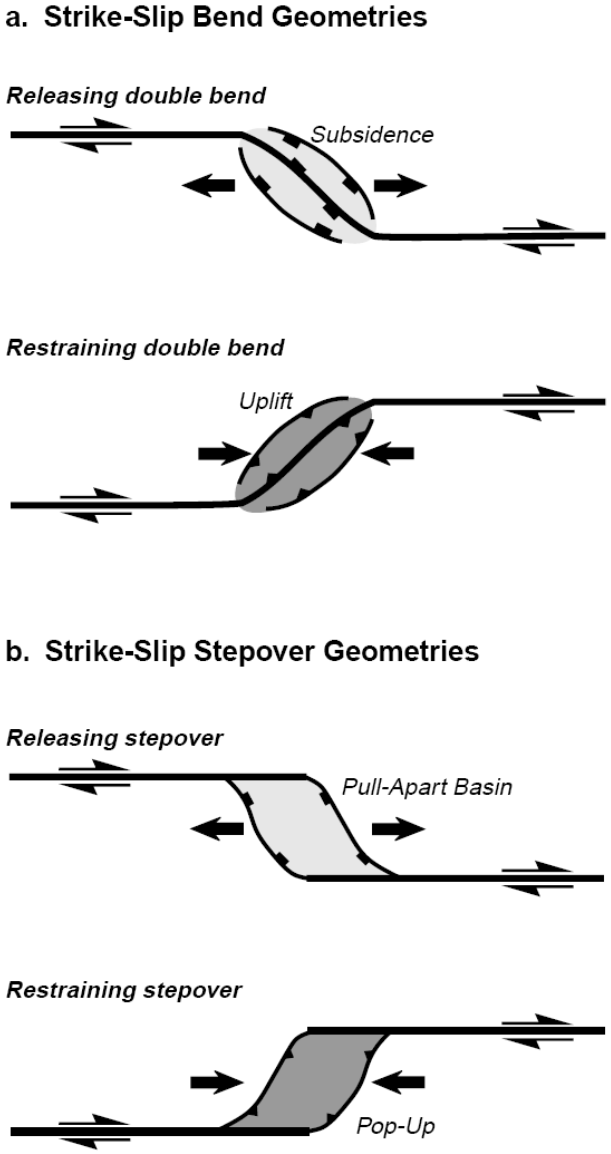

Figure 1. General characteristics of strike-slip fault systems in plan view. (a) Bends in the fault surface produce localized zones of extension and subsidence, whereas restraining bends produce localized zones of contraction and uplift. (b) Stepovers between two offset fault systems produce either pull-apart basins for releasing stepovers or pop-ups and uplifts for restraining stepovers.

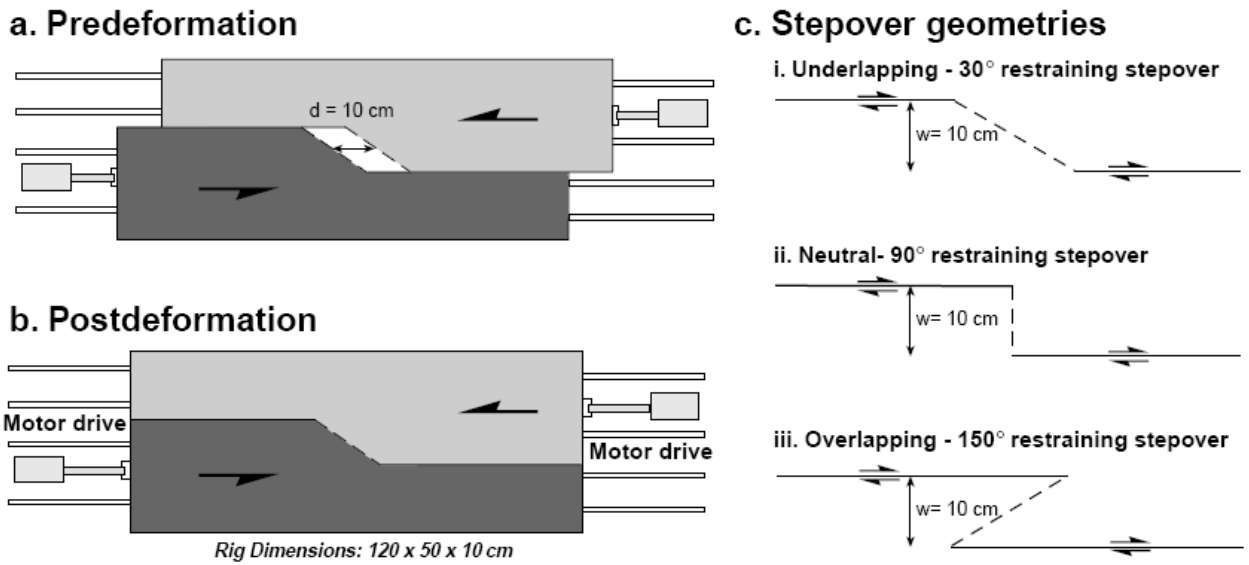

Figure 2. Experimental apparatus. (a) Plan view of experimental apparatus showing the two parts of the deformation table and computer-controlled stepper motors that drive each half. The model is constructed in the central part of the rig, and the sandpack is layered on top of baseplates having predetermined stepover geometries. (b) Stepover geometries analyzed in this article: 30° underlapping, 90° neutral, and 150° overlapping systems.

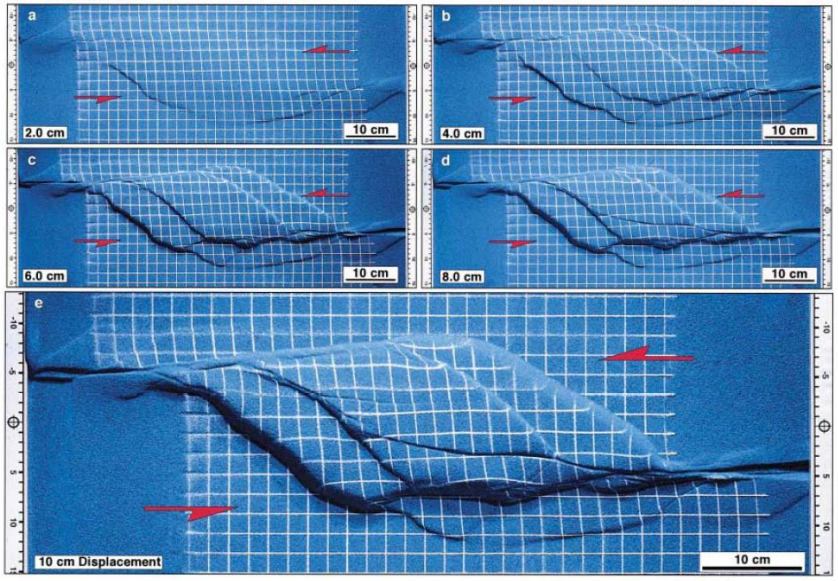

Figure 3. Sequential top-surface photographs showing the progressive evolution of experiment W306, 30° restraining stepover. (a) 2 cm displacement; (b) 4 cm displacement; (c) 6 cm displacement; (d) 8 cm displacement; (e) 10 cm displacement.

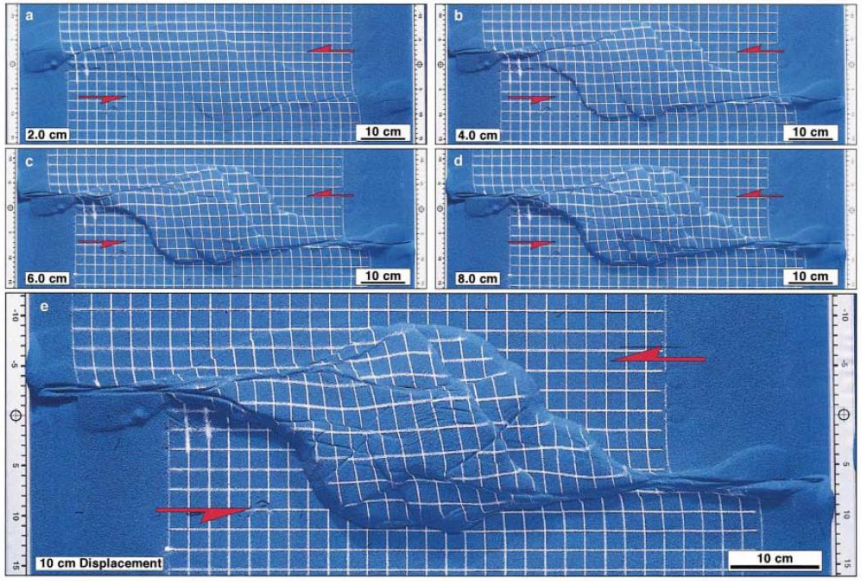

Figure 5. Sequential top surface photographs showing the progressive evolution of experiment W303, 90° restraining stepover. (a) 2 cm displacement; (b) 4 cm displacement; (c) 6 cm displacement; (d) 8 cm displacement; (e) 10 cm displacement.

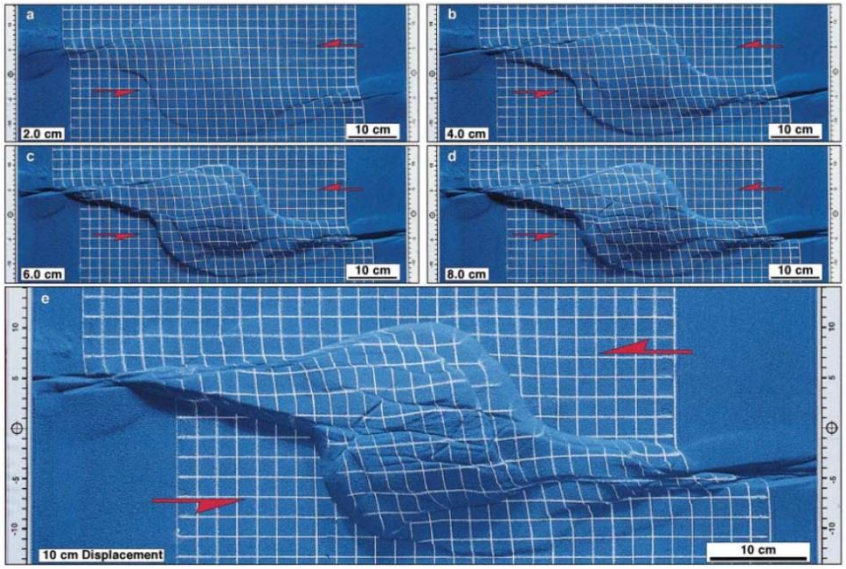

Figure 7. Sequential top-surface photographs showing the progressive evolution of experiment W309, 150° restraining stepover. (a) 2 cm displacement; (b) 4 cm displacement; (c) 6 cm displacement; (d) 8 cm displacement; (e) 10 cm displacement.

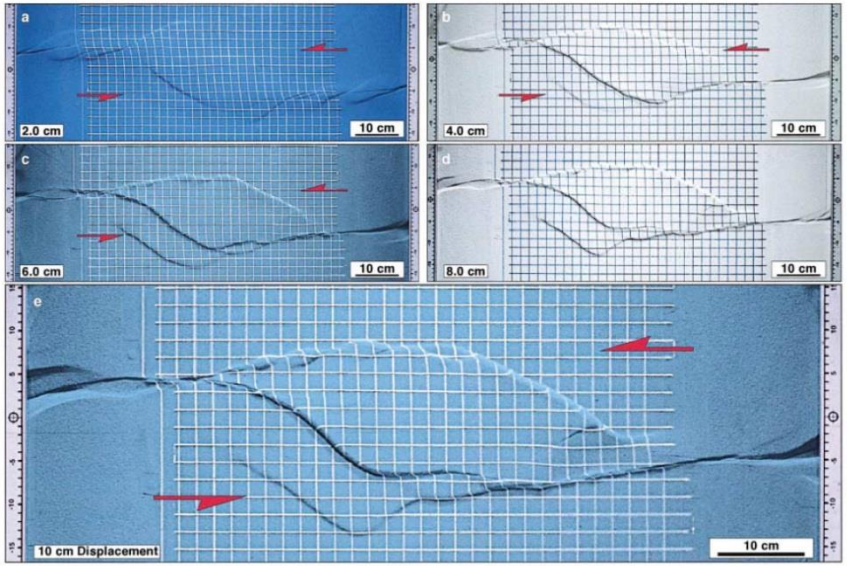

Figure 10. Sequential top-surface photographs showing the progressive evolution of experiment W324, 30° restraining stepover. Synkinematic sedimentation was added incrementally after each 2 cm of displacement. (a) 2 cm displacement; (b) 4 cm displacement; (c) 6 cm displacement; (d) 8 cm displacement; (e) 10 cm displacement.

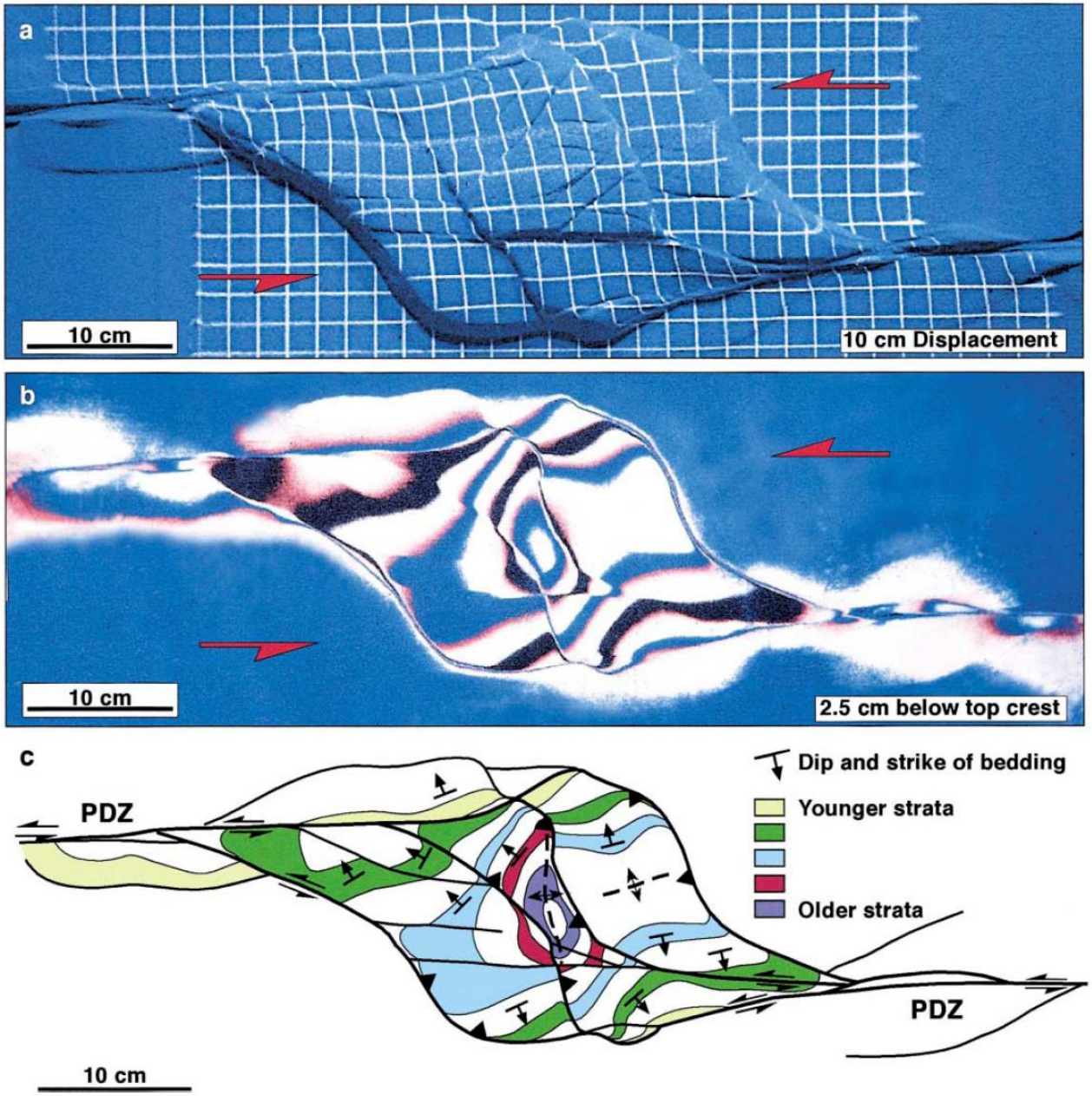

Figure 9. Experiment W305 after 10 cm sinistral displacement. (a) Top surface of model showing pop-up faults. (b) Horizontal section taken 1 cm below top surface. (c) Interpretation of **b**, showing the folds, faults, and bed-dip directions.

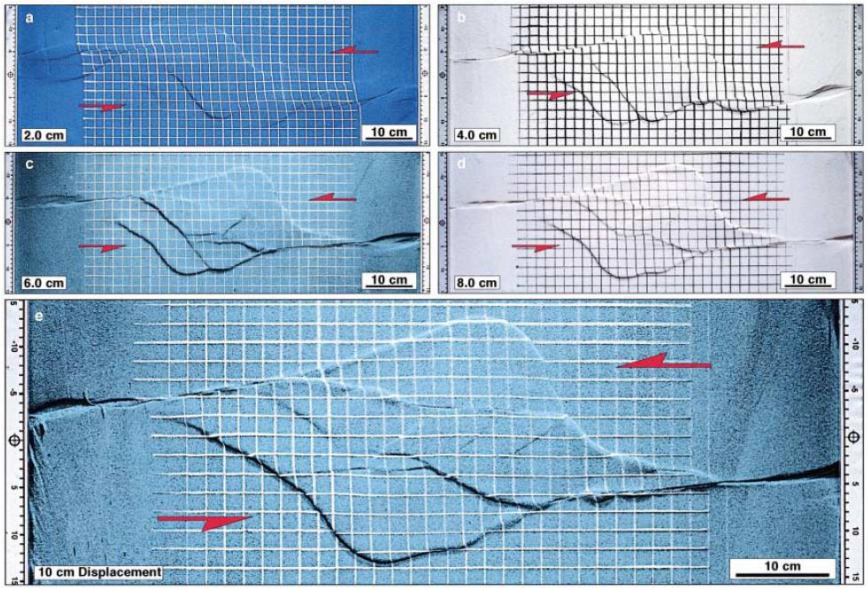

Figure 12. Sequential top-surface photographs showing the progressive evolution of experiment W314, 90° restraining stepover. Synkinematic sedimentation was added incrementally after each 2 cm of displacement. (a) 2 cm displacement; (b) 4 cm displacement; (c) 6 cm displacement; (d) 8 cm displacement; (e) 10 cm displacement.

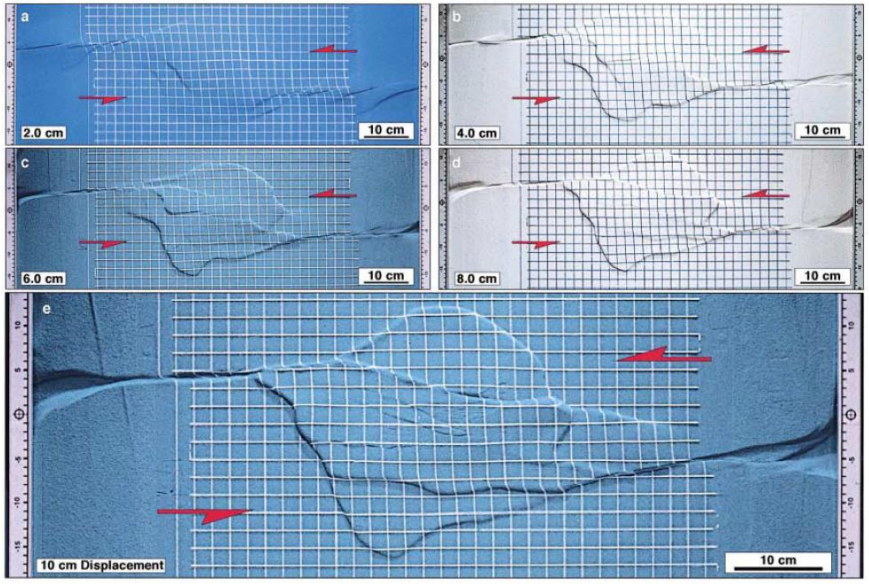

Figure 14. Sequential top-surface photographs showing the progressive evolution of experiment W325, 150° restraining stepover. Synkinematic sedimentation was added incrementally after each 2 cm of displacement. (a) 2 cm displacement; (b) 4 cm displacement; (c) 6 cm displacement; (d) 8 cm displacement; (e) 10 cm displacement.

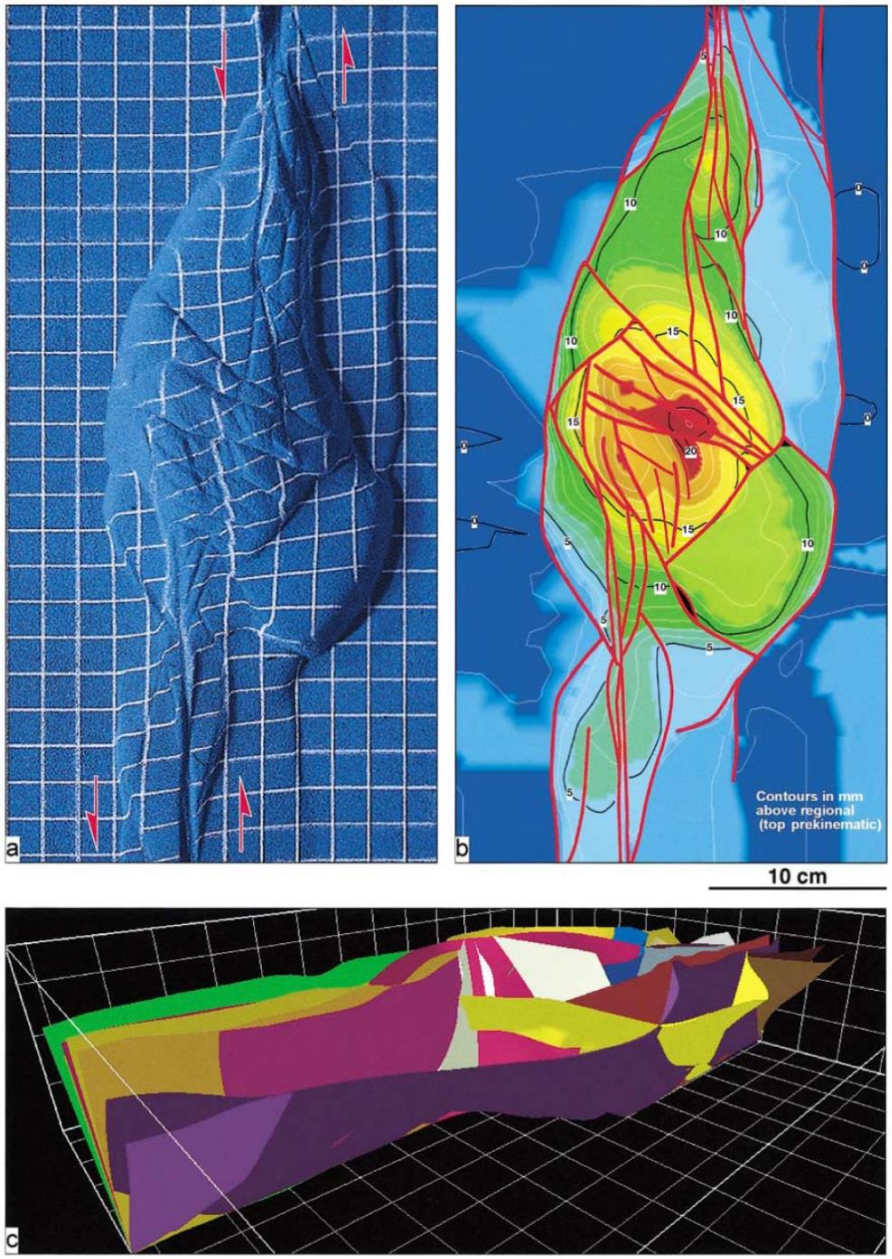

Figure 16. Experiment E307: 90° neutral stepover and 5 cm stepover width. (a) Photograph of the upper surface of the model after 10 cm displacement on the basement faults. (b) Structure contours of the upper surface of the model as interpolated from fifty serial sections across the completed model. (c) Longitudinal sections across model W307. (d) Perspective view of a 3-D visualization of the faults in model W307.

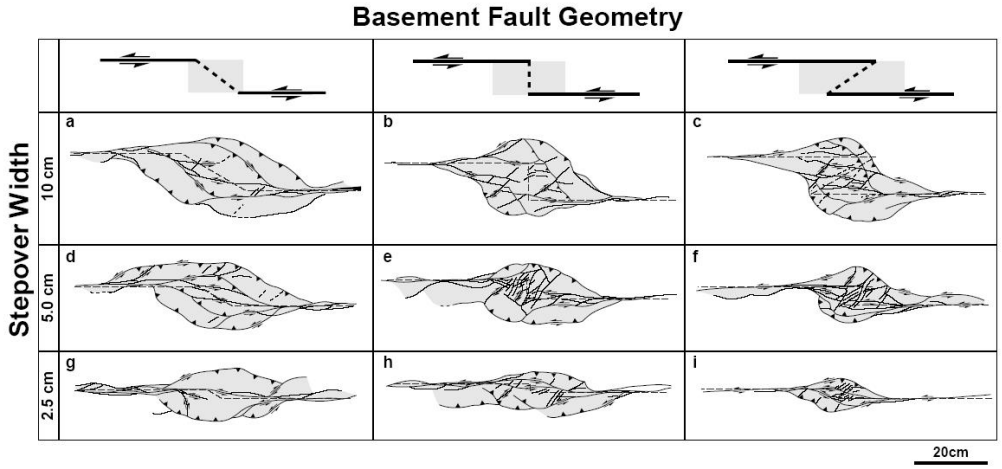

Figure 17. Summary of pop-up structures for restraining stepover spacing from 10 to 2.5 cm. In all experiments displacement on the basement master faults was 10 cm. Sandpack thickness 5 cm.

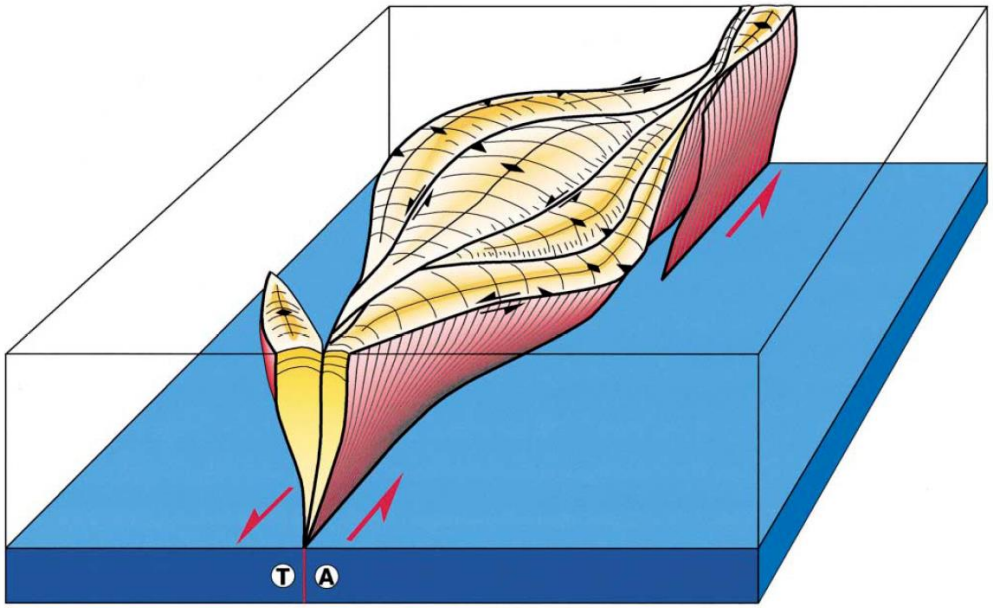

Figure 18. Synoptic diagram illustrating the 3-D geometry of an idealized pop-up structure based on the results of the analog modeling program. T = baseplate movement toward viewer; A = baseplate movement away from viewer.

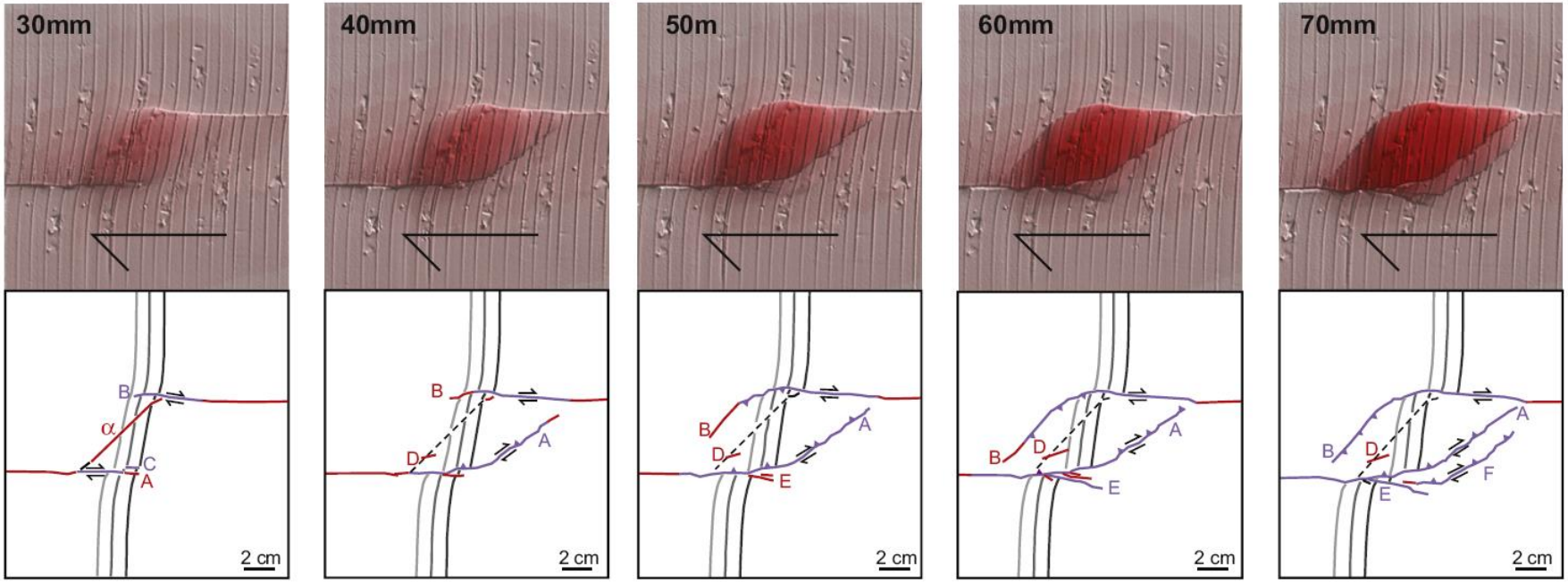

Fig. 5. Uplift pattern and fault map for the 45° 5 cm stepover restraining bend. The color of the fault trace indicates if its motion is primarily strike-slip (red) or oblique-slip (purple). The color scale for uplift is the same as Fig. 4. The restraining segments show some slip at early stages of the experiment but does not accumulate additional slip past 40 mm of plate displacement. Faults A and B start propagating by 20 mm of displacement. The strike of these segments parallels the plate velocity until 40 mm when both faults curve to parallel the restraining segment. By 40 mm of plate displacement, fault A has linked with a small fault (fault C) and has propagated nearly to link with fault B on the far side of the restraining bend. At 50 and 60 mm plate displacement, small faults grow where fault A changes strike. The segments of faults A and B that parallel the restraining segment have oblique-slip motion. From 60 to 70 mm of plate displacement we see fault activity shift from fault A to a new fault F outboard of fault A. The uplift pattern shows that by 70 mm of displacement the new fault F acts as the range-bounding fault. (For interpretation of the references to color in this figure legend, the reader is referred to the web version of this article.)

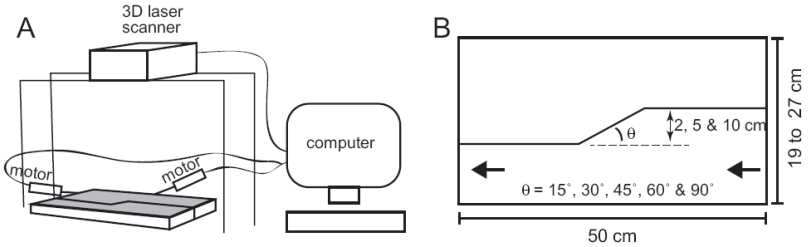

Fig. 2. A) Two computer-controlled stepper motors displace one side of the deformational claybox. In this experiment, one motor is used to apply right lateral slip to the restraining bend. The 3D laser scanner directly records vertical surface deformation and documents shear of initial lines that become warped and offset during the experiment. B) Configuration of the basal plates is varied to explore different restraining bend geometries. The width of the experiment varies from 19 to 27 cm as different experiments have different stepover distance.

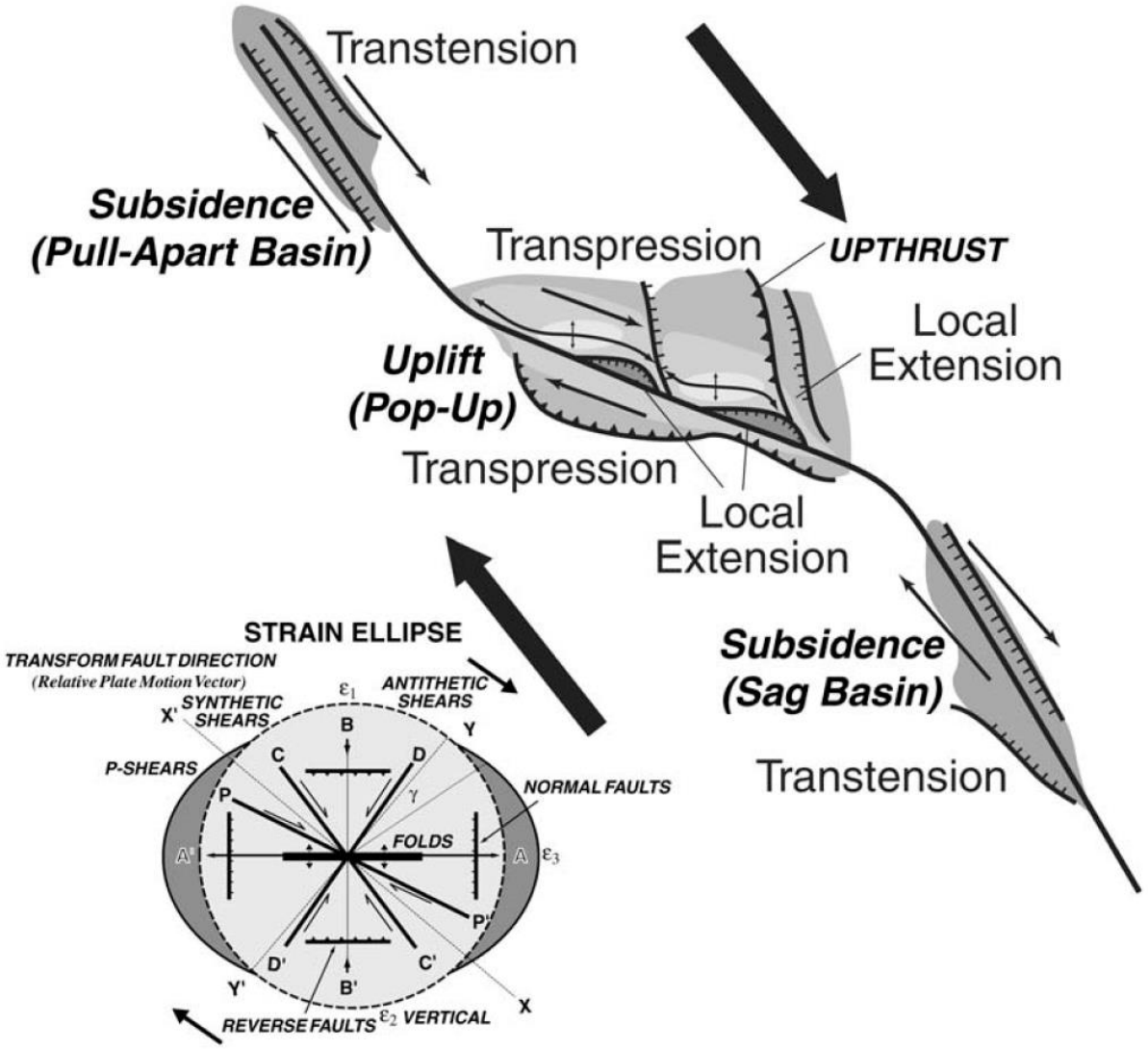

Fig. 9. Typical morphology and structure of restraining double bends in southern California, based on the San Clemente Fault bend region. Some features may be missing on other restraining bends, but some features may be more pronounced than in the San Clemente Fault example. Most Borderland restraining double bends have transtensional zones at the ends. A strain ellipse is shown to highlight the expected structural character for different trends in a zone of NW-directed dextral shear (after Wilcox *et al.* 1973). Contrary to the expected strain patterns, the north-trending faults in the San Clemente Fault bend region are steeply dipping upthrusts, not normal faults.

Lithospheric-scale centrifuge models of pull-apart basins

Giacomo Corti [a,*], Tim P. Dooley [b]

[a] CNR, Consiglio Nazionale delle Ricerche, Istituto di Geoscienze e Georisorse, U.O. Firenze, Via G. La Pira, 4, 50121 Florence, Italy
[b] Bureau of Economic Geology, The University of Texas at Austin, University Station, Box X, Austin, TX 78713, USA

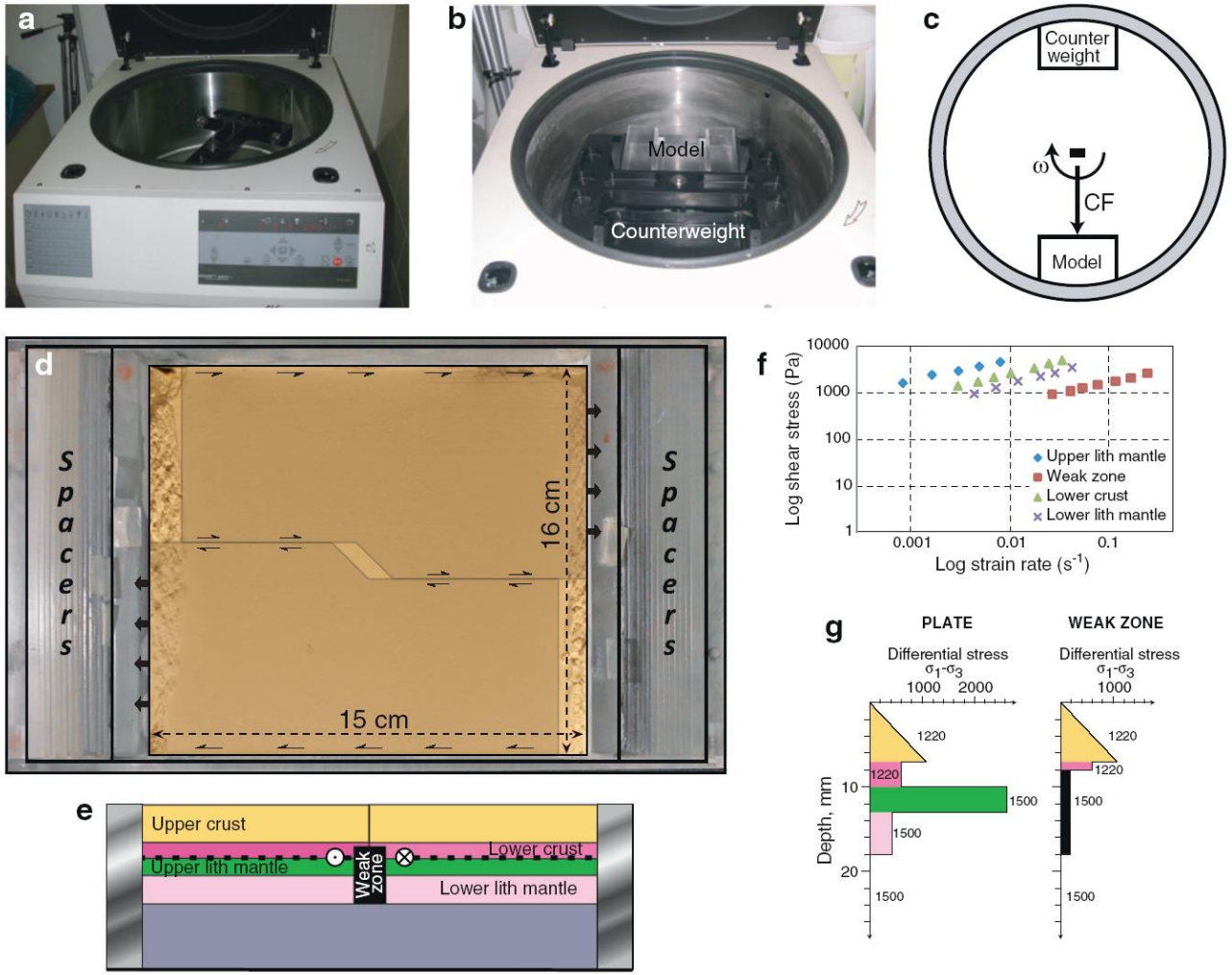

Fig. 1. Experimental setup. (a) Frontal view of the large-capacity centrifuge at the Tectonic Modelling Laboratory of the Institute of Geosciences and Earth Resources (National Research Council of Italy). (b) Close-up of the internal rotor. (c) Loading conditions in the centrifuge (CFF, centrifuge force field). (d) Top-view photo of a model, illustrating the geometry of deformation. (e) Model cross section illustrating the vertical rheological layering. (f) Stress–strain-rate relationships for the different viscous materials used to simulate the continental lithosphere (lith) plotted in a log–log graph. (g) Strength profiles of the model lithosphere in the different domains; numbers indicate the density of the different materials (in kg m^{-3}).

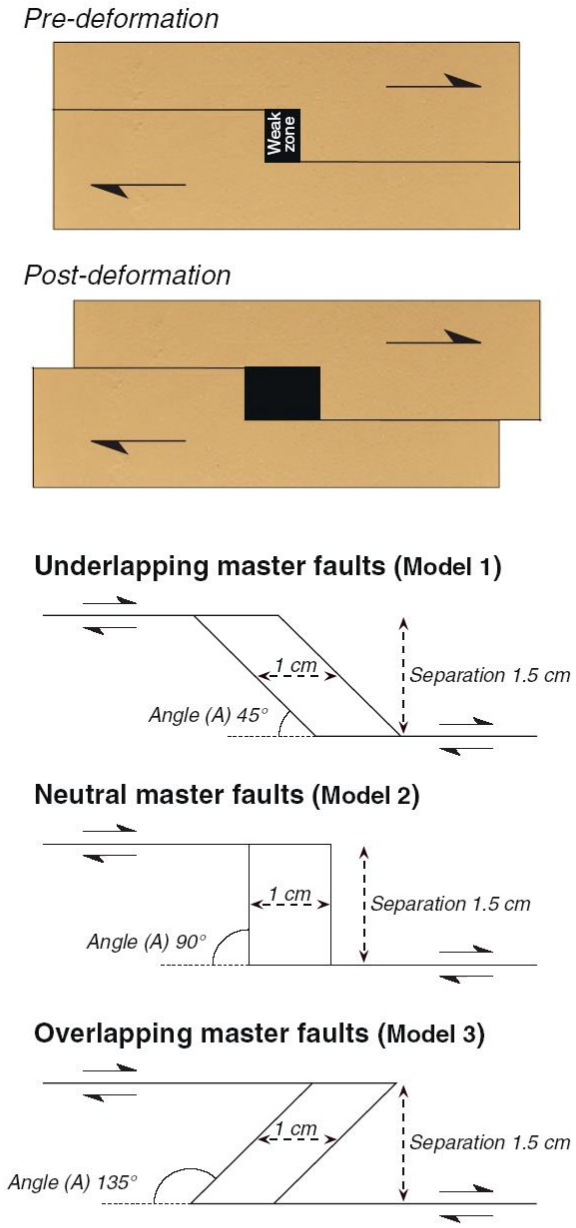

Fig. 2. Geometrical characteristics of the model setups. (a) Overhead view illustrating pre- and post-deformation of the master faults and offset zone. (b) Separation and angular relationships of the stepovers for the three models presented in this paper. The angles of the stepovers are identical in geometry to those presented in Dooley and McClay (1997) and Dooley and Schreurs (2012).

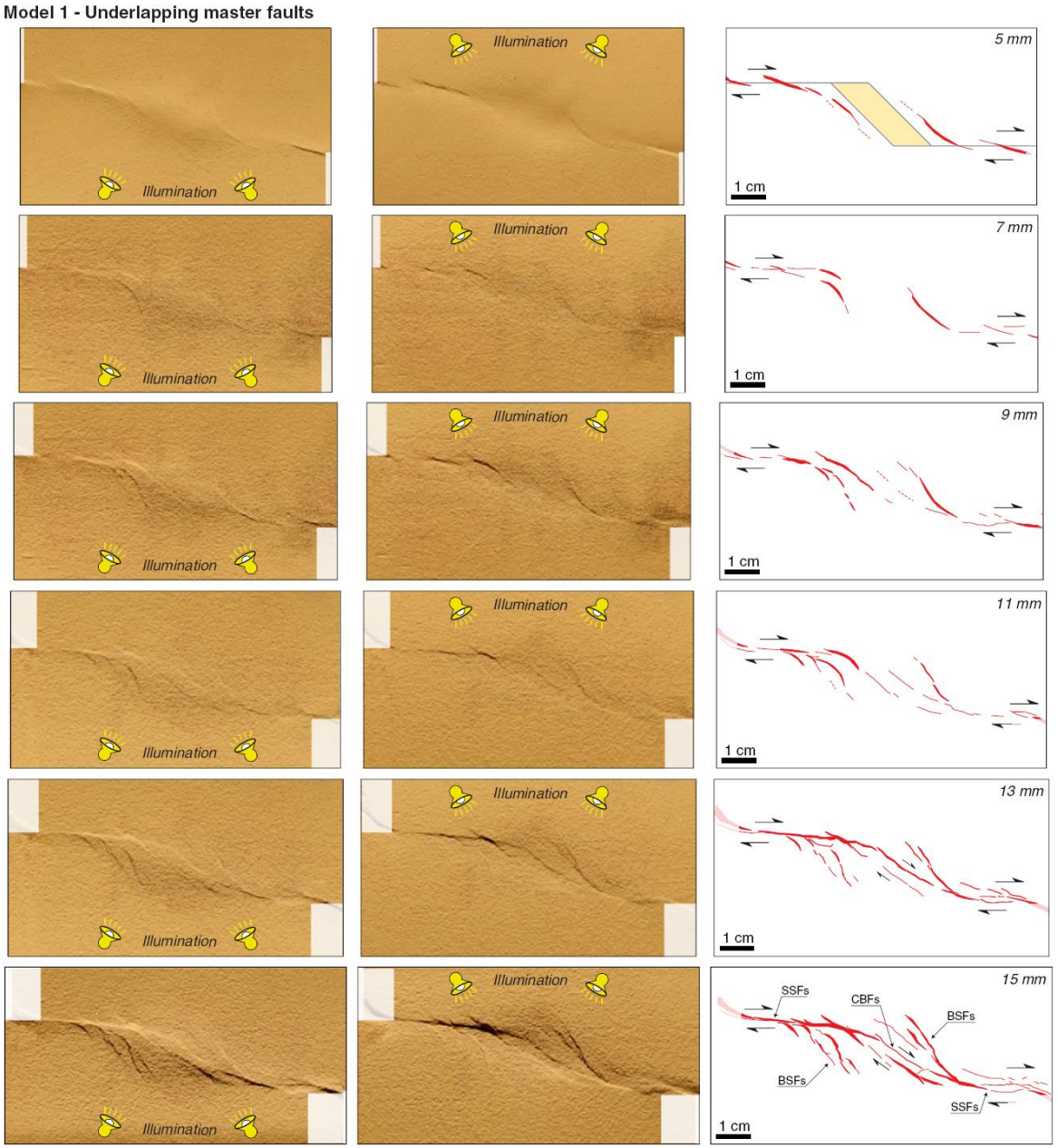

Fig. 3. Evolution of model with underlapping master fault (Model 1), shown as sequential top-view photos with differing illumination angles (left and central panels) and line drawings of structures (right panels). BSFs: basin sidewall faults; CBFs: cross-basin faults; SSFs: strike–slip faults.

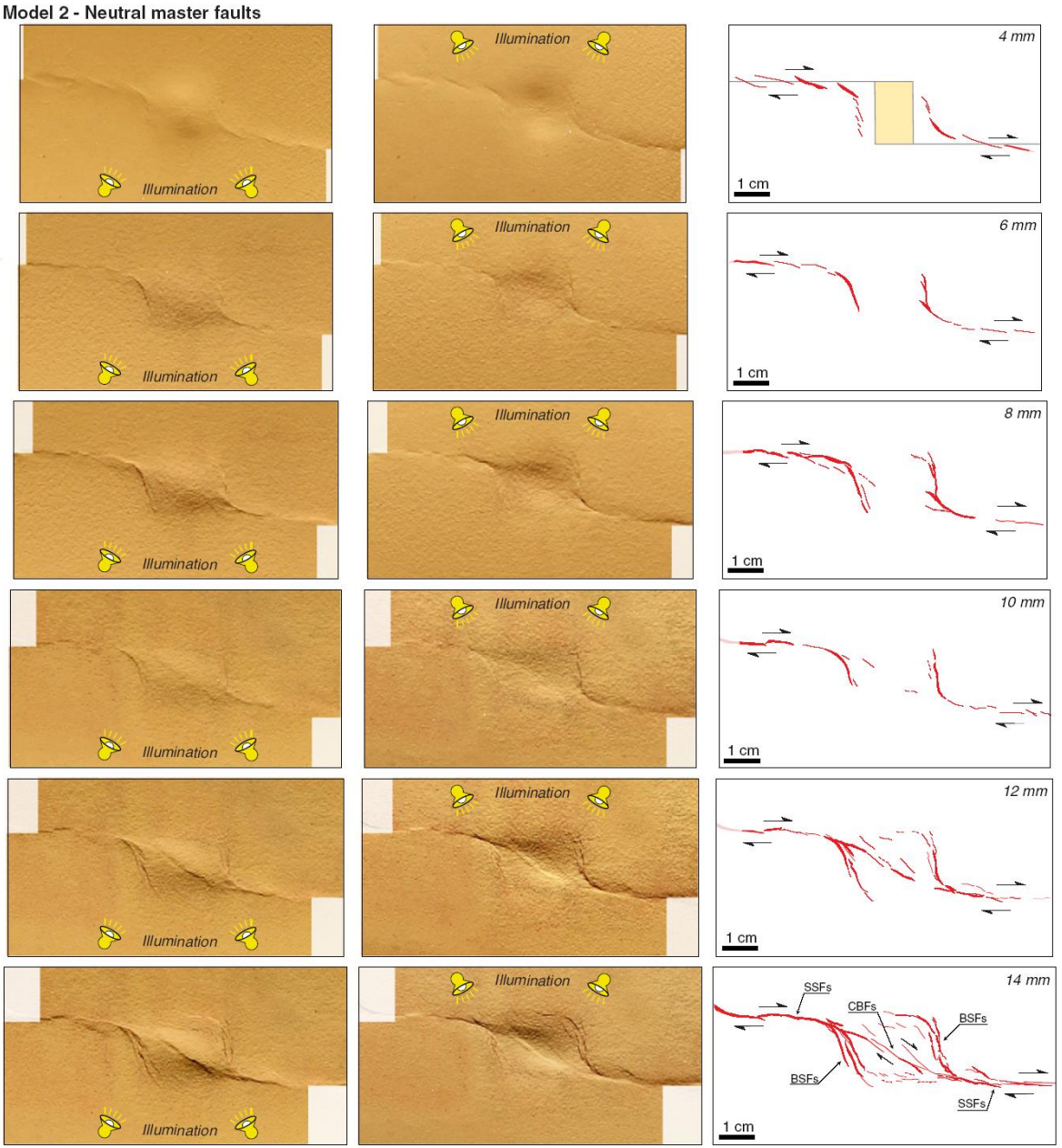

Fig. 4. Evolution of model with neutral master fault (Model 2), shown as sequential top-view photos with differing illumination angles (left and central panels) and line drawings of structures (right panels). BSFs: basin sidewall faults; CBFs: cross-basin faults; SSFs: strike–slip faults.

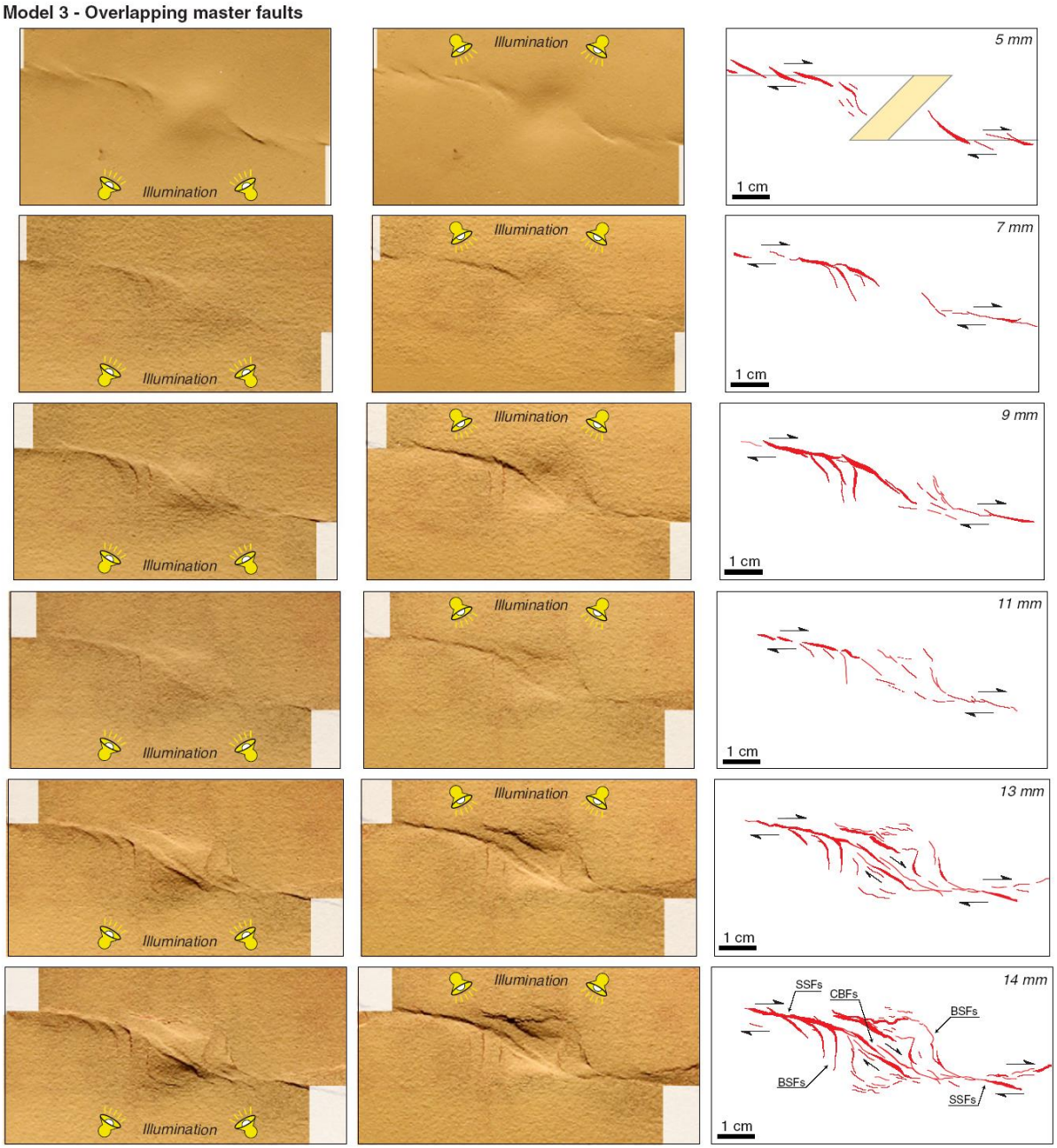

Fig. 5. Evolution of model with overlapping master fault (Model 3), shown as sequential top-view photos with differing illumination angles (left and central panels) and line drawings of structures (right panels). BSFs: basin sidewall faults; CBFs: cross-basin faults; SSFs: strike–slip faults.

Fig. 6. Cross sections from the underlapping (left), neutral (centre) and overlapping (right) master-fault models. Of note is the along-strike variation in basin morphology and the dip-polarity change from one end of the basin to the other. For example, in case of underlapping master faults, the upper crust dips mainly to the right in Section C–C′ then flips to dominantly left dipping in Section E–E′. The same occurs in the other models. Note in sections B-B′ and D-D′ of Model 2 that the thin layer of lower crust above the black weak material composing the weakness zone has been in places completely removed by ductile thinning.

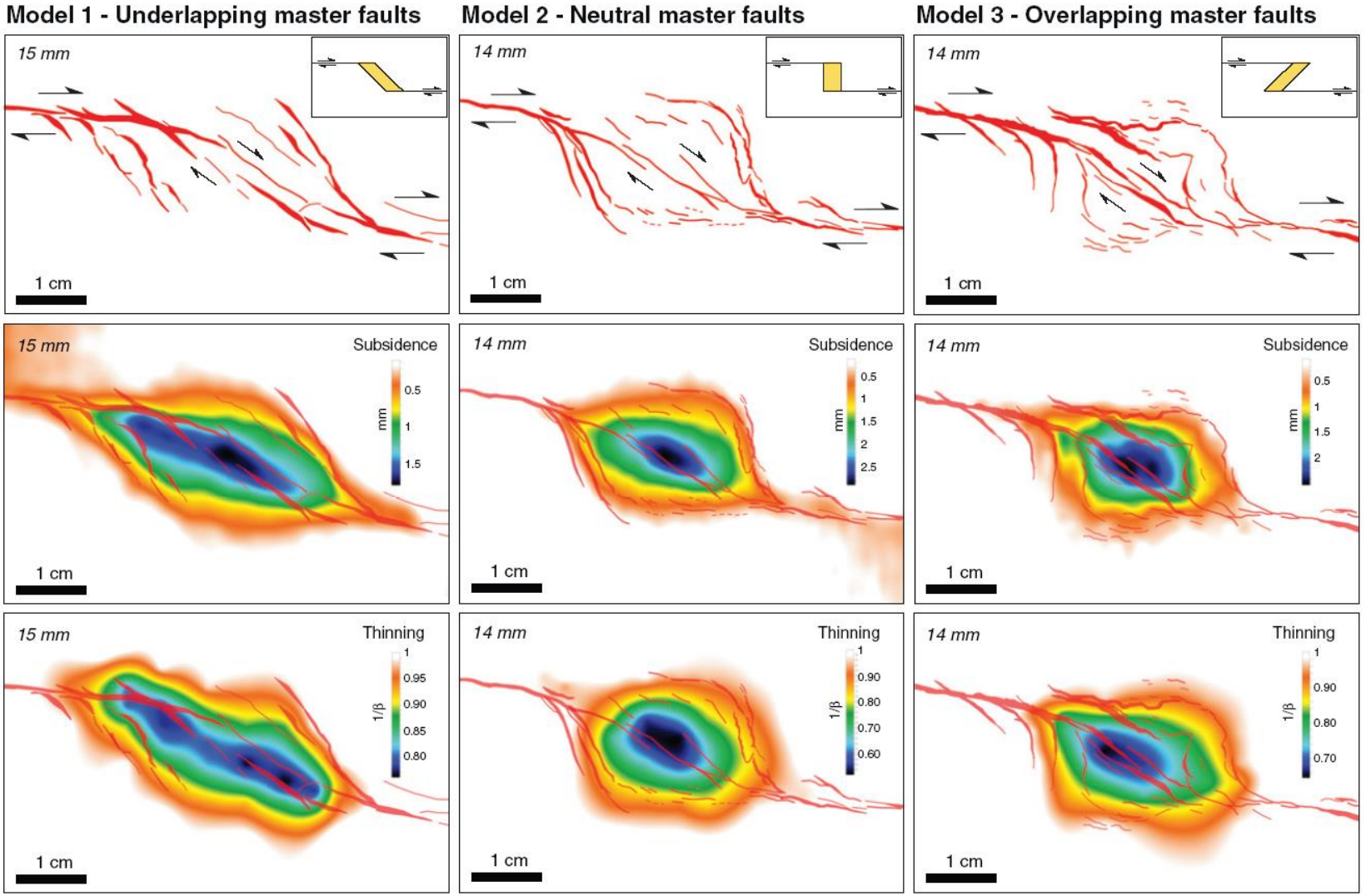

Fig. 7. Surface deformation and lithospheric thinning in the three models, illustrated as fault pattern (top panels), amount of subsidence (central panels) and patterns of lithospheric thinning (bottom panels), indicated with the 1/β factor (where 1/β is the ratio between the final and the initial thickness of the model crust).

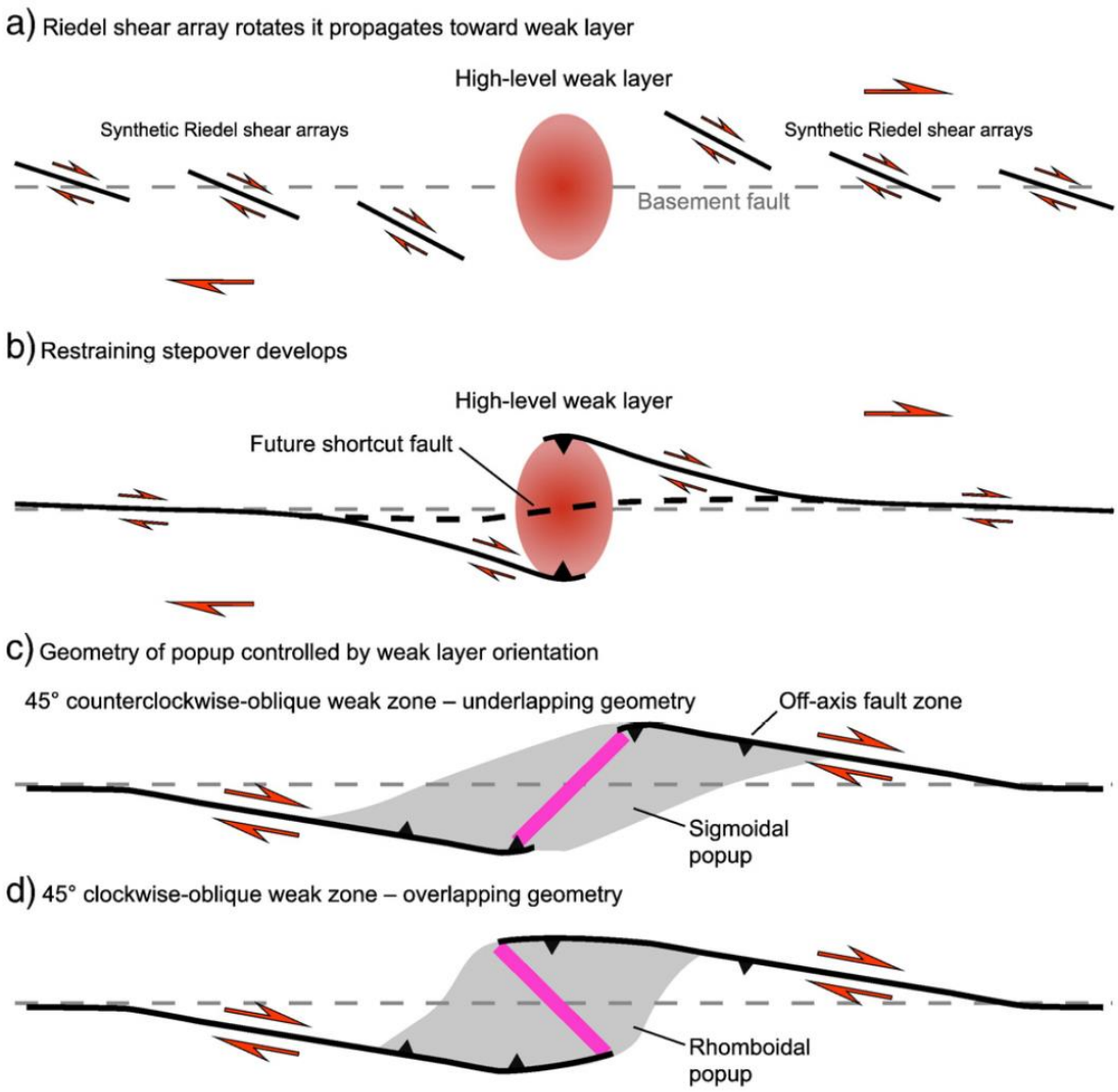

Fig. 72. Summary diagram illustrating typical restraining stepover geometry formed across weak bodies. (a) Riedel shears propagate toward the weak body and gradually diverge from the trace of the basement fault. (b) Linked faults form restraining stepover centred on the weak body. (c) Weak bodies oriented 45° counterclockwise-oblique to the basement fault approximate popups formed above underlapping master-fault geometries. (d) Weak bodies oriented 45° clockwise-oblique to the basement fault approximate popups formed above overlapping master-fault geometries.